POLITECNICO DI TORINO

Master's Degree in Aerospace Engineering





Master's Degree Thesis

Modeling and Analysis of The Deployment of a Tethered Satellite System

Supervisors

Candidate

Prof. Eleonora BOTTA

Abdossalam NAAMAD

Prof. Marcello ROMANO

Eng. Stefano ALIBERTI

October 2025

Summary

The use of Tethered Satellite Systems (TSS) has emerged as an attractive alternative for space-based radar sounding missions. Recent studies have demonstrated that a TSS enables the realization of large antenna apertures while reducing the propulsion requirements typically associated with traditional Formation Flying. Although this solution can significantly enhance sensing performance, it is inherently affected by dynamical instability, which makes the analysis of its dynamics and deployment phase an interesting aspect for system design.

To this end, the research begins with the formulation of a comprehensive mathematical model relying on two of the main modeling methods for Tethered Satellite Systems: the rod model and the discrete model. Subsequently, the numerical simulation framework is introduced and studied to enable systematic simulation of the system's dynamics across different configurations and operational environments. After an initial analysis of the dynamics of the TSS at a constant tether length, attention is shifted to the deployment process, highlighting the difficulties associated with this phase. In particular, the free system's deployment along the radial, along-track, and cross-track directions is investigated.

Subsequently, for each of these strategies, a preliminary control analysis is performed on the rod model, and relative control accelerations are derived and subsequently applied to the higher-fidelity system representation using the discrete model. This approach provides a comparison of each deployment strategy, highlighting both the stability challenges and the control resources associated with each option. Beyond providing practical guidelines for TSS mission design, the results establish a preliminary foundation for deeper study on control strategies for the deployment phase.

Acknowledgements

This hundred-page work marks the end of my Master's degree journey, which has been rich in wonderful people and in both profound and joyful moments. Therefore, I would like to take a moment to express my gratitude to all those who have been part of this chapter of my life. First and foremost, I express my deepest gratitude to my family, beginning with my parents, hoping that this achievement can repay in part their sacrifices, as well as my siblings and all the other family members, from the youngest to the oldest. I am also profoundly grateful to each one of my friends who has carved out a space in my life over these years, scattered across three continents and four countries.

I would like to express my sincere gratitude to Stefano Aliberti, the PhD candidate who carefully guided me through the various stages of this research. I am also deeply grateful to Dr. Eleonora Botta for her support throughout the development of the code, the simulations, and the writing of this thesis. Beyond her technical guidance, I am profoundly grateful for the extraordinary opportunity for personal and professional growth I experienced at the University at Buffalo, through my involvement in the student community and the activities of the Space Systems Dynamics and Control Laboratory. This opportunity - after God's will - would not have been possible without her trust and support. Finally, I would like to thank Dr. Marcello Romano for welcoming me into his research group as a thesis student.

عبد السلام نعماد "Abdossalam Naamad"

Table of Contents

Li	st of	Tables	viii
Li	st of	Figures	ix
1	Intr	roduction to space tethers	1
	1.1	Introduction	1
	1.2	Electrodynamic Tethers	2
		1.2.1 Space debris digression	3
	1.3	Momentum exchange tethers	5
	1.4	Distributed Space Systems	7
		1.4.1 Tethered Satellite Systems	10
	1.5	Further suggested applications of tethers	13
	1.6	Space based radar sounding	14
	1.7	Tethered Satellite Systems Deployment	16
		1.7.1 Notable Cases of Deployment Failure in TSS Missions	17
		1.7.2 State of the Art in Tether Deployment and Stabilization	19
	1.8	Work Subdivision	20
2	Not	cation and Mathematical Tools	22
	2.1	Vectors and Unit Vectors	22
	2.2	Reference Frames	23
		2.2.1 Earth Centered Inertial (ECI)	23
		2.2.2 Perifocal	24
		2.2.3 Local Vertical - Local Horizontal (L)	25
	2.3	Rotation Matrices	27
3	Ma	thematical Model	29
	3.1	Rotating Reference Frame	29
	3.2	Modeling of the external forces	
		3.2.1 Earth's Gravitational Potential Perturbation	32
		3.2.2 Aerodynamic drag	34

	3.3	Modeling of the internal forces	35
		3.3.1 Tether discrete model	36
		3.3.2 Tether dumbbell model	41
		3.3.3 Control forces	42
	3.4	Equations of motion for the discrete model	12
		3.4.1 Deployment's effect on the equations of motion	45
	3.5	Equations of motion for the dumbbell model	49
4	Nui	merical Simulation	53
	4.1	Code Structure	54
		4.1.1 Initialization	54
		4.1.2 Integration	56
		4.1.3 Post-processing	56
5	Nui	merical Results	58
	5.1	Simulation set-up	58
	5.2	TSS free dynamics propagation	30
			31
			35
			38
	5.3		73
			75
			77
			7 9
6	Dep	ployment Strategies 8	32
	6.1		33
	6.2	Proportional-Integral-Derivative Control	33
		6.2.1 Implementation within the reference model 8	34
	6.3	Radial PID controlled deployment	36
		6.3.1 Validation on the discrete model: Radial Configuration case	90
	6.4	Along-track PID controlled deployment	92
		6.4.1 Validation on the discrete model: Along-track Configuration	
	c r		95
	6.5		97
		6.5.1 Validation on the discrete model: Cross-track Configuration	<u>ر</u>
		case	JU
7		nclusions and future work 10	
	7.1	Conclusion	
	7.2	Possible extension and future research)4

Bibliography 107

List of Tables

5.1	Orbital Parameters
5.2	Satellites Parameters
5.3	Tether Parameters
5.4	Lumped masses Parameters
5.5	Reference coordinates for the radial configuration 6
5.6	Reference coordinates for the along-track configuration 65
5.7	Reference coordinates for the cross-track configuration 68
5.8	Deployment's initial and target conditions

List of Figures

1.1	Spinning based Momentum Exchange Tether System	5
1.2	Orbit release representation of spinning MET system	6
1.3	Representation of the GPS constellation. Credits: The Aerospace	
	Corporation	8
1.4	Representation of the LISA mission. Credits: NASA	S
1.5	Illustrative TSS representation. European Space Agency ESA	9
1.6	Tethered Satellite System representation	10
1.7	Rod model scheme	11
1.8	Discrete model scheme	12
1.9	Artistic representation of MARSIS mission. Credits: NASA	15
1.10	TSS1 tether control mechanism. Credits: NASA	18
2.1	ECI reference frame	24
2.2	Perifocal reference frame	25
2.3	Local Orbital Reference Frame	26
3.1	Rotating reference frames	31
3.2	Modeling scheme of the tethered satellite system	36
3.3	Schematic representation at a generic instant during the deployment	
	process	36
3.4	Schematic representation of the fully deployed system	37
3.5	Modeling and discretization process	38
3.6	TSS discretized model	39
3.7	TSS rod model	41
3.8	Main elements of the mathematical model	43
3.9	TSS modeling at a generic instant	46
3.10	Rigid tether model	50
4.1	Schematic representation of the code's structure	57
5.1	Illustrative representation of the radial configuration $\hat{\ }$	61
5.2	Radial configuration: evolution of the x-coordinate (ℓ_1)	62

5.3	Radial configuration: evolution of the y-coordinate $(\hat{\ell}_2)$	63
5.4	Radial configuration: evolution of the z-coordinate $(\hat{\ell}_3)$	63
5.5	Illustrative representation of the along-track configuration	65
5.6	Along-track configuration: evolution of the x–coordinate $(\hat{\boldsymbol{\ell}}_1)$	66
5.7	Along-track configuration: evolution of the y-coordinate $(\hat{\boldsymbol{\ell}}_2)$	66
5.8	Along-track configuration: evolution of the z-coordinate $(\hat{\boldsymbol{\ell}}_2)$	67
5.9	Illustrative representation of the cross-track configuration	68
5.10	Cross-track configuration: evolution of the x–coordinate $(\hat{\boldsymbol{\ell}}_1)$	69
5.11	Cross-track configuration: evolution of the y-coordinate $(\hat{\ell}_2)$	69
5.12	Cross-track configuration: evolution of the z-coordinate $(\hat{\ell}_3)$	70
	Cross-track configuration: evolution of the x-coordinate $(\hat{\ell}_1)$ over	
	5 periods	71
5.14	Cross-track configuration: evolution of the y-coordinate $(\hat{\ell}_2)$ over	
	5 periods	71
5.15	Cross-track configuration: evolution of the z-coordinate $(\hat{\ell}_3)$ over 5	
	periods	72
	TSS modeling at a generic instant	73
5.17	Time evolution of the material coordinates describing the position	7.4
F 10	of the satellites along the tether	74
	Time evolution of the tether length $\dots \dots \dots \dots \dots$	75 76
	Radial configuration: evolution of the x-coordinate (ℓ_1)	
	Radial configuration: evolution of the y-coordinate (ℓ_2)	76
	Radial configuration: evolution of the z-coordinate (ℓ_3)	77
	Along-track configuration: evolution of the x-coordinate (ℓ_1)	78
	Along-track configuration: evolution of the y-coordinate (ℓ_2)	78
	Along-track configuration: evolution of the z-coordinate (ℓ_3)	79
5.25	Cross-track configuration: evolution of the x-coordinate $(\hat{\ell}_1)$	80
5.26	Cross-track configuration: evolution of the y-coordinate (ℓ_2)	80
5.27	Cross-track configuration: evolution of the z–coordinate $(\hat{\ell}_3)$	81
6.1	Conceptual scheme of the PID controller	84
6.2	Rod model: In-plane and out-of-plane angle	85
6.3	Discrete model: In-plane and out-of-plane angle	85
6.4	Radial configuration: time evolution of the in-plane angle	87
6.5	Radial configuration: time evolution of the out-of-plane angle	87
6.6	Radial configuration: time evolution of the tether length	88
6.7	Radial configuration: in-plane control torque	89
6.8	Radial configuration: out-of-plane control torque	89
6.9	Controlled radial configuration: time evolution of the x-coordinate ℓ_1	91
6.10	Controlled radial configuration: time evolution of the y-coordinate ℓ_2	91

6.11	Controlled radial configuration: time evolution of the z-coordinate $\hat{\ell}_3$ 92	
6.12	Along-track configuration: time evolution of the in-plane angle 93	
6.13	Along-track configuration: time evolution of the out-of-plane angle 93	
6.14	Along-track configuration: in-plane control torque 94	
6.15	Along-track configuration: out-of-plane control torque 94	
6.16	Controlled along-track configuration: time evolution of the x-coordinate	
	$\hat{\ell}_1$	
6.17	Controlled along-track configuration: time evolution of the y-coordinate	
	$\hat{\ell}_2$	
6.18	Controlled along-track configuration: time evolution of the z-coordinate	
	$\hat{\ell}_3$	
6.19	Cross-track configuration: time evolution of the in-plane angle 98	
6.20	Cross-track configuration: time evolution of the out-of-plane angle . 98	
6.21	Cross-track configuration: in-plane control torque 99	
6.22	Cross-track configuration: out-of-plane control torque 99	
6.23	Controlled cross-track configuration: time evolution of the x-coordinate	
	$\hat{\ell}_1$	
6.24	Controlled cross-track configuration: time evolution of the y-coordinate	
	$\hat{\ell}_2$	
6.25	Controlled cross-track configuration: time evolution of the z-coordinate	
	$\hat{\ell}_3$	

م مل مسه ما الرحمن الرحمي الرحمي الرحمي الرحمي الرحمي الرحمي الرحمي "وَابْتَغِ فِيمَا آتَاكَ اللَّهُ الدَّارَ الْآخِرَةَ وَلَا تَنسَ نَصِيبَكَ مِنَ الدُّنْيَا اللَّهُ الدَّارَ الْآخِرَةَ وَلَا تَنسَ نَصِيبَكَ مِنَ الدُّنْيَا اللَّهُ الدَّارِ الْآخِرَةَ وَلَا تَنسَ نَصِيبَكَ مِنَ الدُّنْيَا اللَّهُ الدَّارِ الْآخِرَةَ وَلَا تَنسَ نَصِيبَكَ مِنَ الدُّنيَا اللَّهُ الدَّارِ الْآخِرَةَ وَلَا تَنسَ نَصِيبَكَ مِنَ الدُّنيَا اللَّهِ اللَّهِ اللَّهُ الدَّارِ الْآخِرَةَ وَلَا تَنسَ نَصِيبَكَ مِنَ الدُّنيَا اللَّهُ الدَّارِ الْآخِرَةَ اللَّهُ الللَّهُ الللَّهُ الللَّهُ اللَّهُ اللْعُلْمُ اللَّهُ اللَّهُ اللَّهُ اللَّهُ اللَّهُ اللَّهُ اللَّهُ اللَّهُ اللَّهُ اللَّ

"وَابْتَغِ فِيمَا آتَاكَ اللَّهُ الدَّارَ الْآخِرَةَ ۖ وَلَا تَنسَ نَصِيبَكَ مِنَ الدُّنْيَا ۗ وَابْتَغِ فِيمَا آتَاكَ اللَّهُ الدُّنْيَا ۗ وَلَا تَبْغِ الْفَسَادَ فِي الْأَرْضِ وَأَحْسِن كَمَا أَحْسَنَ اللَّهُ إِلَيْكَ ۗ وَلَا تَبْغِ الْفَسَادَ فِي الْأَرْضِ إِنَّ اللَّهَ لَا يُحِبُّ الْمُفْسِدِينَ"

Chapter 1

Introduction to space tethers

1.1 Introduction

Space exploration and exploitation have grown exponentially over the past few decades, and this trend is expected to continue in the foreseeable future. Key areas of interest include communications, navigation and geo-localization, Earth remote sensing, planetary exploration, and space mining.

Equally important are the development of the space industry and the expansion of the space economy, as well as growing concerns related to security and defense - and increasingly, offensive capabilities. These developments highlight how space is rapidly evolving beyond being merely the "upper limit" of our world or the "house" of our stars; it has actually become a critical domain for human activity with economic, geopolitical and strategic implications. However, the current state of the art in space technologies cannot yet be considered fully mature to achieve the ambitious goals set by space research. Significant advancements are still needed, to make these objectives materially feasible and, above all, to improve mission scenarios in terms of cost-efficiency and risk reduction.

Both the high cost of launches and the growing issue of space debris are attracting increasing interest, as they are key factors in improving accessibility to space. Despite the progress made in recent years by reusable launch systems, the financial burden associated with sending payloads into orbit remains one of the barriers to widespread access to space. At the same time, the proliferation of space debris poses serious threats to the safety and sustainability, of current and future missions. Collisions with even small fragments can compromise satellites or crewed spacecraft, increasing operational risks and costs linked to collision avoidance systems. These two factors - launch expenses and space debris - exemplify the

kind of challenges that must be addressed to ensure a more accessible, secure, and economically viable space environment. Another critical aspect to be considered alongside these two issues is the overall cost of the missions themselves, particularly in terms of the required ΔV and, consequently, the amount of propellant needed. This requirement has a direct economic impact on the mission - not only due to the cost of the propellant itself, but also because of the additional mass, volume, and structural components necessary to store the propellant and support the propulsion system.

In this context, the concept of tethers is introduced. Tethers are high-strength, low density cables designed to connect satellites, probes and potentially even space stations. Tethers are structures with a relative small diameter, usually just few millimeters thick, and a length ranging from hundreds of meters to few kilometers. In order to ensure the structural integrity and satisfy the requirements in terms of mechanical properties, the choice of the material is of critical importance. This aspect - the choice of the material - will not be considered in this work, however a brief overview is given in the next few lines. Tethers are typically made of low-density, high-strength polymers. Among the requirements the most relevant are a high strength-to-weight ratio, radiation resistance, thermal resistance, flexibility and long-term life. Indeed, the choice has to allow to meet the stringent requirements regarding the total mass while still ensuring the required performance, enough resistance against the space radiations and temperature variations. In addition to that, flexibility and toughness are important for compact stowage, smooth deployment and the ability to absorb vibrations. A last, yet very important, material property is electrical conductivity which may or may not be required depending on the type of mission for which the tether is designed.

This property allows for the classification of space tethers into two main categories: conductive and non-conductive tethers. The first type features a conductive core which permit the tether to interact with the Earth's magnetic field, these are named Electrodynamic Tethers (EDT). On the other hand, non-conductive tethers serve a variety of purposes, such as Momentum Exchange devices or structural connectors in Tethered Satellite Systems (TSS).

1.2 Electrodynamic Tethers

The Earth possesses a geomagnetic field whose magnetic poles are approximately aligned with the geographic poles. The fundamental principle underlying the concept of electrodynamic tethers is to exploit the interaction between the system and the Earth's magnetic field. The key feature lies in the conductive core, which allows electric current to flow through it, enabling the system to interact with the geomagnetic field. It is possible to exploit the electric current generated within the

tether as a power supply for systems, scientific instruments or electric thrusters, thereby reducing or even eliminating the need for bulky onboard batteries. However, the most significant application arises from the interaction between this current and the Earth's magnetic field. According to the Lorentz force law, a force is exerted on a charged particle when it moves through a magnetic field. According to [1], the electric energy derives from a transfer of energy from the orbital motion of the system, effectively extracting the tether's kinetic energy and causing a gradual decrease in orbital altitude. In scenarios where the primary goal of employing an electrodynamic tether is to generate auxiliary electrical power during a mission, this altitude loss may represent an undesired side effect that must be actively compensated. Conversely, this phenomenon becomes particularly advantageous when the electrodynamic tether is employed for post-mission disposal or the controlled deorbiting of space debris. In such cases, the tether functions as a passive, propellant-free system capable of inducing atmospheric reentry solely through electromagnetic interaction, thereby offering a sustainable and efficient solution for orbital debris mitigation.

1.2.1 Space debris digression

In recent years, the issue of space debris has garnered increasing attention within the space community. A notable example and key turning point can be identified in the first-ever accidental in-orbit collision between two satellites [2]. In 2009 a private communication American satellite, Iridium-33, and a Russian military satellite, Kosmos 2251, collided at 11,7 [km/s]. The collision resulted in the generation of more than 2300 trackable fragments. For the first time, the space community witnessed the consequences of an collision in orbit, which helped underscore the severity of the orbital debris problem - a byproduct of about sixty years of human activity in space. According to [3]: in more than 60 years of space activities, more than 6050 launches led to 56450 tracked objects in orbit for a total mass of more than 9300 tonnes. About 24% of the cataloged objects are satellites, and only 8% are intact and operational - about 4000. This means that roughly 90% of space objects belong to the uncontrolled satellite class. About 11% are spent upper stages. Moreover, since 1961, over 560 in-orbit fragmentation events have been recorded. Of these, only seven were caused by collisions, while the vast majority resulted from explosions of spacecraft or upper stages. The main cause of these explosions is the presence of residual fuel in tanks or fuel lines, or other remaining energy sources still on board. However, collisions are expected to become the primary source of space debris in the future.

As an effort to mitigate this effects, the international space community has collaborated over the past decade to formulate and adopt guidelines aimed at

limiting the generation and accumulation of debris. Despite these efforts, recent analyses of the orbital environment have revealed a troubling trend, particularly in Low Earth Orbit (LEO) and Geostationary Earth Orbit (GEO).

Many simulations, in fact, suggest that, due to collisions caused by fragments generated by other collisions, the number of objects in orbit might grow, even when no further objects are added to space, [4]. This collisional cascading, highlighted for the first time in 1978 by Kessler and Cour-Palais [5] and become popular as Kessler syndrome, may potentially lead to a chain reaction situation, with no further possibility of human intervention.

Lately, studies conducted by Liou and Johnson [6] indicate that the LEO debris population has entered an unstable regime in which collisions among existing objects will continue to generate new debris, leading to a self-sustaining growth of the population over the next two centuries, even in the absence of additional launches. In practice, the outlook is more severe than the "no future launches" scenario, as satellite deployments are expected to persist and unexpected catastrophic breakups may still occur. Consequently, to ensure the long-term sustainability of near-Earth space activities, active debris removal (ADR) and post-mission disposal is now regarded as a necessary component of orbital debris management.

Within this context, electrodynamic tethers represent a promising solution for post-mission disposal. Their low cost, simplicity, and passive operation make them particularly attractive for rapid and efficient deorbiting, especially for satellites in low Earth orbit. The force generated by the interaction between the current flowing through the conductive core and the Earth's magnetic field represents a highly promising tool for enabling low-power atmospheric reentry. It is noteworthy that the direction of resulting magnetic force depends on the polarity of the current: if the polarity is inverted, the force can also accelerate the spacecraft in the direction of its orbital velocity. Generally, this capability would enable orbital maneuvers without the use of propellant and has promising applications especially in what concerns satellite end-of-life strategies. The operational effectiveness of such systems, however, is strongly influenced by the orbital parameters of the mission. In particular, the altitude and inclination of the orbit determine the intensity of the local Earth's magnetic field and the density of the ambient plasma in which the system operates. This parameter is of critical importance, since the current induced along the tether is generated through interaction with the surrounding plasma. The plasma, in fact, acts as a medium to complete the electrical circuit, functioning both as the source from which electrons are collected and the sink into which they are emitted.

Related to the presence and density of plasma required for the operation of electrodynamic tethers, an interesting potential application can be highlighted. In

fact, applications of electrodynamic tethers have also been explored for other planetary environments. For instance, Gallagher et al. (1998) [7] investigated feasibility of the use of an electrodynamic tether for propulsion and power generation for a spacecraft in the Jovian system, leveraging Jupiter's strong magnetic field and the high relative velocities between the magnetic field itself and the spacecraft.

1.3 Momentum exchange tethers

Momentum Exchange Tethers (METs) can be considered as an innovative alternative for space propulsion systems. The system is based on the use of long, rotating or stationary cables to transfer momentum between the payloads at the ends of the tether. Unlike conventional propulsion methods, METs rely on angular momentum transfer to enable orbital changes for payloads without requiring on-board propellant, thereby significantly reducing mission mass and launch costs. Two notable types of momentum exchange tethers include the following:

• Spinning momentum exchange tethers:

Since the semilatus rectum of the orbit is proportional to the square of the angular momentum magnitude, the larger its value, the farther the orbit passes from the attracting center. During the rotation of a space tether system of constant length, its total angular momentum remains constant, while the angular momenta of each of the bodies connected by the tether change. There is a continuous redistribution of the magnitude of the angular momentum between the connected bodies, while the overall angular momentum of the system, which coincides with the value of angular momentum of the Center of Mass, remains constant. Cutting the tether stops this redistribution, and the further free motion of the bodies is determined by the magnitude of the angular momentum that they had at the time of cutting.

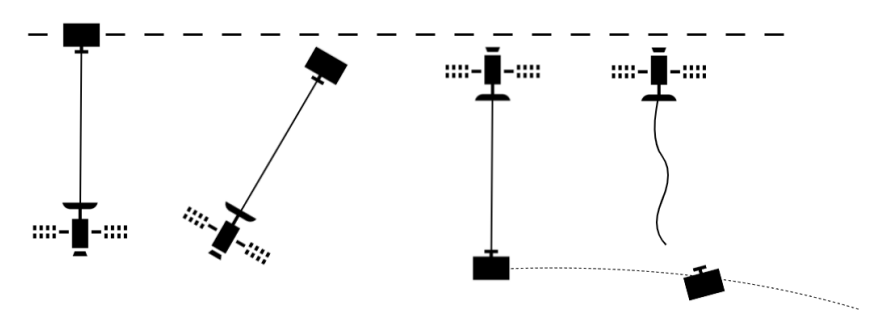


Figure 1.1: Spinning based Momentum Exchange Tether System

This effect can be used to increase or decrease the height of the end bodies' orbits. For instance, when the upper payload is released from a tether, it

carries more angular velocity than it requires to stay on that circular orbit of the Center of Mass of the system. Since the upper payload does not have enough energy to escape the Earth's gravity, and considering that there is an excess of angular momentum, the upper payload goes into an elliptical orbit with the release point being the perigee of the orbit. [8]

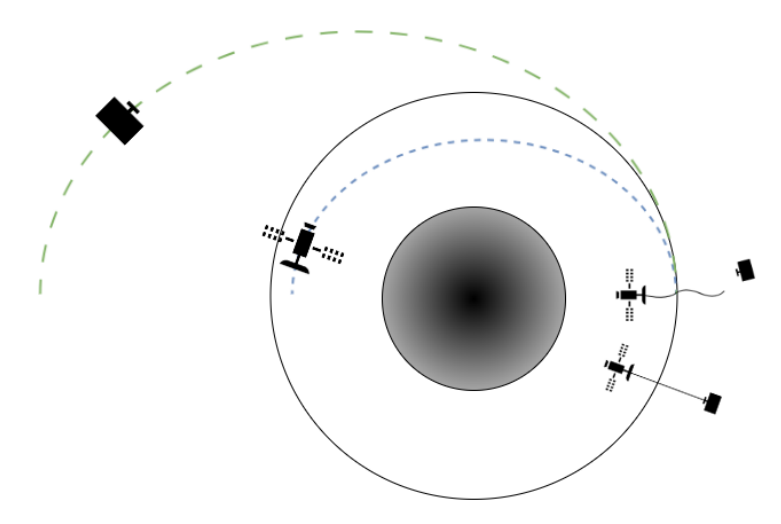


Figure 1.2: Orbit release representation of spinning MET system

Similarly, once part of the system has been released, what remains of the system does not have enough angular velocity to stay on its circular orbit when it is released and so the lower end body and the tether go into an elliptical orbit, too, but this time the release point would be the apogee of the orbit. One of the alternatives to restore the orbit of the system after the release of the upper payload, would be to explore the use of an electrodynamic tether as a spinning momentum exchange tether.

Nevertheless, it remains noteworthy that this system allows for the upward and downward transfer of masses released from a hanging tether

An example of a potential application of METs is in the development of space transportation systems. A space systems architecture was developed to enable repeated payload transport between low Earth orbit and the lunar surface with minimal reliance on propellant by Hoyt and Uphoff [9]. A system, for orbital transfers between Earth and Mars, comprising two rotating tethers in highly elliptical orbits around each planet has been devised by L. Forward and Nordley [10]. According to their work, at Earth the payload is picked up near periapsis and, following half a rotation it is released at a velocity sufficient to place it on a high-speed transfer trajectory toward Mars. Upon arrival, the payload is intercepted near Mars periapsis and subsequently released on a suborbital reentry path.

• Variable length exchange momentum tethers:

The redistribution of the angular momentum between the elements of a space tether system can be carried out also by changing the tether length. The greater the length of the tether, the stronger the redistribution of the angular momentum between the connected bodies [11]. It is noteworthy also that varying the tether's length leads to the appearance oscillations of the system. These oscillations must be carefully analyzed and controlled, as they can significantly influence the stability and efficiency of the tether dynamics.

Overall, whether the objective is to enable orbital transfers or to facilitate atmospheric re-entry and post-mission disposal, tethers have demonstrated considerable potential as green, propellant-less solutions. In addition, tethers can also serve as structural components within distributed space systems. In particular, they are a distinctive feature of Tethered Satellite Systems (TSS), where two or more satellites are physically connected via long cables.

1.4 Distributed Space Systems

A Distributed Space System is a system composed of several spacecrafts. Unlike traditional missions, where all the goals and requirements are integrated into a single central spacecraft, in a Distributed Space System functions are decentralized across the multiple elements composing the system, which work together to accomplish the given mission. During the last decades these systems have attracted increasing interest, since they offer significant improvements both in terms of cost and performance optimization. Usually, these systems are composed by small satellites, instead of the more known large spacecrafts. As an immediate consequence the missions would be able to accomplish the goals being much less expensive in all the aspects and stages of the mission, from launch to orbit control and eventual maneuvers. With the proliferation of CubeSats and other small satellites, DSSs have become increasingly attractive for both governmental and commercial space missions.

As highlighted by Aliberti in his work [12], from an operational point of view the intrinsic characteristics of this architecture guarantee a major flexibility and robustness. Indeed such an architecture could be easily scaled, adapted and reconfigured for different scenarios and missions with different requirements, keeping the same level of efficiency, reliability and fault-tolerance. Especially, it is noteworthy that given the independence of the spacecrafts, the failure of the single element of a constellation does not necessarily compromise the functions of the remaining elements. In this context, the loss of a single element may indeed degrade overall mission performance; however, such degradation is significantly less severe compared to the failure of a centralized satellite that concentrates all functionalities

into a single platform.

Distributed Space Systems are commonly classified into four main categories, based on the level of coordination and interdependence among the elements:

• Constellation:

The most known and common type are satellite constellation. This typology is already active, widely used and plays a key role in our quotidian life. A constellation consists of a group of satellites whose orbits are designed in order to have a coordinate coverage without having a control of the relative positions. The orbits of the satellites are designed to ensure the desired spatial and temporal coverage. These type of DSS finds the most important application in what concerns global positioning and communications.

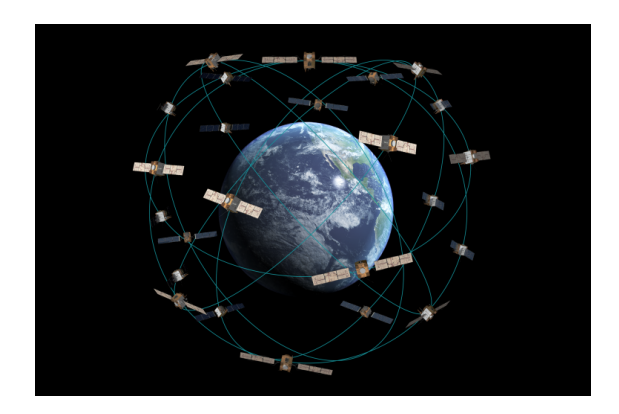


Figure 1.3: Representation of the GPS constellation. Credits: The Aerospace Corporation

• Swarm:

Space swarms are large-scale type of distributed space system composed of a very high number of small, relatively simple satellites that operate collectively to accomplish a common objective [13].

• Formation:

Formation flights are quite similar to constellations, but with a key difference: the monitoring of relative positions. Formation flight, in fact, refers to a class of distributed space systems in which multiple satellites orbit in coordination while maintaining precise relative positions. The objective of such an arrangement is to enable the satellites to function collectively as a single, large-scale virtual instrument, thereby achieving performance and capabilities that would be difficult or impossible for a single spacecraft to achieve on its own.

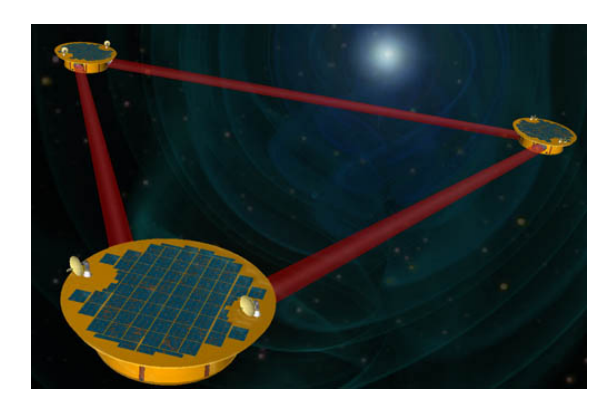


Figure 1.4: Representation of the LISA mission. Credits: NASA

• Tethered:

This specific type of DSS is particularly interesting, as the satellites that make up the system are physically connected to each other through a cable, and it will be at the heart of the analysis conducted in this thesis.



Figure 1.5: Illustrative TSS representation. European Space Agency ESA

The concept emerges from mission scenarios in which the system components are required to maintain significantly closer relative distances compared to the previous DSS architectures. Moreover, these missions typically demand precise control of the relative positions between the elements. In such cases, implementing a formation-flying or swarm-based configuration would result in substantial control effort and complexity. This is primarily due to the high level of precision typically required, combined with the fact that each element is individually subject to perturbations that influence its dynamics. Consequently, this would necessitate extremely accurate position and attitude determination systems, as well as high-performance control mechanisms, both of which would incur considerable costs. The use of a mechanical connection,

such as a tether, offers a promising alternative. It effectively eliminates the need for complex and expensive relative position control systems, since the relative positions and distances between the various elements are physically constrained aside from potential structural deformations of the system, which can be addressed with a lower expenditure.

However, despite the advantages, the dynamics of tethered systems are inherently complex. The presence of long, flexible cables introduces nonlinearities, coupling between translational and rotational motion, and sensitivity to external perturbations. The following section presents a comprehensive overview of the modeling approaches for these systems.

1.4.1 Tethered Satellite Systems

As shown in 1.5, a Tethered Satellite System (TSS) consists fundamentally of a space tether connecting two masses. Based on the mission profile and goals, the end-masses of the system could either be two satellites of similar or even identical size and mass. Alternatively, in a different scenario, the system may include a mother satellite and a sub-satellite, equipped with the appropriate instrumentation and systems to perform specific tasks defined within the mission.

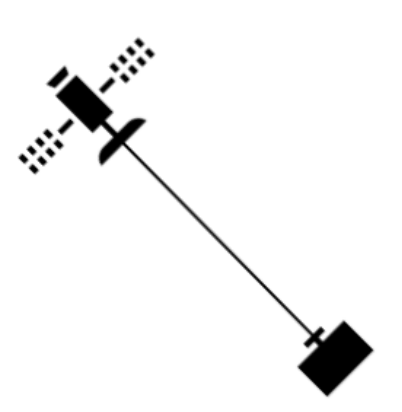


Figure 1.6: Tethered Satellite System representation

To gain insight into the dynamics of the system and analyze how it behaves under operational conditions, it is essential to develop a reference model able to accurately represent the system. Such a model serves as the foundation for both analytical investigations and numerical simulations, allowing to study system responses, assess performance, and evaluate the impact of external disturbances or control strategies. In fact, the space environment is characterized by a large number of perturbation factors - e.g., air drag force, the Earth's oblateness, represented

by the J_2 perturbation, solar pressure, heating effect. In addition to these external factors, attention must also be given to internal phenomena, primarily related to the tether. The tether itself exhibits inherently complex mechanical behavior, mainly due to elastic deformation and internal damping.

The choice of the modeling approach depends on the aspects to be analyzed, the level of accuracy required, and the computational effort considered acceptable. For the TSS, three reference models are typically considered [14], [15], [16]:

- Rod model:

The model - commonly referred to as dumbbell model - is considered to be the simplest approach developed over decades of research on space tether systems. A graphical representation is given in 1.7. In its basic formulation, the model reduces the system to two point masses connected by a rigid rod. Depending on the specific needs of the research, it is possible to assume either a massless tether - where the rod connecting the end masses is considered to have no mass - or a massive tether. In the second case, the tether is assumed to be straight and inextensible, uniform in mass and a slight modification of the initial parameters leads to a more complex - yet still relatively simple - set of governing equations. Typically three degrees of freedom are considered: the in-plane angle θ , the out-of-plane angle ϕ , and the deployed tether length L. These three parameters are usually selected as the generalized coordinates, leading to three dynamics equations that will be discussed in detail in 3.3.2.

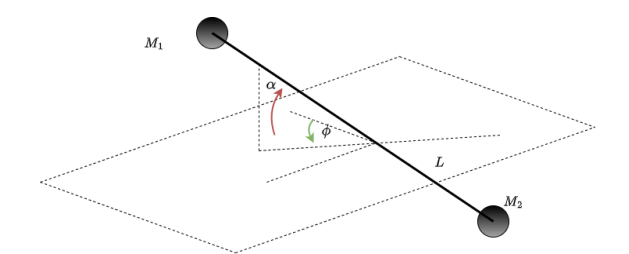


Figure 1.7: Rod model scheme

By modeling the tether as a rigid body, the main advantage lies in the simplicity of the system, resulting in a significant reduction in the complexity of the governing equations. This model is typically employed for simplified analyses when the tether remains taut due to an appropriate external force (e.g., a control force or gravity gradient), a condition that is not always guaranteed in realistic scenarios. Therefore, while it provides a useful framework for preliminary studies, its validity must be carefully assessed depending on the specific operational context. In cases where the application is particularly demanding in terms of accuracy and the need to understand the deformation

of the tether the rod model - given its inherent inability to account for internal elastic phenomena - would not be adequate.

- Discrete model:

To overcome the limitations of the rod model, the discrete model is introduced, as it represents a more suitable compromise between the fidelity of the system representation and the associated computational and analytical cost. As represented in 1.8, the model is developed by dividing the tether into a series of mass points connected by massless spring-damper elements. Usually, the tether is divided into a series of segments of equal length. Each segment is, then, represented by a point mass - located at its center of mass - corresponding to the total mass of the segment. The parameters of the spring-damper elements are selected based on the mechanical properties of the material from which the tether is made. These aspects will be further examined in a 3.3.1.

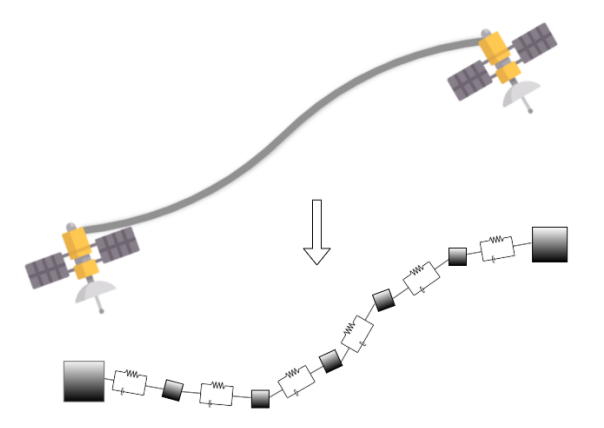


Figure 1.8: Discrete model scheme

Within this framework, the total number of degrees of freedom under analysis is directly related to the number of lumped masses chosen for the tether discretization, with each mass contributing three translational degrees of freedom. Consequently, this approach enables the analysis not only of the motion of the end bodies, but also of the response of each individual lumped mass, thereby capturing the overall behavior of the tether. Gaining insight into a greater number of degrees of freedom automatically enables a more accurate and comprehensive characterization of the system's dynamic behavior, capturing not only the influence of external perturbations but also internal effects such as elastic deformations, configuration changes, and variations in deployment velocity, all of which may induce significant distortions in the tether shape.

- Continuous model:

Finally, by further increasing the level of fidelity in the system representation, we find the continuous model. In this formulation, the tether is modeled as a truly continuous entity, without mass lumping or segmentation. While this approach would offer the most accurate theoretical description of the tether's behavior, it leads to a highly complex dynamic analysis and a significantly higher computational cost. For these reasons, the continuous model finds limited applications.

1.5 Further suggested applications of tethers

As outlined in the previous introductory sections, tether systems represent a promising solution to few important challenges in the space sector: post-mission disposal or active space debris removal, as well as the development of sustainable propulsion alternatives and the construction of tethered platforms. However, tether systems also hold potential as a possible solution to a broader range of research questions. Among these, it worth mentioning the detection of gravity waves, measurement of the Earth's atmospheric properties or other explored alternatives as generation of electromagnetic waves by an orbiting electrodynamic tether [17], collection of samples from micro-meteoroids, comets and asteroids [18], novel tether-based approaches for docking and close rendezvous maneuvers [19], and passive attitude stabilization of spacecraft [20].

Very interesting, in addition to what has just been mentioned, is the use of space tethers for the so called space elevators. Around the 1960s Yu Artsutanov, inspired by an idea originally proposed by Tsiolkovsky in 1895 [21], formulated for the first time the concept of such a system [22]. The concept of a space elevator essentially involves a space tether system connecting the Earth's surface to a space station positioned beyond the geostationary orbit. The function of moving a payload from the first station at the Earth's surface to the second one in orbit is carried out by special climbers that move along the tether. This operating mechanism implies that the primary energy expenditure is associated with the movement of the climbers. In essence, the main energy cost lies in changing their gravitational potential energy as they ascend or descend along the tether.

The first studies that have been conducted concluded that the available technology was not yet mature enough to develop materials with the required properties to ensure the structural integrity of the system [22],[23]. In addition to material limitations, several critical challenges could be identified, including the generation of sufficient energy to change the altitude of the climbers, as well as the need to address environmental threats such as impacts with micro-meteoroids or low-Earth orbit debris and lightning strikes [24]. More recent studies, however, have

addressed the main challenges by proposing innovative solutions, analyzing the dynamics and stability, and introducing new concepts, as the partial space elevator, which is a radially oriented space tether system connecting two space stations [25], [26].

Finally, it is both appropriate and preparatory to the core analysis of this thesis to mention, among the potential applications of tethers, space-based radar sounding. A more in-depth analysis will be provided in the following section.

1.6 Space based radar sounding

This thesis will primarily draw upon the work of Aliberti, Quadrelli, and Romano on a distributed space-based radar sounder [27]. Nonetheless, it is important to acknowledge the existence of other studies related to space-based radar sounding, which have explored alternative approaches to addressing challenges in this field [28].

Fundamentally, the idea is to observe planetary bodies using sensors placed in orbit, leveraging the privileged point of view that such a position can offer. Among the various options for observing the Earth from above, orbital observation is undoubtedly the most complex and expensive to implement, especially when compared to alternatives that allow for closer range sensing - such as drones or other aerial platforms (e.g., high-altitude balloons). However, it is considered a highly promising approach and has seen significant advancements in recent years. Moreover, for observations of other celestial bodies - such as the Moon, Mars, and, in the future, potentially other planets and their satellites - orbital sensing represents the most viable and effective option available. Depending on the type of antenna used, and more specifically the frequency band selected for sensing operations, different objectives can be pursued. For instance, low-frequency sensing enables sub-surface analysis, which serves as the primary application considered in this work to motivate the subsequent analysis of dynamics and deployment strategies discussed in later sections. Examples of missions that employed radar sounders for subsurface investigations include the Apollo Lunar Sounder Experiment (ALSE) [29], the Mars Advanced Radar for Subsurface and Ionosphere Sounding (MARSIS) onboard ESA's Mars Express mission [30], and the Japanese SELENE (Kaguya) lunar orbiter [31]. On the other hand, higher-frequency sensing is typically used for surface remote sensing, allowing for the acquisition of highly detailed satellite imagery.

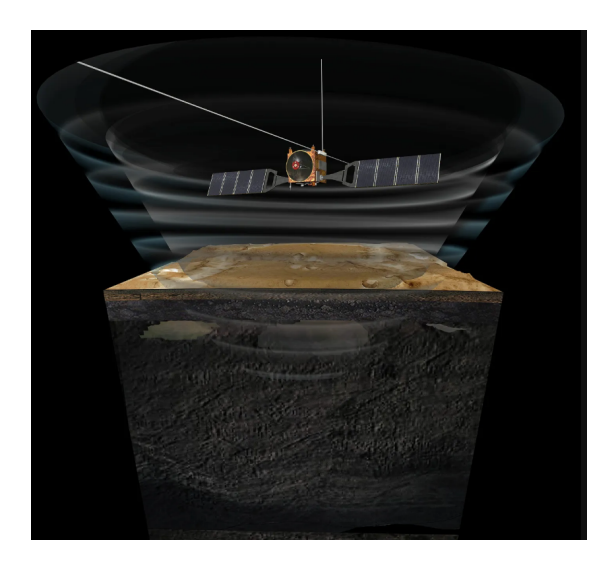


Figure 1.9: Artistic representation of MARSIS mission. Credits: NASA

The technological landscape in which this concept evolved has traditionally relied on systems consisting of an antenna mounted on a single orbiting satellite. However, achieving the desired performance with such systems would require antennas of large dimensions that would be incompatible with the constraints of a space mission in terms of mass and size. For this reason, research efforts have focused on developing solutions able to improve, by relying on innovative concepts, the performance of such systems. In particular, thanks to the recent technological advancements, these efforts have led to the conception of an approach based on synthesizing large antenna apertures by employing arrays of small satellites flying in carefully coordinated orbital formations. For example, Carrer and Rovolo in their paper [28] have demonstrated that such a configuration improves performance in the following areas:

- 1. reduce the influence of surface clutter;
- 2. increase the across-track resolution;
- 3. increase the signal-to-noise ratio (SNR)
- 4. provide greater flexibility in the processing of signals acquired by the different sensors.

In line with the ongoing need to improve the performance of such systems and to propose innovative solutions, Aliberti, Quadrelli and Romano have proposed an alternative designed to address the main challenges associated with a formation flying radar sounding system. These challenges can be summarized as follows:

- 1. Precise determination of the relative positions between the satellites within the formation is needed in order to enable proper signal processing and ensure the overall performance of the radar system;
- 2. The temporal evolution of aperture is inherently constrained by orbital dynamics, especially by external perturbations such as atmospheric drag, solar radiation pressure, and gravitational anomalies;
- 3. The temporal evolution of the dynamics is, moreover, constrained by the inherently limited availability of onboard propellant, which restricts the extent of active maneuvering and the capability to compensate for configuration deviations;
- 4. Achieving the high level of precision required typically necessitates the use of advanced satellite platforms properly equipped to perform accurate and coordinated adjustments.

The solution explored in their work is able to address the aforementioned issues through the use of a Tethered Satellite System (TSS). Indeed, the structural mechanical connection provided by the tether acts as a much stronger constraint significantly reducing, or even eliminating, the costs required to maintain the relative positioning of the individual elements within a typical formation flying configuration.

The innovative aspect in their approach lies in the specific configuration intended for the system during the data acquisition phase of the mission. Unlike earlier studies, which primarily focused on naturally stable configurations - more precisly the naturally gravity gradient stabilized radial configuration - Aliberti explored and confirmed the feasibility of maintaining the system stability in the cross-track configuration, which is oriented perpendicularly to both the radial and along-track directions. In particular, in [27] two stabilization strategies are proved to be reliable: gyroscopic stabilization and aerodynamic stabilization, the latter being particularly effective at low altitudes. However, the feasibility of such a mission still depends on a second factor of no less importance: a successful deployment to the final configuration. Building upon their analysis, this thesis further investigates the dynamics of tethered systems with a focus on the study of the deployment phase, aiming to contribute to overcoming this critical obstacle.

1.7 Tethered Satellite Systems Deployment

Regardless of the specific configuration or intended application, all tasks involving a Tethered Satellite System (TSS) begin with the deployment of the tether,

which is therefore the first essential step to achieve the system's operational configuration. However, the deployment phase is often the most critical in missions involving TSS. Indeed, numerous tether missions have failed due to incomplete or unsuccessful deployment. These failures and difficulties in the deployment have significantly hindered the broader adoption of tether technology in space missions. Consequently, research interest in this area remains particularly strong, as it is considered crucial to open the door to a large-scale use of tether systems in space missions. To contextualize this ongoing effort, the following subsections will first examine two well-known mission failures directly related to unsuccessful deployment, and will then present the current state of the art in strategies aimed at ensuring the stabilization of this crucial phase.

1.7.1 Notable Cases of Deployment Failure in TSS Missions

The first mission to give concrete expression to interest in Tethered Satellite Systems (TSS) was the NASA/ASI (Italian Space Agency) Tethered Satellite System (TSS-1). In 1984, an agreement between the two space agencies was signed, outlining the mission objectives as follows: to evaluate the capability for deploying, controlling and retrieving a tethered satellite; to validate predictions of the dynamic forces in such systems; to investigate the electrodynamic interaction of a conductive core, and to demonstrate the capability of the system to serve as a facility for research in geophysical and space physics. The Tethered Satellite System-1 (TSS-1) consisted of a satellite, a 20 km long tether - with electrically conducting copper strands in its core - with a 2.54 mm diameter, and a deployer in the Shuttle's cargo bay. Specifically, the mission was conducted during the STS-46 Shuttle Flight. Given the technology available at the time, it was impossible to predict exactly how the system would perform in space prior to the mission. The deployment and retrieval of the tether relied on a tether control mechanism schematized in 1.10, and these stages represented the greatest sources of uncertainty for the designers.

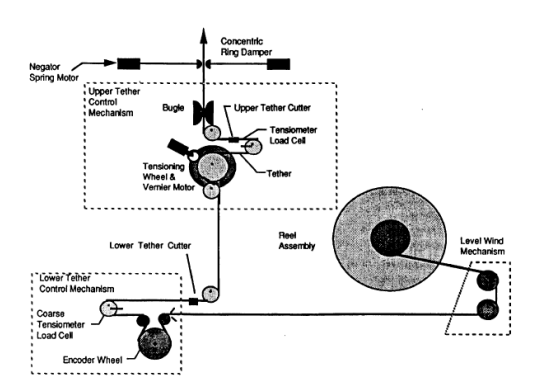


Figure 1.10: TSS1 tether control mechanism. Credits: NASA

As it turned out, the fatal obstacle to the success of the mission was, indeed, the deployment phase. The mission failed primarily because full deployment of the tethered satellite was not achieved. The investigation committee, which was tasked with analyzing the mission (TSS-1 CIB), identified five flight anomalies, all related to the tether and its deployment. According to the NASA report [32] the three main failures are here reported as follows:

- Unplanned Tether Deployment Stop at 179 Meters;
- Unplanned Tether Deployment Stop at 256 Meters;
- Failure to Move Tether in Either Direction at 224 Meters;

The review focused mainly on structural aspects, identifying a series of mechanical blockages - related to the wind-level mechanism - as the cause of the failures. It also recommended a more careful and precise analysis of the loads, taking into account the interactions among the various system components, as well as the use of ground testing procedures that more accurately replicate the in-orbit scenario.

Even with its limited deployment, TSS-1 provided significant information regarding the deployment and retrieval phases, and it paved the way for subsequent missions aimed at more successfully testing the use of tethered satellite systems. In this context, it is worth mentioning the TSS1-R mission [33], a reflight of the first mission conducted four years later, which achieved improved results but failed shortly before reaching the final tether length due to tether breakage caused by electrical discharge. The investigation committee, in this case, affirmed that the high-voltage systems must be better understood and managed in missions involving electrodynamic tether applications. More recent missions include the Young Engineers' Satellite 2 (YES2) of ESA and DLR[34] and the JAXA's Konotori Integrated Tethered Experiment (KITE) [35]. The former was a demonstrative mission

for the re-entry of a light-weight capsule by the use of a tether rather than a conventional retro-rocket and was launched after the failure of Young Engineers' Satellite (YES) mission. The latter was intended to deploy a 700 m length tether from the H-II Transfer Vehicle(HTV), but it failed to accomplish its mission objectives due to a technical malfunction.

These missions collectively highlight the technical challenges associated with tether deployment, ranging from mechanical blockages and system malfunctions to tension management and electrical discharge. They underscore the critical need for robust and reliable control strategies capable of handling systems dynamics, as well as ensuring stability under different operational conditions. Thus, the next subsection presents the state of the art and the main advancements in tether deployment control and stabilization.

1.7.2 State of the Art in Tether Deployment and Stabilization

In recent years, substantial progress has been achieved through numerical simulations and ground-based testing, contributing to a deeper understanding of tether dynamics under real orbital conditions. Furthermore, building upon the achievements and failures of previous space tether missions, various control methods for tether deployment have been devised.

One of the earliest approaches proposed for stabilizing tether deployment was the tension control law developed by Rupp [36], which became a cornerstone in the early studies on tethered systems. Many controllers subsequently developed following this work proved effective, yet most of them were primarily designed to regulate deployment in planar motion, thus limiting their applicability. Following this line, for example, Aslanov introduced a tether length control law based on the swing principle for payload delivery to Earth's surface [37]. Among the tension-based approaches, Pradeep proposed a linear tether tension control law that successfully addressed some of the main limitations of earlier methods [38]. This controller was further refined by Zhu and Murugathasan, who optimized its performance by tuning the control gains, thereby achieving a faster deployment rate [39]. Despite these advancements, optimized linear tension controllers remained sensitive to initial conditions and exhibited only a limited domain of stability. In the past decade, more advanced controllers have been introduced. The Linear Quadratic Regulator (LQR) approach, applied by Kojima and Taruoka, demonstrated effective control and deployment of the tether, although the process remained relatively slow [40]. More recently, significant progress has been achieved with Sliding Mode Controllers (SMC), which are particularly well-suited for handling the nonlinearities inherent in tether dynamics. Building upon this framework, Kang et al. proposed a fractional-order SMC that further enhanced robustness and adaptability [41].

The aim of all of this advancements, together with the progressive introduction of increasingly accurate system models, is not only to reduce the risk of mission failure but also to establish more reliable methodologies for predicting and managing tether behavior across the wide range of operational scenarios. Nevertheless, one of the challenges that remains only partially addressed is tether deployment outside the orbital plane of motion, which represents an essential step for the application from which this research originates. Accordingly, the primary objective of this thesis - and its main original contributions - would be to further investigate the deployment dynamics of a tethered satellite system, with the ultimate goal of achieving a fully deployed cross-track configuration - in which the tether is oriented perpendicularly to the orbital plane. The study will not be strictly confined to deployment along the cross-track direction; nevertheless, alternative pathways will also be explored, taking under consideration more stable and cost-effective options, such as the deployment in the orbital plane already explored in the literature. This will be done with the aim of characterizing the system dynamics in terms of control effort and stability for each of these alternatives. Ultimately, the results presented may serve as a foundation for more detailed future analyses of control algorithms and potentially for a experimental validation phase, thereby providing the necessary foundation for future in-orbit demonstrations.

1.8 Work Subdivision

The research was carried out out partly in Turin and partly in Buffalo, under the supervision of PhD candidate Stefano Aliberti and Dr. Eleonora Botta, Associate Professor at the State University of New York at Buffalo; it also follows part of the projects led by Dr. Marcello Romano - former full-time Professor at the Polytechnic University of Turin - within the activities of the ASTRADORS group.

This section is intended to provide an outline of the workflow followed in this research, to help guide the reader through the various chapters, and to briefly summarize the content of each chapter. The content of this thesis is divided into the following chapters:

- Chapter 1 Introduction: provided a general overview of space tethers and their applications, starting from Electrodynamic Tethers (EDTs) up to Tethered Satellite Systems (TSS). This progression leads to the application that motivates the present study, namely space-based radar sounding using tethered satellite systems, and introduces the main challenges related to their deployment.
- Chapter 2 Notation and Mathematical Tools: introduces the mathematical framework and notation employed throughout the analysis.

- Chapter 3 Mathematical Model: develops the dynamic modeling of the tethered satellite system, including external and internal forces, different tether representations, and the formulation of the equations of motion, with specific attention to deployment effects.
- Chapter 4 Numerical Simulation: describes the implementation of the simulation environment, detailing the code structure in its main phases: the initialization of parameters, the integration of the equations of motion, and the post-processing procedures.
- Chapter 5 Numerical Results: after a brief introduction of the physical parameters of the system under analysis, presents and discusses the outcomes of the first simulations, offering a baseline picture of the inherent tendencies of the system. It analyzes the system dynamics in the absence of deployment maneuvers and subsequently in different deployment configurations, highlighting the main challenges that arise in each case.
- Chapter 6 Deployment Strategies: explores potential deployment strategies, first by evaluating the required control effort through a simplified preliminary simulation of the dynamics using the rod model. Subsequently, an equivalent control action is applied to the lumped-masses model to assess its effectiveness within a framework that more faithfully reproduces the system's actual behavior under real conditions.
- Chapter 7 Conclusions and Future Work: briefly summarizes the main activities carried out throughout the work, focusing on the key findings, while also suggesting possible directions for further investigations on the Tethered Satellite Systems.

Chapter 2

Notation and Mathematical Tools

In order to carry out a rigorous and accurate analysis of any phenomenon or system, it is fundamental to clearly define and understand the set of tools that will be employed throughout the study. Relying on mathematics enables us to comprehend the physics of the system and to understand its behavior and responses to both internal and external agents, arising from the environment in which it operates. The purpose of this chapter is, therefore, to introduce the tools that make up the the mathematical framework adopted to represent the system, along with the notation that will be used to denote each of these tools.

2.1 Vectors and Unit Vectors

We begin by introducing the basic mathematical tools employed in this analysis. Vectors represents a certain quantity characterized by an amplitude and direction, and they play a central role in the representation of physical phenomena within a three-dimensional space. They are typically expressed through three distinct components, defined with respect to a given reference system. On the other hand, unit vectors, commonly referred to as versors, are a specific category of vectors. They are characterized by having unit magnitude and, like all vectors, must be defined with respect to a reference frame. Their primary function is to identify a particular direction and consequently they are fundamental to construct and define reference frames.

The notation used in this work is the following:

- A bold letter, v, represents vectors;
- Versors will be represented with the notation: $\hat{\mathbf{v}}$.

2.2 Reference Frames

Reference frames are the indispensable elements for orienting ourselves in analytical studies. It is essential to define each reference frame clearly and consistently, ensuring coherence throughout the analysis. Indeed, the choice and formulation of these reference frames can significantly simplify both the initial setup of the analysis and the subsequent post-processing phase, enhancing clarity and computational efficiency. By establishing a set of mutually orthogonal unit vectors, one can define a reference frame suitable for the analysis of physical phenomena. Each reference frame, generally denoted by \mathcal{F} , will be distinguished by a subscript that identifies the specific frame being referred to. While the vectrix representation of a reference frame \mathcal{F} , used to indicate the set of unit vectors that define its orientation in space, is denoted by the symbol $\hat{\mathcal{F}}$.

Considering a set of three perpendicular unit vectors, $\hat{\mathbf{a}}_1$, $\hat{\mathbf{a}}_2$, $\hat{\mathbf{a}}_3$, the vectrix formulation is the following:

$$\hat{\mathcal{F}}_a \triangleq \begin{bmatrix} \hat{\mathbf{a}}_1 & \hat{\mathbf{a}}_2 & \hat{\mathbf{a}}_3 \end{bmatrix}^T \tag{2.1}$$

All the vector quantities that will be discussed in this study will be expressed according to one of the following reference systems.

2.2.1 Earth Centered Inertial (ECI)

The Earth-Centered Inertial (ECI) reference frame is a quasi-inertial reference system. The unit vectors used to define this reference frame are the following:

- $\hat{\mathbf{e}}_1$, which points toward the Vernal Equinox;
- $\hat{\mathbf{e}}_3$, which points toward the celestial North Pole;
- $\hat{\mathbf{e}}_2$, which lies on the equatorial plane, completes the right-handed triad and is defined as $\hat{\mathbf{e}}_2 = \hat{\mathbf{e}}_3 \times \hat{\mathbf{e}}_1$.

$$\hat{\mathcal{F}}_{ECI} \triangleq \begin{bmatrix} \hat{\mathbf{e}}_1 & \hat{\mathbf{e}}_2 & \hat{\mathbf{e}}_3 \end{bmatrix}^T \tag{2.2}$$

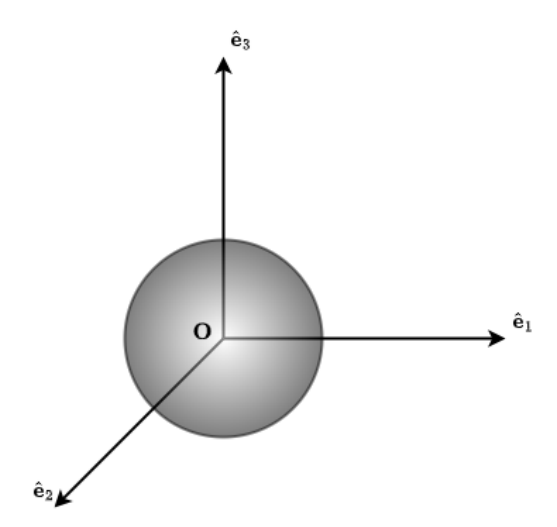


Figure 2.1: ECI reference frame

It is note worthy to remember that, since this geocentric system is attached to the Earth, it is subject to continuous acceleration and, therefore, theoretically cannot be considered as a proper inertial reference frame. In fact, the Earth orbits the Sun on its almost circular orbit and in turn the Sun orbits the center of the Milky Way along an approximately circular path. However, since the accelerations are relatively small, in this study, as an acceptable approximation, \mathcal{F}_{ECI} is assumed to be fixed with respect to the distant stars. Therefore, it is considered acceptable to treat \mathcal{F}_{ECI} as an inertial frame.

It should be noted, finally, that the Earth is in rotation with respect to this reference frame.

2.2.2 Perifocal

This reference frame is the second Earth-centered reference frame that is taken into consideration in this study. Actually, by definition the Perifocal reference frame \mathcal{F}_P is centered on the focus of the analyzed orbit. This focus, however, exactly coincides with the Earth's center.

- $\hat{\mathbf{p}}_1$, points towards the perigee of the reference orbit;
- $\hat{\mathbf{p}}_3$, is normal to the orbital plane, parallel to the angular momentum vector, and inclined with respect to $\hat{\mathbf{e}}_3$ by an angle equal to the orbital inclination i;
- $\hat{\mathbf{p}}_2$, is advanced by 90 degrees in the direction of orbital motion and completes the right-handed triad.

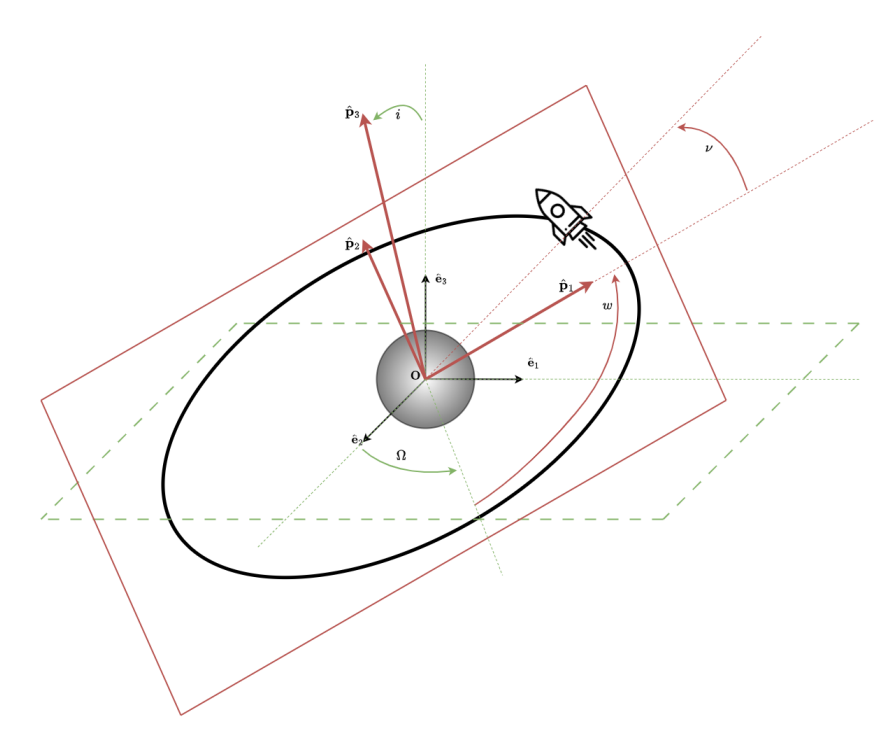


Figure 2.2: Perifocal reference frame

$$\hat{\mathcal{F}}_P \triangleq \begin{bmatrix} \hat{\mathbf{p}}_1 & \hat{\mathbf{p}}_2 & \hat{\mathbf{p}}_3 \end{bmatrix}^T \tag{2.3}$$

Given the initial Orbital Coordinates - orbit inclination i, eccentricity e, semimajor axis a, Right Ascension of the Ascending Node Ω (RAAN), argument of perigee ω , true anomaly ν - this reference frame provides a more straightforward mean of computing the initial state vector of the system's Center of Mass (CoM) - position and velocity at instant zero - enabling a generalizable and easily scalable analysis with respect to varying orbital conditions.

2.2.3 Local Vertical - Local Horizontal (L)

This is a non-inertial Cartesian Coordinate System (CCS). Specifically, it is an Orbital Reference Frame centered and oriented according to the instantaneous position - with respect to the Earth - of the center of mass of the system under consideration, which, in our case, is the Tethered Satellite System. This reference frame proves particularly useful, as Earth-Centered Inertial (ECI) frames are well suited for modeling orbital dynamics, but they are not equally effective when it comes to describing the relative motion between satellites, which constitutes the primary focus of our study.

It is defined as follows:

- $\hat{\boldsymbol{\ell}}_1 = \frac{\mathbf{R}}{\|\mathbf{R}\|}$, is pointed toward the instantaneous radial direction;
- $\hat{\ell}_3 = \frac{\mathbf{R} \times \dot{\mathbf{R}}}{\|\mathbf{R} \times \dot{\mathbf{R}}\|}$, perpendicular to the orbital plane and coincident with the direction of the system's angular momentum. This direction will be referred to as the cross-track direction;
- $\hat{\ell}_2$ completes the right-handed triad as $\hat{\ell}_2 = \hat{\ell}_3 \times \hat{\ell}_1$. This will be referred to as the along-track direction.

$$\hat{\mathcal{F}}_L \triangleq \begin{bmatrix} \hat{\boldsymbol{\ell}}_1 & \hat{\boldsymbol{\ell}}_2 & \hat{\boldsymbol{\ell}}_3 \end{bmatrix}^T \tag{2.4}$$

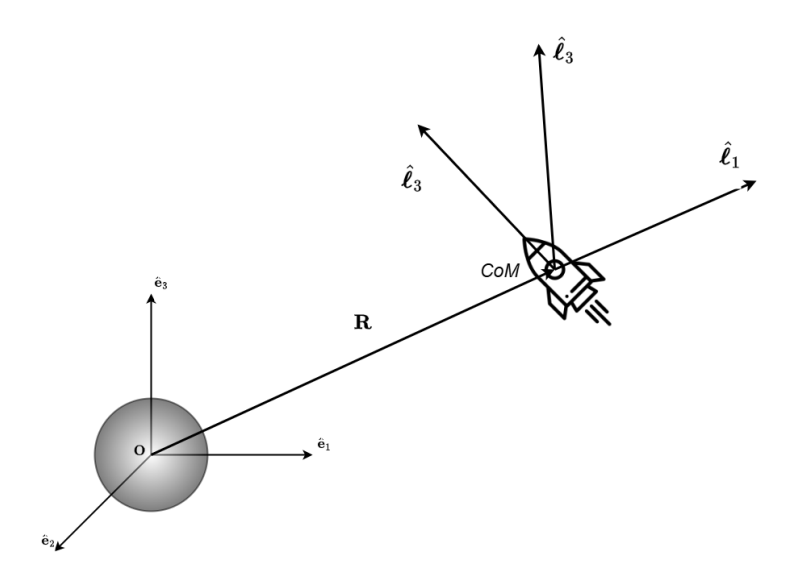


Figure 2.3: Local Orbital Reference Frame

This is the reference frame that will be adopted to analyze and represent the relative motion between the elements of the model used to represent the Tethered Satellite System.

Once the reference frames have been introduced, it is now possible to complete the overview of vector notation and their representation. To this end, let us consider a generic vector \mathbf{v} . The expression of this vector within the ECI reference frame is the following:

$$\mathbf{v}^{ECI} = v_x^{ECI}\hat{\mathbf{e}}_1 + v_y^{ECI}\hat{\mathbf{e}}_2 + v_z^{ECI}\hat{\mathbf{e}}_3$$
 (2.5)

where v_x^{ECI} , v_y^{ECI} and v_z^{ECI} are the components of **v** along the unit vectors $\hat{\mathbf{e}}_1$, $\hat{\mathbf{e}}_2$, and $\hat{\mathbf{e}}_3$.

$$\mathbf{v}^{ECI} = \begin{bmatrix} v_1 & v_2 & v_3 \end{bmatrix}^T \tag{2.6}$$

Recalling the vectrix formulation of the ECI reference frame provided in Equation 2.1, it is possible to write the vector \mathbf{v} alternatively as:

$$\mathbf{v}^{ECI} = \hat{\mathcal{F}}_{ECI}^T \mathbf{v} \tag{2.7}$$

The same vector can be conceptually represented in an analogous manner within the other two reference frames. For instance, the expression of the vector \mathbf{v} in the Local Vertical - Local Horizontal reference frame \mathcal{F}_L is the following:

$$\mathbf{v}^L = v_x^L \hat{\boldsymbol{\ell}}_1 + v_y^L \hat{\boldsymbol{\ell}}_2 + v_z^L \hat{\boldsymbol{\ell}}_3 \tag{2.8}$$

The physical quantity represented by the vector remains the same across all reference frames. However, the vector representations differ depending on the CCS in which they are expressed. The most intuitive difference arises from the relative distance with respect to the origin of the chosen reference frame. An equally important distinction, nevertheless, lies in the rotational relationship between these reference frames. In the following section, we will examine how to perform transformations between each of these reference systems.

2.3 Rotation Matrices

Rotation matrices represent a fundamental tool for transforming vector quantities between different reference frames. In many applications, physical quantities are more easily observed or computed within a specific reference frame; however, for operational purposes and to ensure consistency across analyses, it is often necessary to express them with respect to another CCS. This necessity makes the use of appropriate rotation matrices essential to correctly transform variables between frames

Let us consider a generic reference frame \mathcal{F}_A , represented by the vectrix notation:

$$\hat{\mathcal{F}}_A = \begin{bmatrix} \hat{\mathbf{a}}_1 & \hat{\mathbf{a}}_2 & \hat{\mathbf{a}}_3 \end{bmatrix} \tag{2.9}$$

We can observe the following fundamental properties that arise from the orthonormality of its basis vectors:

$$\hat{\mathcal{F}}_A \cdot \hat{\mathcal{F}}_A^T = \begin{bmatrix} \hat{a}_1 \cdot \hat{a}_1 & \hat{a}_1 \cdot \hat{a}_2 & \hat{a}_1 \cdot \hat{a}_3 \\ \hat{a}_2 \cdot \hat{a}_1 & \hat{a}_2 \cdot \hat{a}_2 & \hat{a}_2 \cdot \hat{a}_3 \\ \hat{a}_3 \cdot \hat{a}_1 & \hat{a}_3 \cdot \hat{a}_2 & \hat{a}_3 \cdot \hat{a}_3 \end{bmatrix} = \begin{bmatrix} 1 & 0 & 0 \\ 0 & 1 & 0 \\ 0 & 0 & 1 \end{bmatrix} = \mathbf{I}_3$$
 (2.10)

$$\hat{\mathcal{F}}_A \times \hat{\mathcal{F}}_A^T = \begin{bmatrix} \hat{a}_1 \times \hat{a}_1 & \hat{a}_1 \times \hat{a}_2 & \hat{a}_1 \times \hat{a}_3 \\ \hat{a}_2 \times \hat{a}_1 & \hat{a}_2 \times \hat{a}_2 & \hat{a}_2 \times \hat{a}_3 \\ \hat{a}_3 \times \hat{a}_1 & \hat{a}_3 \times \hat{a}_2 & \hat{a}_3 \times \hat{a}_3 \end{bmatrix} = \begin{bmatrix} 0 & \hat{a}_3 & -\hat{a}_2 \\ -\hat{a}_3 & 0 & \hat{a}_1 \\ \hat{a}_2 & -\hat{a}_1 & 0 \end{bmatrix}$$
(2.11)

Specifically, the dot product of the vectrix with its transpose yields the identity matrix, reflecting both the orthogonality and the unit norm of the basis vectors. Similarly, the structure of the cross product reveals the intrinsic right-handedness of the frame.

Let us now consider once again the generic vector \mathbf{v} , whose expression in the generic reference frame \mathcal{F}_A can be can be written according to the equation 2.5:

$$\mathbf{v}^A = \hat{\mathcal{F}}_A \cdot \mathbf{v} \tag{2.12}$$

Considering the expression of the same vector in a second, generic reference frame \mathcal{F}_B and recalling the equations 2.5 and 2.12:

$$\mathbf{v}^B = \hat{\mathcal{F}}_B \cdot \mathbf{v} = \hat{\mathcal{F}}_B \cdot \hat{\mathcal{F}}_A^T \cdot \mathbf{v}^A \tag{2.13}$$

This final expression, reveals how the vector \mathbf{v} expressed in the reference frame \mathcal{F}_B is nothing more than the same vector expressed in frame \mathcal{F}_A , pre-multiplied by a rotation matrix, which we can identify as:

$$\mathbf{R}_{ba} = \hat{\mathcal{F}}_B \cdot \hat{\mathcal{F}}_A^T \tag{2.14}$$

This notation refers to the rotation matrix which, when pre-multiplied to a vector expressed in reference frame \mathcal{F}_A , yields the same vector expressed in \mathcal{F}_B . It is both intuitive and demonstrable that the inverse transformation - the conversion from \mathbf{v}^B back to \mathbf{v}^A - can be performed using the rotation matrix:

$$\mathbf{R}_{ab} = \hat{\mathcal{F}}_A \cdot \hat{\mathcal{F}}_B^T \tag{2.15}$$

By elaborating the equations 2.14 and 2.15 the following property, concerning the relationship between a rotation matrix and the matrix that performs the inverse rotation, is obtained:

$$\mathbf{R}_{ab} = \mathbf{R}_{ba}^{-1} \tag{2.16}$$

and, given the orthonormality of the basis vectors:

$$\mathbf{R}_{ba}^{T} = \mathbf{R}_{ba}^{-1} \quad \Rightarrow \quad \mathbf{R}_{ab} = \mathbf{R}_{ba}^{T} \tag{2.17}$$

Chapter 3

Mathematical Model

This chapter is intended to present the reference mathematical model developed to analyze the dynamics of the Tethered Satellite System. It has been structured to progressively introduce the various ingredients required to define the characteristic equations of motion of the system - starting from the external disturbances and forces, moving on to the internal forces and tether modeling, and finally addressing deployment-related issues. This step-by-step approach ultimately leads to full formulation of the equations by distinguishing between two main modeling approaches: the discrete model, in which the tether is represented as a chain of interconnected elements, and the dumbbell model. Throughout the chapter, the reader is also guided through the procedure that enables the tether to be represented using either approach.

3.1 Rotating Reference Frame

In the previous chapter reference frames have been introduced, however the behavior of the reference frames themselves has not been explicitly taken into account. This aspect becomes crucial, especially when dealing with non-inertial reference frames. In particular, special attention must be paid to the relative rotation between the reference frames. For example, in our analysis the Local reference frame \mathcal{F}_L rotates with respect to the Earth-centered CCS \mathcal{F}_{ECI} . Such rotation gives rise to additional terms in both the first and second time derivatives of vector quantities and we should not neglect this effect in order to formulate the kinematic and dynamic equations correctly and consistently.

Let us call in action the two generic reference frames used in the previous chapter, \mathcal{F}_A and \mathcal{F}_B , together with the generic vector \mathbf{v} . We assume now that \mathcal{F}_B is rotating with angular velocity $\boldsymbol{\omega}_{ba}$ relative to \mathcal{F}_A : For the sake of simplicity and clarity for the reader, the following is specified:

- The notation \mathbf{v}^A , refers to the vector \mathbf{v} expressed in \mathcal{F}_A ;
- The notation \mathbf{v}^B , refers to the vector \mathbf{v} expressed in \mathcal{F}_B ;

Assuming now that the vector \mathbf{v} represents the position of a material point P.

- The notation \mathbf{v}_a , refers to the position of P with respect to the origin of \mathcal{F}_A ;
- The notation \mathbf{v}_b , refers to the position of P with respect to the origin of \mathcal{F}_B ;
- The notation $\dot{\mathbf{v}}_a^A$, refers to the velocity of P with respect to the origin of \mathcal{F}_A expressed in the reference frame \mathcal{F}_A ;
- The notation $\dot{\mathbf{v}}_a^B$, refers to the velocity of P with respect to the origin of \mathcal{F}_A expressed in the reference frame \mathcal{F}_B ;

The same considerations apply to the velocity of P with respect to the origin of \mathcal{F}_B , $\dot{\mathbf{v}}_b$, and later to the accelerations. The relationship between $\dot{\mathbf{v}}_a$ and $\dot{\mathbf{v}}_b$ is given by:

$$\dot{\mathbf{v}}_a = \dot{\mathbf{v}}_b + \boldsymbol{\omega}_{ba} \times \mathbf{v}_b \tag{3.1}$$

By further deriving the equation 3.1, we obtain the expression of the second time derivative:

$$\ddot{\mathbf{v}}_a = \ddot{\mathbf{v}}_b + \dot{\boldsymbol{\omega}}_{ba} \times \mathbf{v}_b + \boldsymbol{\omega}_{ba} \times \boldsymbol{\omega}_{ba} \times \mathbf{v}_b + 2\boldsymbol{\omega}_{ba} \times \dot{\mathbf{v}}_b \tag{3.2}$$

In the last expression, the following inertial terms appear:

- The centrifugal acceleration: $2\omega_{ba} \times \dot{\mathbf{v}}_b$;
- The Coriolis acceleration: $\boldsymbol{\omega}_{ba} \times \boldsymbol{\omega}_{ba} \times \mathbf{v}_{b}$;
- The Euler acceleration: $\dot{\omega}_{ba} \times \mathbf{v}_{b}$.

The expressions of these derivatives, which highlight the significance of the effect of the rotating frame, can be conveniently represented either in the coordinates of one reference frame or in those of the other.

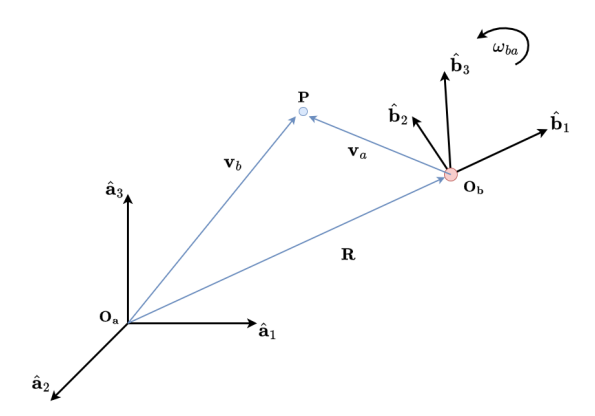


Figure 3.1: Rotating reference frames

3.2 Modeling of the external forces

One of the intrinsic challenges of space missions arises from the fact that, once the launch countdown is completed and the orbital insertion phase of the spacecraft begins, human intervention and the ability to actively respond to potential maneuvering needs, trajectory deviations, or system malfunctions become virtually nonexistent - unless such scenarios have been accurately anticipated and studied. In essence, improvisation and emergency interventions are not viable options in space operations. Therefore, it becomes immediately evident how crucial it is to conduct a thorough analysis of the operational environment of the mission and of all the factors that may perturb the spacecraft's motion during its operational phase. Among the perturbative effects that must be accounted for in a space mission - beyond the dominant gravitational attraction of the central body - are aerodynamic drag, perturbation of the gravitational potential field, solar radiation pressure, and third-body gravitational effects.

In this work, based on the chosen altitude and mission application, only the gravitational field perturbations and aerodynamic drag will be considered as disturbances affecting the system dynamics. The effects of solar radiation pressure and third-body interactions - specifically with the Moon - will be neglected. The following subsections will introduce the mathematical formulation of these perturbations, along with the parameters required for their evaluation.

The notation with the 'ECI' superscript - \mathbf{v}^{ECI} - will be omitted in these subsections; however, unless otherwise specified, all quantities presented herein are intended to be defined with respect to the \mathcal{F}_{ECI} reference frame.

3.2.1 Earth's Gravitational Potential Perturbation

The first perturbation considered is that of the terrestrial gravitational potential. As a starting point, we present the formulation commonly used when evaluating the acceleration exerted by a massive body on an orbiting object:

$$\mathbf{a}_G = -\frac{GM_{\oplus}}{\|\mathbf{R}\|^3} \mathbf{R} \tag{3.3}$$

here, G denotes the gravitational constant, M_{\oplus} represents the mass of the Earth, and \mathbf{R} is the position vector from the Earth's center to the center of mass of the body under consideration. In this case, the acceleration due to the earth's gravitational field is modeled by the gravitational force of a point mass positioned at the center of the earth. However, this formulation is based on the simplifying assumption that the attracting body - in this case, the Earth - is perfectly spherical and has a uniform mass distribution. In reality, the Earth is neither spherical nor homogeneous, and therefore the expression previously introduced in 3.3 does not represent the most accurate model. For higher fidelity, especially when analyzing the motion of bodies in proximity to Earth, it becomes necessary to rely on more sophisticated models able to account for the gravitational contribution of each infinitesimal volume element dv, depending on its position and density, according to the following equation:

$$\mathbf{a}_G = -G \int \frac{\rho(\mathbf{r})}{\|\mathbf{R}\|^3} \,\mathbf{R} dv \tag{3.4}$$

where dv is infinitesimal volume element located at position \mathbf{r} , and $\rho(\mathbf{r})$ represents the density of the Earth in the infinitesimal volume element dv.

This work adopts as reference the expression of the gravitational potential formulated using the spherical harmonic analysis and Legendre function [42], [43], [44].

$$V(R,\phi,\lambda) = \frac{GM_{\oplus}}{R} \sum_{n=0}^{\infty} \sum_{m=0}^{n} \left(\frac{R_{\oplus}}{R}\right)^{n} P_{nm}(\sin\phi) \left[C_{nm}\cos(m\lambda) + S_{nm}\sin(m\lambda)\right]$$
(3.5)

 R_{\oplus} indicates the earth radius, R is norm of the position vector from the Earth's center to the center of mass of the body under consideration, ϕ is the latitude, and λ the longitude.

Specifically, depending on the desired level of precision, one may choose appropriate values of degree n and order m, and consequently compute the function P_{nm} and the spherical harmonics C_{nm} and S_{nm} . The general expressions for the Legendre function P_{nm} is given as follows:

$$P_{nm}(u) = \frac{1}{2^n n!} (1 - t^2)^{m/2} \frac{d^{(n+m)}}{du^{(n+m)}} (u^2 - 1)^n$$
(3.6)

where u is a simple substitution: $u = \sin \phi$.

Spherical harmonics refers to the following set of expressions:

$$C_{nm} = (2 - \delta) \frac{M_{\oplus}}{R_{\oplus}^n} \frac{(n - m)!}{(n + m)!} \int \rho(r) \, r^n \, P_{nm}(\sin \phi') \cos(m\lambda') \, dr$$
 (3.7)

$$S_{nm} = (2 - \delta) \frac{M_{\oplus}}{R_{\oplus}^n} \frac{(n - m)!}{(n + m)!} \int \rho(r) \, r^n \, P_{nm}(\sin \phi') \sin(m\lambda') \, dr \tag{3.8}$$

here \mathbf{r} is again the position of the infinitesimal volume element, and $\rho(\mathbf{r})$ represents its the density. Finally, δ is defined as follows:

$$\delta = \begin{cases} 1, & m = 0 \\ 0, & m \neq 0 \end{cases} \tag{3.9}$$

Particular attention will be given to the J_2 effect, associated with the zonal harmonic coefficient C_{20} and accounts for the oblateness of the Earth. Among the higher-order perturbative components of the gravitational potential, the J_2 term represents the most significant deviation from the ideal spherical model.

Let us now present the derivation of the polynomial and the subsequent transition from the gravitational potential expression to the corresponding gravity acceleration, expressed in the form that will be employed in our code. The contribution of the J_2 term corresponds to the spherical harmonic component of degree n=2 and order m=0. Legendre functions of degree (m=0), represent a special case and are commonly referred to as Legendre polynomials with the following simplified form:

$$P_n(u) = \frac{1}{2^n n!} \frac{d^n}{du^n} (u^2 - 1)^n \tag{3.10}$$

Specifying the expression in the case of n=2:

$$P_{n=2}(u) = \frac{1}{2} \left(3u^2 - 1 \right) \tag{3.11}$$

For the sake of completeness, it is worth noting that, conventionally, for n = 0: $P_0 = 1$ and $C_{00} = 1$; while for n = 1: $P_1 = u$ and $C_{10} = 0$.

According to equations 3.5 - 3.11, we thus have the following expression for the gravitational potential of the Earth:

$$V(r,\phi,\lambda) = -\frac{\mu_{\oplus}}{R} \left[1 - J_2 \left(\frac{R_{\oplus}}{R} \right)^2 \frac{1}{2} \left(3\sin^2 \phi - 1 \right) \right]$$
 (3.12)

Finally, it is possible to obtain the perturbative acceleration, by computing the gradient of the potential:

$$\mathbf{a}_G = \nabla V \tag{3.13}$$

the final expression is:

$$\boldsymbol{a}_g = -\frac{\mu_{\oplus}}{\|\boldsymbol{R}\|^3} \boldsymbol{R} + J_{2factor} \frac{\mu_{\oplus}}{\|\boldsymbol{R}\|^3} \boldsymbol{R}$$
(3.14)

where μ_{\oplus} is defined as $\mu_{\oplus} = GM_{\oplus}$. All the variable here are to be considered measured and expressed in the \mathcal{F}_{ECI} reference frame. The term $J_{2factor}$ is as follows:

$$J_{2factor} = \frac{3}{2} J_2 \left(\frac{R_{\oplus}}{\|\mathbf{R}\|} \right)^2 \begin{bmatrix} 5 \left(\frac{R_z}{\|\mathbf{R}\|} \right)^2 - 1 & 0 & 0 \\ 0 & 5 \left(\frac{R_z}{\|\mathbf{R}\|} \right)^2 - 1 & 0 \\ 0 & 0 & 5 \left(\frac{R_z}{\|\mathbf{R}\|} \right)^2 - 3 \end{bmatrix}$$
(3.15)

3.2.2 Aerodynamic drag

We now turn to the second perturbation considered in this work. Although the spacecraft operates beyond the boundaries of the Earth's atmosphere, it still encounters a residual presence of atmospheric particles, especially in low Earth orbits. Aerodynamic drag thus becomes the most prominent perturbative effect acting on satellites in such orbits. This is primarily due to the combination of the high orbital velocities with a low, but still non-negligible, atmospheric density.

To balance physical realism and computational efficiency, a simplified model is adopted in our simulations to approximate these effects without excessive numerical cost. Therefore, the expression used to compute the acceleration associated with this perturbation is the following:

$$\mathbf{a}_D = -\frac{1}{2} \frac{\rho_{\text{atm}} C_d A}{m} v_r^2 \hat{\mathbf{v}}_r \tag{3.16}$$

where ρ_{atm} is the atmospheric density - evaluated according to the Harris-Priester model [43] - C_d is the drag coefficient, A is the reference cross-sectional area of the satellite, m is the satellite mass, and v_r is the relative velocity between the satellite and the surrounding atmosphere. The combination of the orders of magnitude of the atmospheric density and the orbital velocity results in a residual acceleration that is not negligible. This acceleration corresponds to a force acting

in the direction opposite to the motion of the spacecraft. Its primary effects include a gradual decrease in the semi-major axis and a progressive circularization of the orbit.

It is important to note that the velocity appearing in the drag expression refers to the relative velocity. This quantity represents the velocity of the spacecraft with respect to the atmospheric particles impacting its surface. Its expression is given by:

$$\mathbf{v}_r = \mathbf{v} - \mathbf{v}_{\text{atm}} \tag{3.17}$$

Indeed, it must be taken into account that the atmospheric particles are not stationary at the moment of impact; rather, they are rotating along with the Earth, with a velocity equal to the Earth's rotational velocity. We have that:

$$\mathbf{v}_{\text{atm}} = \boldsymbol{\omega}_{\oplus} \times \mathbf{R} \tag{3.18}$$

where ω_{\oplus} is the earth's angular velocity and **R** is the position vector from the Earth's center to the center of mass of the body under consideration.

3.3 Modeling of the internal forces

In order to enable a complete and accurate analysis, especially in systems such as a TSS, it is fundamental not only to consider the effects of the external factors, but also to account for the internal forces.

First and foremost, in almost all space systems it is necessary to implement control forces to ensure the maintenance of the desired position and attitude. These control forces are classified as internal forces, since they are generated by actuation mechanisms that are integral part of the system, such as thrusters and reaction wheels. In addition to these forces, tether tension plays a fundamental role in TSSs and significantly influences the system dynamics.

Section 1.4.1 provided an overview on the different modeling approaches used to analyze a TSS and, as previously mentioned, the choice of one model over another directly affects the ability to accurately capture the internal dynamics of the system. In this thesis, two models were employed for different purposes. The study and understanding of the system's dynamics has been entrusted to the discrete model. Subsequently, regarding the study of deployment strategies, an initial analysis was carried out using the dumbbell model. This choice was motivated by its simplicity and allowed for a faster and less computationally demanding assessment of the necessary control action; these were subsequently transferred to the discrete model by extracting and applying the corresponding control accelerations. Consequently, in this section both tether models will be introduced.

3.3.1 Tether discrete model

Among the presented alternatives, the lumped-masses model turns out to be the best compromise between accuracy and computational efficiency. Accordingly, the choice of reference for interpreting the system's dynamics falls on this model. In this section we address the construction process of the model and the representation of the tether, thereby laying the groundwork for formulating the system's dynamic equations. This study is built upon to the discretization process proposed by Quadrelli [45], [46]. Let us consider the following reference representation for the system under analysis:



Figure 3.2: Modeling scheme of the tethered satellite system

Delving into details, let us start by specifying that, for the sake of simplicity, the two satellites at the ends of the tether are modeled as point masses concentrated at the extremities, but for simplicity of visualization they are represented as squares. In relation to Figure 3.2, we now introduce the generalized coordinate s. Below, a representation of a general case is provided. Indeed, the subdivision approach proposed by Quadrelli is particularly well-suited for describing general system configurations, including the deployment process, and will prove especially useful later in the analysis.



Figure 3.3: Schematic representation at a generic instant during the deployment process

It is important to precise that, as will be discussed later, the system is designed to be launched in a compact configuration with the tether initially reeled - half within one satellite and half within the other. In this context, Figure 3.3 becomes easier to interpret. The coordinate s is simply a material coordinate used to identify the different portions of the tether. Specifically:

- the part of tether reeled in spacecraft A at instant t is identified by :

$$0 \le s \le s_A(t) \tag{3.19}$$

- the portion of tether reeled in spacecraft B at instant t is identified by :

$$s_B(t) \le s \le L_{tot} \tag{3.20}$$

 L_{tot} is here the total tether length.

- while the part of tether deployed at instant t, $\bar{\ell}(t)$, is identified by:

$$s_A(t) \le s \le s_B(t) \tag{3.21}$$

Let us now consider the case in which the tether is fully deployed, which will also serve as the initial reference case for analyzing and discussing the system's dynamics. In this case the reference values are: $s_A = 0$, $s_B = L_{\rm tot}$ and $\bar{\ell} = L_{\rm tot}$.



Figure 3.4: Schematic representation of the fully deployed system

For the purposes of our analysis, we adopt a reference discretization of the tether into 10 lumped masses. Let us now outline, step by step, the procedure through which the continuous tether is reduced to a set of N point masses - 10 in our case connected by spring-damper elements. First, the tether is divided into N segments by defining a series of nodes that divide it into equal parts. At the center of mass of each segment, a point mass is placed, corresponding in value to the mass of that segment. Each point mass thus represents a portion of the tether. As a result, the system consists of N lumped masses standing for the tether itself, in addition to the two satellite masses located at the ends.

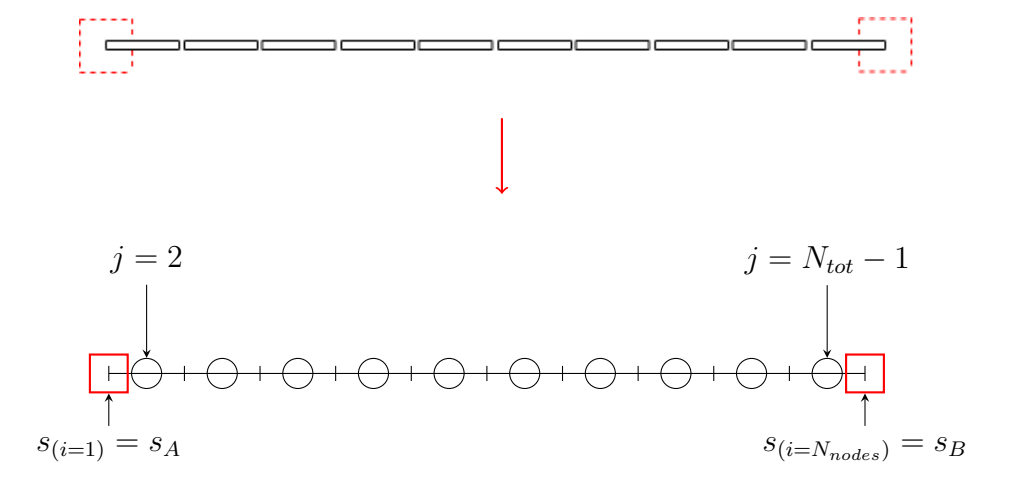


Figure 3.5: Modeling and discretization process

Furthermore, Let us now specify for the sake of clarity the following notation:

- N_{int} indicates the number of the internal lumped masses representing the tether. $N_{int} = 10$ in our reference case. It should be remembered that the number of lumped masses corresponds to the number of segments N into which the tether has been divided.
- $N_{nodes} = N_{int} + 1$ refers to the number of nodes used in the discretization process. In our reference case $N_{nodes} = 11$.
- $N_{tot} = N_{int} + 2$ is the total number of masses included in the system model. $N_{tot} = 12$ in our reference case.
- $N_{threads}$ is used for the sake of clarity and simplicity to identify the number spring-damper connective elements.

Before proceeding with the computation of the tension, let us take a further step into the details of the adopted model. First of all, from this point onward, the symbol ρ_j will be used to denote the position vector of each of the just defined masses with respect to the origin of the local orbital reference frame.

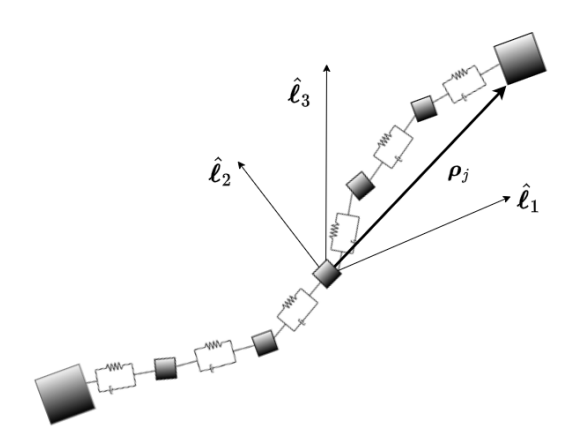


Figure 3.6: TSS discretized model

Secondly, in order to formulate the equations for the deployment scenario, which will be addressed later in Section 3.4.1, it is useful, within the current discretization, to identify the subdivision nodes along the tether. These nodes correspond to the endpoints of the N segments, and will be indexed using the notation i. In association with this indexing, we define a dimensionless coordinate ranging from 0 to 1:

$$\xi_i = \frac{i-1}{N_{nodes} - 1}$$
 $i = 1, 2, ..., N_{nodes}$ (3.22)

Based on this definition, the coordinate s for each node can be written as follows:

$$s_i = s_A + \xi_i \bar{l}(t) \tag{3.23}$$

Moreover, it is now possible to identify each segment as the collection of infinitesimal tether elements corresponding to the portion of the material coordinate s between two adjacent nodes, s_i and s_{i+1} . Consequently, the j-th point mass associated with that segment can be expressed as:

$$m_i = \mu_t \Delta s_i = \mu_t (s_{i+1} - s_i)$$
 (3.24)

where a relationship between index j and index i can be identified, given by the following expression: i = j - 1 for $j = 2, 3, ..., N_{tot}$. In this formula, μ_t refers to the linear density of the tether.

To account for the effects of internal forces, we finally introduce the use of spring-damper systems as connections between the lumped masses. Each mass is, in fact, connected to its adjacent ones through a spring-damper system.

Here the index k is used to identify each thread. The force developed within each k-th spring-damper element can be formulated as follows:

$$T_k = \begin{cases} K \left(\epsilon_k + c \dot{\epsilon}_k \right) \hat{\tau}_k & \epsilon_k > 0 \& \dot{\epsilon}_k > 0 \\ 0 & \epsilon_k \le 0 \end{cases}$$
 (3.25)

where K = EA, with E Young's modulus and A reference cross-sectional area, while c is a proportionality coefficient such that cK represents the damping coefficient. Finally, $\hat{\tau}_k$ is the unit vector identifying the direction of the tension. In addition to material and geometric properties, the strain, the strain rate, and the orientation of each thread needs to be defined. To obtain the latter quantities, the following parameters must be considered:

- The undeformed length of the thread:

$$\bar{l}_{k} = \begin{cases} \frac{1}{2} \frac{L_{tot}}{N} & \text{for the external threads (} k = 1, N_{threads}) \\ \\ \frac{L_{tot}}{N} & \text{for all the internal threads (} k = 2, ..., N_{threads} - 1) \end{cases}$$
(3.26)

- The orientation of the thread, given as:

$$\hat{\boldsymbol{\tau}}_k = \frac{(\boldsymbol{\rho}_{k+1} - \boldsymbol{\rho}_k)}{\|\boldsymbol{\rho}_{k+1} - \boldsymbol{\rho}_k\|} \qquad k = 1, 2, ..., N_{threads}$$
(3.27)

- The mechanical stretch l_m :

$$l_{m,k} = \|\boldsymbol{\rho}_{k+1} - \boldsymbol{\rho}_k\| - \bar{l}_k \qquad k = 1, 2, ..., N_{threads}$$
 (3.28)

- The mechanical stretch rate \dot{l}_m , defined as:

$$\dot{l}_{m,k} = (\dot{\boldsymbol{\rho}}_{k+1} - \dot{\boldsymbol{\rho}}_k) \cdot \hat{\boldsymbol{\tau}}_k \qquad k = 1, 2, ..., N_{threads}$$
(3.29)

Once this values have been computed it is possible to obtain the strain and the strain rate, respectively, as:

$$\varepsilon_k = \frac{l_{m,k}}{\bar{l}_k} \tag{3.30}$$

$$\dot{\varepsilon}_k = \frac{\bar{l}_k \, \dot{l}_{m,k} - \dot{\bar{l}}_k \, l_{m,k}}{\bar{l}_k^2} \tag{3.31}$$

Given the tension in each thread it is important to note that each mass element experiences the tension force exerted by the spring-damper element on its right and the tension force exerted by the spring-damper element on its left; except for the masses at the two ends of the tether, which are subjected to only one tension force.

Finally, it is important to emphasize that this formulation deliberately neglects the compressive capacity of the tether system. Specifically, it is assumed that the force developed along any segment of the tether instantaneously drops to zero as soon as a negative strain is detected, i.e., as soon as the segment undergoes compression. From a physical perspective, this implies that the tether is assumed to undergo immediate buckling as soon as it experiences a compressive load. This assumption is consistent with the actual behavior of cables, which exhibit tensile forces only when stretched and shows no resistance under compression.

3.3.2 Tether dumbbell model

Having access to a fast and low-cost alternative is a significant advantage that should not be overlooked, particularly in the early stages of analysis or when testing control strategies. With this in mind, and considering the computational burden associated with the lumped-masses approach once the deployment phase is introduced, this section introduces the rod modeling of the Tethered Satellite System. The difference compared to the previous case is substantial and immediately evident: the system is now reduced - regardless of the tether's flexibility and elasticity - to two point masses connected by a rod of infinite stiffness, which neither bends nor twists.

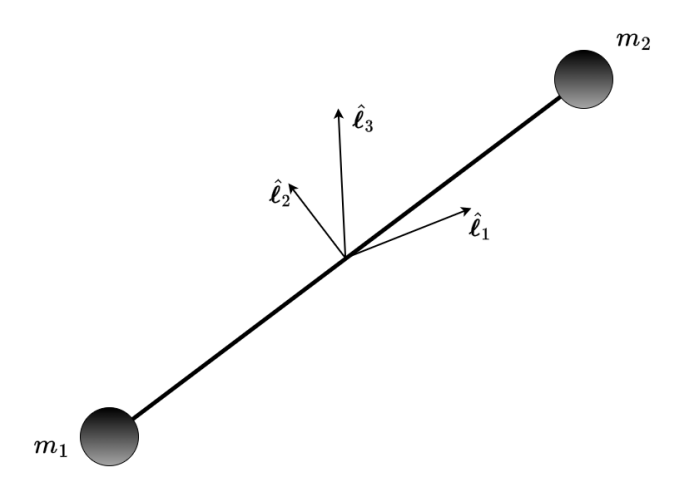


Figure 3.7: TSS rod model

The reduction in complexity becomes clearly apparent also at the level of the equations of motion, as will be shown later. In this formulation, the number of degrees of freedom is drastically reduced when compared to the discrete model: in

fact, only three coordinates are required to fully describe the state of the system. Therefore, despite this simplification clearly reduces the level of detail captured, it provides a useful framework for preliminary studies, enabling rapid development and testing of deployment strategies and control laws without the computational burden associated with lumped masses model. In this way, the rod model serves as a practical compromise, offering insights into the overall system behavior while maintaining an acceptable level of consistency with the actual mission scenario.

3.3.3 Control forces

To conclude this section, we introduce the concept of control forces. In order to guide the system from the packed configuration to a desired operational configuration, to enable transitions between different configurations, or to ensure that the system remains stable once a target configuration is achieved, it is necessary to provide the system with actuators. In particular, thrusters and reaction wheels are the subsystems used to act on both the position and attitude dynamics, and the forces or torques exerted by these actuators must be properly modeled.

As a first step, the analysis will focus exclusively on the control of the system's position. For this reason, reaction wheels and relative torques will not be considered at this stage.

3.4 Equations of motion for the discrete model

Having addressed all the necessary components - ranging from the basic elements of the mathematical model to the formulation of internal forces - it is now time to undertake a deeper investigation of the equations of motion implemented in our code. The equations of motion are formulated in the \mathcal{F}_{ECI} reference frame, given that many of the relevant quantities are defined in this CCS. However the results illustrating the system's dynamics will be later presented with respect to the local orbital frame \mathcal{F}_L ; thus, special attention must be paid to the transformations between the two main reference frames.

Let us now take into consideration the expression of the position vector of the j-th mass of the system, ρ_i .

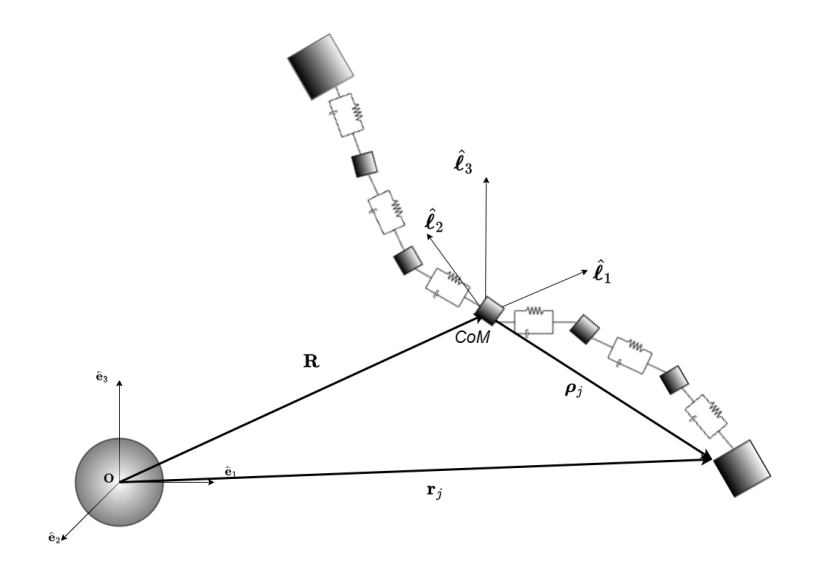


Figure 3.8: Main elements of the mathematical model

According to the representation given in Figure 3.8 and to the notation previously explored:

$$\mathbf{r}_j = \mathbf{R} + \boldsymbol{\rho}_j \quad \rightarrow \quad \boldsymbol{\rho}_j = \mathbf{r}_j - \mathbf{R}$$
 (3.32)

To obtain the kinematic and dynamic equations, it is now sufficient to accurately differentiate the equation 3.32 in \mathcal{F}_{ECI} . By performing the first derivation:

$$\dot{\boldsymbol{\rho}}_{j,ECI} = \dot{\mathbf{r}}_{j,ECI} - \dot{\mathbf{R}}_{ECI} \tag{3.33}$$

By further deriving this equation, again in the ECI frame:

$$\ddot{\boldsymbol{\rho}}_{j,ECI} = \ddot{\mathbf{r}}_{j,ECI} - \ddot{\mathbf{R}}_{ECI} \tag{3.34}$$

Let us now take a step forward towards the final formulation. We need to integrate the equations representing the motion of the j-th mass with respect to the local reference frame \mathcal{F}_L . Remembering that \mathcal{F}_L rotates with respect to \mathcal{F}_{ECI} with an angular velocity Ω , we can express the time derivatives of ρ_j in the inertial reference frame - $\dot{\rho}_{j,ECI}$ and $\ddot{\rho}_{j,ECI}$ - as function of the time derivatives of the same vector in the non-inertial reference frame - denoted by $\dot{\rho}_{j,L}$ and $\ddot{\rho}_{j,L}$. To the equations 3.33 and 3.34 respectively correspond:

$$\dot{\boldsymbol{\rho}}_{j,ECI} = \dot{\boldsymbol{\rho}}_{j,L} + \Omega \times \boldsymbol{\rho}_j \tag{3.35}$$

$$\ddot{\boldsymbol{\rho}}_{i,ECI} = \ddot{\boldsymbol{\rho}}_{i,L} + \boldsymbol{\Omega} \times \boldsymbol{\Omega} \times \boldsymbol{\rho}_i + \dot{\boldsymbol{\Omega}} \times \boldsymbol{\rho}_i + 2\boldsymbol{\Omega} \times \dot{\boldsymbol{\rho}}_{i,L}$$
(3.36)

By simply inverting these equations we obtain:

$$\dot{\boldsymbol{\rho}}_{j,L} = \dot{\boldsymbol{\rho}}_{j,ECI} - \Omega \times \boldsymbol{\rho}_j \tag{3.37}$$

$$\ddot{\boldsymbol{\rho}}_{j,L} = \ddot{\boldsymbol{\rho}}_{j,ECI} - \Omega \times \Omega \times \boldsymbol{\rho}_j - \dot{\Omega} \times \boldsymbol{\rho}_j - 2\Omega \times \dot{\boldsymbol{\rho}}_{j,L}$$
(3.38)

And now, by substituting the expression in 3.34 into 3.38:

$$\ddot{\boldsymbol{\rho}}_{i,L} = (\ddot{\mathbf{r}}_i - \ddot{\mathbf{R}}) - \mathbf{\Omega} \times \mathbf{\Omega} \times \boldsymbol{\rho}_i - \dot{\mathbf{\Omega}} \times \boldsymbol{\rho}_i - 2\mathbf{\Omega} \times \dot{\boldsymbol{\rho}}_{i,L}$$
(3.39)

In order to ensure consistency in the analysis, all quantities must be expressed in the same reference frame, in our case \mathcal{F}_L :

$$\ddot{\boldsymbol{\rho}}_{j,L}^{L} = (\ddot{\mathbf{r}}_{j} - \ddot{\mathbf{R}})^{L} - \boldsymbol{\Omega}^{L} \times \boldsymbol{\Omega}^{L} \times \boldsymbol{\rho}_{j}^{L} - \dot{\boldsymbol{\Omega}}^{L} \times \boldsymbol{\rho}_{j}^{L} - 2\boldsymbol{\Omega}^{L} \times \dot{\boldsymbol{\rho}}_{j,L}^{L}$$
(3.40)

In certain cases, the variables are inherently defined and expressed in the \mathcal{F}_L reference frame. In contrast, other quantities - such as the angular velocity, angular acceleration, and the accelerations of the center of mass as well as of each j-th mass - are defined and evaluated in the \mathcal{F}_{ECI} reference frame. Thus, a transformation is needed, as expressed here:

$$(\ddot{\mathbf{r}}_j - \ddot{\mathbf{R}})^L = R_{L,ECI}(\ddot{\mathbf{r}}_j - \ddot{\mathbf{R}})^{ECI}$$
(3.41)

and analogously for all quantities defined in the \mathcal{F}_{ECI} reference frame. Here, $R_{L,ECI}$ refers to the rotation matrix which pre-multiplied by a quantity expressed in the \mathcal{F}_{ECI} frame, yields the same quantity expressed in the \mathcal{F}_L . It is defined as follows:

$$R_{L,ECI} = \hat{\mathcal{F}}_L \hat{\mathcal{F}}_{ECI}^T \tag{3.42}$$

The inverse transformation, as previously explored in Section 3.1, is easily performed by $R_{ECI,L} = R_{L,ECI}^T$.

At this stage, we still need to specify the accelerations of both the center of mass and each j-th mass in the ECI reference frame. In the simulations conducted in this work the Earth's gravity potential and aerodynamic drag perturbations have been considered together with the internal forces. We write the acceleration of the j-th mass as:

$$\ddot{\mathbf{r}}_i = \mathbf{a}_{G,i} + \mathbf{a}_{D,i} + \mathbf{T}_i + \mathbf{u}_i \tag{3.43}$$

Here, \mathbf{T}_j is the resultant force from the balance of tensions acting on the mass - corresponding to the adjacent threads.

Regarding the center of mass, the corresponding quantities in terms of drag and gravitational acceleration can also be consistently calculated - excluding tension forces, whose resultant can be shown to be zero. Alternatively, it is possible to resort to the definition of Center of Mass:

$$\ddot{\mathbf{R}} = \frac{1}{\sum_{j} m_{j}} \sum_{j} m_{j} \ddot{\mathbf{r}}_{j} \quad \rightarrow \quad j = 1, 2, ..., N_{tot}$$
(3.44)

Finally, by substituting in 3.40 the equation to be integrated in the code for each mass assumes the following form:

$$\ddot{\boldsymbol{\rho}}_{j,L}^{L} = (\mathbf{a}_{G,j} + \mathbf{a}_{D,j} - \ddot{\mathbf{R}})^{L} - \boldsymbol{\Omega}^{L} \times \boldsymbol{\Omega}^{L} \times \boldsymbol{\rho}_{j}^{L} - \dot{\boldsymbol{\Omega}}^{L} \times \boldsymbol{\rho}_{j}^{L} - 2\boldsymbol{\Omega}^{L} \times \dot{\boldsymbol{\rho}}_{j,L}^{L} + \frac{\mathbf{T}_{j}}{m_{j}} + \mathbf{u}_{j} \quad (3.45)$$

The superscripts L have been added in this final form to specify that the equation is written in the local reference frame \mathcal{F}_L .

In the next section, the final step toward the complete formulation of the equations is taken by introducing the deployment and its effects, as well as specifying the assumptions adopted.

3.4.1 Deployment's effect on the equations of motion

As anticipated in the previous sections, the focus of this work will be shifted toward the analysis of the system's deployment starting from a packed configuration. In this case, the system evolves from an initial condition where the tether is partially wound around each of the two satellites to a state in which the tether is fully deployed. The most challenging aspect to handle from the equations' perspective is the time variability of the deployed mass. There are essentially two alternatives. The first assumes a constant mass for each lumped mass element composing the tether, while considering the number of such lumped masses as variable. The second approach, instead, assumes a constant number of elements and allows their mass to vary. The choice falls on the second alternative for computational simplicity, since it is easier to manage a state vector with a fixed number of variables rather than having to deal with a state vector whose dimensions change progressively.

In order to maintain the consistency of the analysis it is important to correctly account for both the mass and length variability, which lead to the appearance of new terms in the kinematic and dynamic equations - which will be referred to as 'convective terms'. In particular, the variation of the tether deployed length, and consequently of the mass distribution, essentially affects the dynamics of the internal masses and must be correctly accounted for in order to ensure the proper formulation of the equations of motion.

Let us now recall the node-based subdivision proposed in 3.5 and apply it to the case of a generic instant in time:

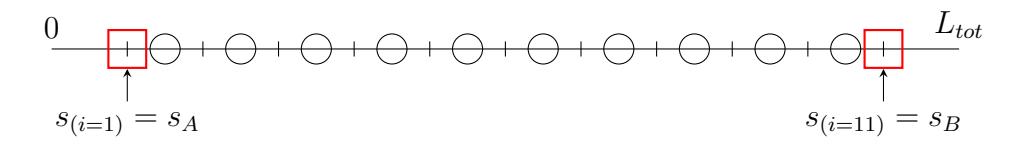


Figure 3.9: TSS modeling at a generic instant

Each of the previously defined material coordinates s_i is now time-varying. Consequently, the position vector of the j-th mass ρ_j will vary over time not only as a result of the orbital dynamics, but also as a function of the evolution of the s coordinate.

$$\boldsymbol{\rho}_{i}(s(t), t) \tag{3.46}$$

Let us now differentiate with respect to time the latter expression. Unlike the case of a constant tether length, we have:

$$\dot{\boldsymbol{\rho}}_{j}(s(t),t) = \frac{d}{dt}\left(\boldsymbol{\rho}_{j}(s(t),t)\right) = \frac{\partial \boldsymbol{\rho}_{j}}{\partial t} + \frac{\partial \boldsymbol{\rho}_{j}}{\partial s}\frac{\partial s}{\partial t}$$
(3.47)

By appropriately developing the final expression in 3.47, the new kinematic equation is obtained:

$$\dot{\boldsymbol{\rho}}_{j} = \frac{\partial \boldsymbol{\rho}_{j}}{\partial t} + \frac{1}{\bar{l}\Delta\xi} \left[\frac{ds_{A}}{dt} \tilde{\boldsymbol{r}}(\xi, t) + \frac{d\bar{l}}{dt} \xi \tilde{\boldsymbol{r}}(\xi, t) \right]_{\xi_{j-1}}^{\xi_{j}}$$
(3.48)

Taking a step forward, according to the Newton's second law:

$$\mathbf{F}_{ext,j} = \frac{d\mathbf{p}_j}{dt} = \frac{d(m_j \dot{\boldsymbol{\rho}}_j)}{dt} = m_j \frac{d\dot{\boldsymbol{\rho}}_j}{dt} + \dot{\boldsymbol{\rho}}_j \frac{dm_j}{dt}$$
(3.49)

where, \mathbf{F}_j is the vector of the resultant forces acting on the system, \mathbf{p}_j is the linear momentum of the j-th mass, and m_j its mass. By inverting the last equation and isolating the acceleration term:

$$\frac{d^2}{dt^2}(\boldsymbol{\rho}_j(s(t),t)) = \frac{\mathbf{F}_{ext,j}}{m_j} - \dot{\boldsymbol{\rho}}_j \frac{\dot{m}_j}{m_j}$$
(3.50)

A proper development of this formulation yields the final form of the dynamic equation:

$$\ddot{\boldsymbol{\rho}}_{j,L}^{L} = (\mathbf{a}_{G,j} + \mathbf{a}_{D,j} - \ddot{\mathbf{R}})^{L} - I_{terms,j}^{L} + C_{D,terms,j}^{L} + \frac{\mathbf{T}_{j}^{L}}{m_{j}} + \mathbf{u}_{j}^{L}$$
(3.51)

For compactness, the following terms have been introduced: $I_{terms,j}$ that contains the contributions arising from the rotational inertial effects, $C_{K,terms,j}$ who represents the convective term of the kinematic equation, and $C_{D,terms,j}$ which comprises the convective terms of the dynamic equation.

$$I_{terms,j} = \mathbf{\Omega} \times \mathbf{\Omega} \times \boldsymbol{\rho}_j + \dot{\mathbf{\Omega}} \times \boldsymbol{\rho}_j + 2\mathbf{\Omega} \times \dot{\boldsymbol{\rho}}_{j,L}$$
(3.52)

$$C_{K,terms,j} = \frac{1}{\bar{l}\Delta\xi} \left[\frac{ds_A}{dt} \tilde{\boldsymbol{r}}(\xi,t) + \frac{d\bar{l}}{dt} \xi \tilde{\boldsymbol{r}}(\xi,t) \right]_{\xi_{j-1}}^{\xi_j}$$
(3.53)

$$C_{D,terms,j} = -\frac{\dot{m}_j}{m_j} \dot{\boldsymbol{\rho}}_{j,L} + \frac{\mu_t}{m_j} \left[\frac{ds_j}{dt} \tilde{\mathbf{v}}(s_j, t) - \frac{ds_{j-1}}{dt} \tilde{\mathbf{v}}(s_{j-1}, t) \right]$$
(3.54)

We can specify here that $\tilde{\mathbf{r}}$ and $\tilde{\mathbf{v}}$ refer, respectively, to the position and velocity of the nodes s_i . These positions and velocities correspond to points whose dynamics are not integrated into the system. They are obtained using a finite element approximation that relies on the positions and velocities of the lumped masses, according to which:

$$\tilde{\mathbf{r}} = \tilde{\mathbf{r}}(s(\xi_j), t) = \frac{1}{2}(\boldsymbol{\rho}_j + \boldsymbol{\rho}_{j+1})$$
(3.55)

$$\tilde{\mathbf{v}} = \tilde{\mathbf{v}}(s(\xi_j), t) = \frac{1}{2}(\dot{\boldsymbol{\rho}}_j + \dot{\boldsymbol{\rho}}_{j+1})$$
(3.56)

It should be recalled here that the index j refers to the masses that actually compose our model, whereas the index i refers to the nodes used to subdivide the tether. However, for the sake of clarity the equations written in these section rely solely on the index j. It is possible, nevertheless, to identify a relationship between the two indexes: each of the j-th internal mass $(j = 2,3,...,N_{tot}-1)$ is preceded by a node s_i whose index i is equal to j-1 and followed by a node whose index i+1 is equal to j.

Regarding the end masses it is necessary to account for the mass of the satellite itself and for the mass of the portion of tether coiled inside the satellite. Consequently as the tether is deployed, the end masses decrease. Accordingly, the equation of motion for j = 1 and j = N should be changed by adding a term that accounts for the variation in satellite mass. However, given the order of magnitude of the tether mass compared to that of the satellite itself, it is considered a reasonable approximation to leave the equations unchanged, without introducing additional terms. The kinematic and dynamic equations, for j = 1 and $j = N_{tot}$, are therefore as follows:

$$\dot{\boldsymbol{\rho}}_{j}^{L} = \frac{d\boldsymbol{\rho}_{j}^{L}}{dt} \tag{3.57}$$

$$\ddot{\boldsymbol{\rho}}_{j,L}^{L} = (\mathbf{a}_{G,j} + \mathbf{a}_{D,j} - \ddot{\mathbf{R}})^{L} - I_{terms,j}^{L} - \frac{\dot{m}_{j}}{m_{j}} \dot{\boldsymbol{\rho}}_{j,L} + \frac{\mathbf{T}_{j}^{L}}{m_{j}} + \mathbf{u}_{j}^{L}$$
(3.58)

Let us now specify a few assumption that were made during the writing of the code. First of all the system is destined to be used only in circular or near circular orbit. Thus, in the orbital parameters the eccentricity e is allowed to vary between 0 and 0.01. Considering such values it is reasonable to assume negligible the Euler contribution in the inertial terms (3.52), since $\dot{\Omega} \simeq 0$ is accepted to be a correct approximation. Secondly, it is important to precise that the control action can be applied only on the satellites at the extremities of the tether. While the lumped masses conceptually also represent the small antenna elements composing the space-based radar sounder, these sensors are too small to be treated as independent satellite entities capable of housing an internal control system. Finally, the mass of the tethered lumps neglects the weight of the actual remote sensing system, as defining this mass falls entirely outside the scope of this study.

Given this assumptions we can now rewrite the final form of the equations of motion integrated in the code for each of the masses of the system. For the two end masses the equations are:

$$\dot{\boldsymbol{\rho}}_{j}^{L} = \frac{d\boldsymbol{\rho}_{j}^{L}}{dt} \tag{3.59}$$

$$\ddot{\boldsymbol{\rho}}_{j,L}^{L} = (\mathbf{a}_{G,j} + \mathbf{a}_{D,j} - \ddot{\mathbf{R}})^{L} - I_{terms,j}^{L} + C_{D,terms,j}^{L} + \frac{\mathbf{T}_{j}^{L}}{m_{j}} + \mathbf{u}_{j}^{L}$$
(3.60)

while for the N_{int} lumped masses representing the tether, the kinematic and dynamic equations are given as follows:

$$\dot{\boldsymbol{\rho}}_{j} = \frac{\partial \boldsymbol{\rho}_{j}}{\partial t} + C_{K,terms,j} \tag{3.61}$$

$$\ddot{\boldsymbol{\rho}}_{j,L}^{L} = (\mathbf{a}_{G,j} + \mathbf{a}_{D,j} - \ddot{\mathbf{R}})^{L} - I_{terms,j}^{L} - \frac{\dot{m}_{j}}{m_{j}} \dot{\boldsymbol{\rho}}_{j,L} + \frac{\mathbf{T}_{j}^{L}}{m_{j}}$$
(3.62)

where:

$$I_{terms,j} = \mathbf{\Omega} \times \mathbf{\Omega} \times \boldsymbol{\rho}_j + 2\mathbf{\Omega} \times \dot{\boldsymbol{\rho}}_{j,L}$$
 (3.63)

$$C_{K,terms,j} = \frac{1}{\bar{l}\Delta\xi} \left[\frac{ds_A}{dt} \tilde{\boldsymbol{r}}(\xi,t) + \frac{d\bar{l}}{dt} \xi \tilde{\boldsymbol{r}}(\xi,t) \right]_{\xi_{j-1}}^{\xi_j}$$
(3.64)

$$C_{D,terms,j} = -\frac{\dot{m}_j}{m_j} \dot{\boldsymbol{\rho}}_{j,L} + \frac{\mu_t}{m_j} \left[\frac{ds_j}{dt} \tilde{\mathbf{v}}(s_j, t) - \frac{ds_{j-1}}{dt} \tilde{\mathbf{v}}(s_{j-1}, t) \right]$$
(3.65)

As will be better specified in the next chapter - specifically in Section 4.1.1 -, the code is structured in a way that the user can specify in the initialization phase the type of analysis to be conducted leading to the activation - or not - of the different terms in the equations of motion.

Finally, the system of Ordinary Differential Equations can be written in a compact form as follows:

$$\dot{X} = \begin{bmatrix} \dot{\mathbf{R}}^{ECI}_{j} & \vdots & \vdots \\ \ddot{\mathbf{R}}^{ECI}_{j,L} & \vdots \\ \dot{\rho}_{1,L}^{L} & \vdots \\ \dot{\rho}_{j,L}^{L} & \vdots \\ \dot{\rho}_{N_{tot},L}^{L} \end{bmatrix} = \begin{bmatrix} \dot{\mathbf{R}}^{ECI}_{j} & \vdots & \vdots \\ \ddot{\mathbf{R}}^{ECI}_{j,L} & \vdots \\ \ddot{\rho}_{N_{tot},L}^{L} & \vdots \\ \dot{\rho}_{N_{tot},L}^{L} &$$

3.5 Equations of motion for the dumbbell model

The difference in the modeling of the system inevitably extends to the equations of motion, where, as previously mentioned, the simplification becomes once again evident. The common thread linking the two formulations lies in the fact that the dynamics of the TSS are interpreted with respect to the local reference frame centered on the center of mass. Nevertheless, the resulting mathematical structure assumes a completely different form, reflecting the different assumptions adopted.

Let us first of all recall the system's representation given in 3.7 and place it within the global reference frame identifying at the same time the elements required for the formulation of the equations of motion.

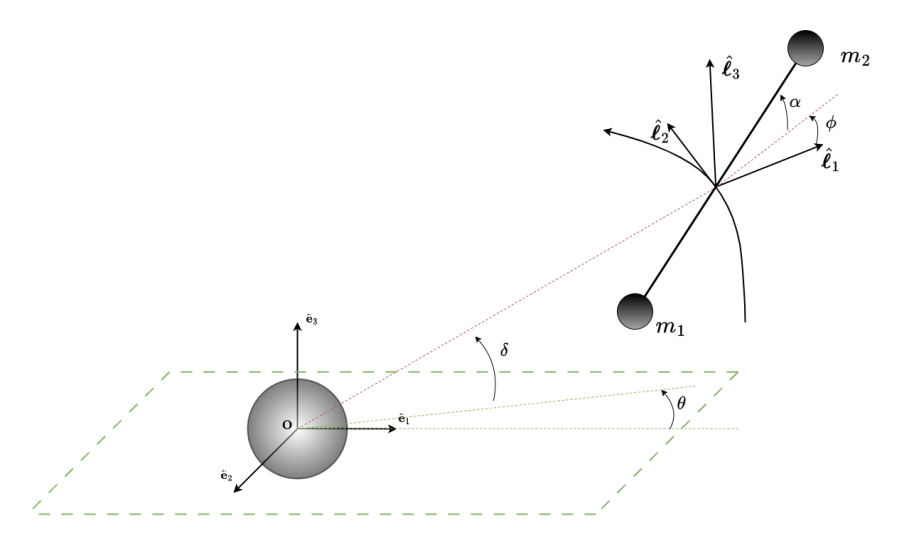


Figure 3.10: Rigid tether model

This figure includes the coordinates required to describe the state of the TSS in the dumbbell model. Three of these coordinates are related to the orbit: the orbital radius R, the latitude of the Center of Mass θ and its altitude δ . The other three are directly related to the tether: the tether length L, the in-plane angle ϕ and the out-of-plane α . Based on these coordinates - referred to as generalized coordinates - , the first step is to formulate and define the position vectors of the two satellites in the global reference frame.

$$\mathbf{R}_{1} = \left(R \cos \theta + \frac{L}{2} \cos \alpha \cos(\phi + \theta) \right) \hat{\mathbf{e}}_{1}$$

$$+ \left(R \sin \theta + \frac{L}{2} \cos \alpha \sin(\phi + \theta) \right) \hat{\mathbf{e}}_{2}$$

$$+ \left(R \sin \delta + \frac{L}{2} \sin \alpha \right) \hat{\mathbf{e}}_{3}$$

$$(3.67)$$

$$\mathbf{R}_{2} = \left(R \cos \theta - \frac{L}{2} \cos \alpha \cos(\phi + \theta) \right) \hat{\mathbf{e}}_{1}$$

$$+ \left(R \sin \theta - \frac{L}{2} \cos \alpha \sin(\phi + \theta) \right) \hat{\mathbf{e}}_{2}$$

$$+ \left(R \sin \delta - \frac{L}{2} \sin \alpha \right) \hat{\mathbf{e}}_{3}$$
(3.68)

This represents the starting point for determining the kinetic and potential energy terms, which are then used within a Lagrangian formulation leading to the final form of the equations of motion.

As the end masses are modeled as point masses, the kinetic energy of the system accounts only for to the translational motion of the two bodies. Hence, it can be written as:

$$E_k = \frac{1}{2}m_1 \|\dot{\mathbf{R}}_1\|^2 + \frac{1}{2}m_2 \|\dot{\mathbf{R}}_2\|^2$$
(3.69)

The gravitational potential energy is simply given by the contribution of the two end masses interacting with the Earth's gravity field, and can be written as:

$$E_p = -\frac{\mu_{\oplus} m_1}{\|\mathbf{R}_1\|} - \frac{\mu_{\oplus} m_2}{\|\mathbf{R}_2\|}$$
 (3.70)

Finally, to formulate the equations of motion it is sufficient to define the Lagrange function and substitute it into the Lagrange equations:

$$L = E_k - E_p \tag{3.71}$$

$$\frac{d}{dt} \left(\frac{\partial L}{\partial \dot{q}_i} \right) - \frac{\partial L}{\partial q_i} = Q_i, \tag{3.72}$$

where q_i is the generalized coordinate and Q_i is the generalized force.

By performing this derivation for each of the generalized coordinates, a set of differential equations describing the system's dynamics is obtained. In this section, the transition from the set of six time-dependent differential equations to a set of three equations with respect to the true anomaly is omitted; nevertheless, by carrying out this change of variable, the final formulation can be expressed as follows:

$$\phi'' = 2(\phi' + 1) \left(\frac{e \sin \nu}{1 + e \cos \nu} + \phi' \tan \alpha - \frac{L'}{L} \right) - \frac{3}{2} \frac{\sin 2\phi}{1 + e \cos \nu}$$
 (3.73)

$$\alpha'' = \frac{2e\sin\nu}{1 + e\cos\nu}\alpha' - 2\frac{L'}{L}\alpha' - \frac{1}{2}\left((\phi' + 1)^2 + \frac{3\cos^2\phi}{1 + e\cos\nu}\right)\sin 2\alpha \tag{3.74}$$

$$L'' = \frac{2e\sin\nu}{1 + e\cos\nu}L' + L\left(\alpha'^2 + (\phi' + 1)^2\cos^2\alpha + \frac{3\cos^2\phi\cos^2\alpha - 1}{1 + e\cos\nu}\right)$$
(3.75)

This set of equations corresponds to a set of assumptions in which the tether's mass is considered negligible, and therefore its contribution to the kinetic and potential energy terms is ignored. If the tether's mass were to be included, only a few additional terms and minor modifications of some coefficients would be required; however, the overall system dynamics would remain essentially unchanged. Similarly, all energy contributions related to external disturbances - such as solar radiation, aerodynamic drag, and electrodynamic forces, as well as gravitational perturbations caused by the Earth's oblateness - are considered negligible. This

last assumption is considered to be acceptable for the use of this model, as it is intended solely for a preliminary analysis.

Regarding the implementation of the deployment, it is sufficient to impose the desired law in terms of $\dot{L}(t)$. Finally, as done in the previous section, the system of Ordinary Differential Equations is reported in compact form:

$$\dot{X} = \begin{bmatrix} \dot{\phi} \\ \ddot{\phi} \\ \dot{\alpha} \\ \dot{L} \\ \ddot{L} \end{bmatrix} = \begin{bmatrix}
\phi' = \frac{d\phi}{d\nu} \\
\phi'' = 2(\phi' + 1) \left(\frac{e \sin \nu}{1 + e \cos \nu} + \phi' \tan \alpha - \frac{L'}{L} \right) - \frac{3}{2} \frac{\sin 2\phi}{1 + e \cos \nu} \\
\alpha' = \frac{d\alpha}{d\nu} \\
\alpha'' = \frac{2e \sin \nu}{1 + e \cos \nu} \alpha' - 2 \frac{L'}{L} \alpha' - \frac{1}{2} \left((\phi' + 1)^2 + \frac{3 \cos^2 \phi}{1 + e \cos \nu} \right) \sin 2\alpha \\
L'' = \frac{2e \sin \nu}{1 + e \cos \nu} L' + L \left(\alpha'^2 + (\phi' + 1)^2 \cos^2 \alpha + \frac{3 \cos^2 \phi \cos^2 \alpha - 1}{1 + e \cos \nu} \right)
\end{bmatrix} \tag{3.76}$$

Chapter 4

Numerical Simulation

The main stage in the analysis of space system dynamics is the development of dedicated software for the simulation of the system's behavior. Such software enables the correct implementation of the mathematical model and provides a means to extract and interpret the solutions it can deliver. These systems are usually rather complex, often involving a large number of equations to be integrated - equations that, as in our case, may also be stiff. The objective at this stage is therefore to design a code capable of consistently integrating the differential equations that govern the evolution of the system's state, ensuring the required accuracy while, at the same time, minimizing as much as possible the computational cost.

In this chapter, following the previous ones in which the system under analysis and the mathematical tools adopted to describe it have been introduced, the architecture of the code developed in MATLAB for the study of the dynamics of the Tethered Satellite System is presented. Following the initialization of the system parameters and orbital conditions, the code integrates the differential equations governing the system's motion, consistently accounting for both the internal dynamics and the external perturbations - depending on the tether model selected. Then, to facilitate a comprehensive understanding of the system behavior, the output data of the simulation are subsequently processed through a dedicated post-processing framework. This phase allows for the extraction of key indicators and the elaboration of graphical representations, such as for relative positions and velocities, or in-plane and out-of-plane angles.

It is noteworthy to highlight that code structure also facilitates the scalability, enabling the analysis of the system under different configurations and scenarios.

4.1 Code Structure

An intelligent structuring of the code allows each phase of the analysis to be examined independently, in a manner that is both simple and intuitive. The code can be decomposed into three main parts, within which different functions are called to execute specific tasks, ensuring ease of maintenance throughout the simulation workflow. It should be noted that in this section the discussion refers exclusively to the use of the discrete model; however, the basic structure remains the same for the dumbbell model, with a significant reduction in the complexity of each stage.

4.1.1 Initialization

First of all, the user can define the various available simulation options. This begins with the input of the initial data required to determine the state vector under the initial conditions: the orbital parameters. By defining the orbital parameters, the reference orbit that the system's center of mass is intended to follow, as well as its initial position along this orbit, are determined. This also establishes the position of the Local Orbital Reference Frame \mathcal{F}_L . During this phase, it is also necessary to specify the configuration in which the system is to be studied, as well as the model to be used to study the system's dynamics and, eventually, the number of lumped masses used to discretize the tether. This completes the second step in the formulation of the initial state vector: it is now possible to define the position and velocity, within the local reference frame, of each mass composing the system in the case of the lumped-masses model. The state vector assumes the following form:

$$X = \begin{bmatrix} X_{cm} \\ X_1 \\ X_2 \\ \vdots \\ X_{N_{tot}} \end{bmatrix}$$

$$(4.1)$$

here the state of each mass is composed by six elements:

$$X_j = \begin{bmatrix} x_j & y_j & z_j & \dot{x}_j & \dot{y}_j & \dot{z}_j \end{bmatrix}^T \tag{4.2}$$

The size of this vector is directly proportional to the number of lumped masses considered. Specifically, the first six elements represent the state - in terms of position and velocity - of the system's Center of Mass with respect to the Earth in the \mathcal{F}_{ECI} reference frame, while each of the masses representing the tether

corresponds to six elements describing its position and velocity relative to the Center of Mass in the local reference frame \mathcal{F}_L , for a total of 6+6N state variables.

For clarity during the various stages of the simulation, once the details regarding the configuration and the number of lumped masses for the tether have been provided, two indexing vectors are generated. These vectors allow the positions and velocities of the individual masses to be extracted separately, yielding the following vectors:

$$\begin{bmatrix} x_1 \\ y_1 \\ z_1 \\ x_2 \\ y_2 \\ y_2 \\ z_2 \\ \vdots \\ x_N \\ y_N \\ z_N \end{bmatrix} \begin{bmatrix} \dot{x}_1 \\ \dot{y}_1 \\ \dot{z}_1 \\ \dot{x}_2 \\ \dot{y}_2 \\ \dot{y}_2 \\ \dot{z}_2 \\ \vdots \\ \dot{x}_N \\ \dot{y}_N \\ \dot{z}_N \end{bmatrix}$$

$$(4.3)$$

These index vectors allow to accurately assign and extract the state of each individual mass, a step that proves useful throughout all stages of the analysis, from initialization to integration and post-processing. Furthermore, during the initialization all the necessary data and parameters - ranging, for example, from the initial mass values to the specific perturbation coefficients - are defined and collected into a single structure array, which is then passed to the integrator.

Finally, it is possible to specify the type of analysis to be conducted. This includes selecting which of the previously introduced perturbations to account for, defining the number of orbital periods over which the system will be simulated, and deciding whether to investigate the transition from the compact configuration to the fully deployed state or, alternatively, to focus on the dynamics and stability at a fixed deployed tether length. Furthermore, the user is required to select which deployment strategy is to be adopted, and whether or not active control should be included, specifying also which of the available controllers is to be employed. Similarly, it is also necessary to specify which analyses are to be included during the post-processing stage.

In the case of the dumbbell model, this initialization is again simpler, since it is sufficient to know the desired configuration and the tether parameters to establish the initial state vector.

4.1.2 Integration

The second phase starts by passing all the variables defined during initialization to the integration function through a structure array. The use of structure arrays ensures both compactness and clarity, and the same approach is adopted for the storage of output parameters. The integration function constitutes the core of the code, as it performs the numerical integration of the system dynamics and provides, as output, the time evolution of the state vector. Within this phase, all the necessary functions are activated to compute the accelerations governing the dynamics of the Tethered Satellite System. These include contributions from external perturbations, inertial terms, and, in the case of deployment, convective terms, as well as possible control accelerations. In this way, the complete set of differential equations that govern the system's motion is formulated and integrated.

These derivatives,- equal in number to the system states and corresponding to the time derivative of the state vector itself - are then integrated using the variable-step numerical integration algorithms provided by the coding environment. The choice of integration algorithm is particularly significant for problems characterized by complex dynamics; in this work, the MATLAB integrator ode113 has been adopted as the reference. Such integrators are designed to integrate the differential equations from time zero to the final time specified by the user during the initialization phase, employing a variable number of steps that automatically adapt to the stiffness of the equations being solved. By default, MATLAB stores all integration steps performed. In our case, however, given the dimension of the state vector, the stiffness of the ODEs, and the upper limits imposed on matrix sizes within MATLAB, it was necessary to restrict the number of stored steps by explicitly specifying the time instants to be saved. However, this adjustment does not compromise the accuracy of the integration; it only reduces the frequency with which the data are stored.

Each iteration, furthermore, begins by computing the position and orientation of the local reference frame from the data contained in the first six state variables - those associated with the center of mass - before proceeding with the calculations required to determine the relevant accelerations. Once all iterations are completed, the output of this phase consists of a vector containing the time instants and a matrix containing the corresponding state evolution. In this way, the complete time history of the system state is obtained, from the initial instant to the final time specified. These data, appended to the input structure array, serve as the basis for the post-processing phase.

4.1.3 Post-processing

The integration phase is the most computationally demanding. However, it is as central as it is sterile if not followed by a post-processing phase capable of giving

concrete form to the obtained results. The purpose of this section, therefore, is to generate plots that allow for a clear and intuitive visualization of the system's dynamic evolution. Furthermore, this phase serves to verify the correctness of the implemented equations and the simulation itself. Among other checks, it ensures compliance with fundamental physical principles, such as the conservation laws, the work-energy principle, but also the cancellation of the net tether forces acting on the center of mass and of convective terms, all of which correspond to internal forces.

After completing the post-processing of the data, the primary outputs are represented through the following plots:

- Evolution with respect to time of radial, along-track and across-track position of different bodies, represented with respect to the center of mass of the system;
- Evolution with respect to time of radial, along-track and across-track velocity of different bodies with respect to the center of mass of the system;
- Evolution with respect to time of total tether length;
- In the case where the system is controlled, the evolution of forces acting on each satellite.

In conclusion, a schematic representation of the code structure, as described in this section, is presented below.

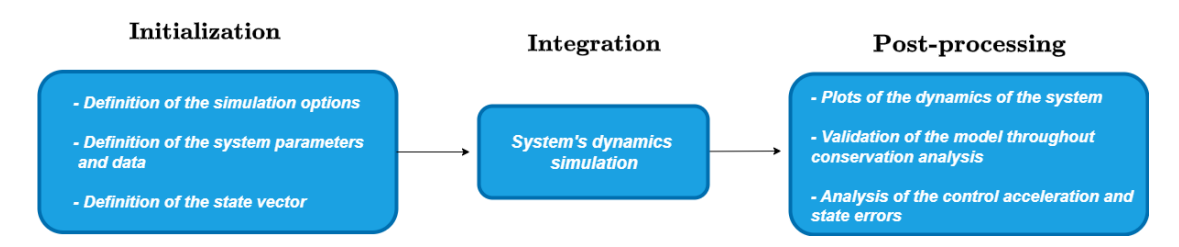


Figure 4.1: Schematic representation of the code's structure

Chapter 5

Numerical Results

Once the theoretical framework has been established - with the definition of the mathematical tools, the formulation of the equations, and the implementation of the simulation code - it is now time to perform the actual simulations. In order to do so, this chapter presents in detail the system under investigation, providing its reference data and parameters and then moving forward towards the presentation of the first indicative results, that are reported to offer a preliminary interpretation of the system's dynamics. By observing the simulated dynamics, it becomes possible to assess the effects of external perturbations, internal forces, and generally the system's response under different operating conditions. First, the natural dynamics of the system are examined, offering a baseline picture of its orbital behavior in the absence of deployment maneuvers and providing an insight into the inherent tendencies of the system. Each of the known configurations will be analyzed, thereby, confirming which one tends to exhibit stable behavior and which, on the contrary, proves to be naturally unstable. In the second stage, attention shifts to the deployment phase, where the system's modeling and simulation are subjected to an additional level of complexity. The results presented in this chapter, therefore, represent a first step towards the understanding of the TSS dynamics, which is essential for the subsequent design and implementation of control strategies.

5.1 Simulation set-up

Delving into a more specific section, the selection of the system to be analyzed and the orbital parameters are guided by the initial motivation behind this research: the use of a tethered satellite system - in a cross-track configuration - for space based radar sounding. Thus, in this section, the Tethered Satellite System under analysis, its defining characteristics, and the orbital conditions chosen for the simulation are presented. Subsequently, the first results obtained are illustrated,

providing the reader with an understanding of the system's behavior in different scenarios, both in terms of configuration and deployment process. As a final remark, it is important to highlight that the analysis reported here relies on the lumped-masses model.

As a first instance we specify the orbital parameters that determine the position the Local Orbital Frame \mathcal{F}_L - centered on the system's Center of Mass:

Orbital Parameters	Values	Unit
Right Ascendind of the Ascensione Node (RAAN)	0	[deg]
Inclination (i)	0	[deg]
Semi Major Axis (a)	6578.5	[Km]
Eccentricity (e)	0	[-]
Argument of Periapsis (w)	0	$[\deg]$
True Anomaly (ν)	0	$[\deg]$

Table 5.1: Orbital Parameters

These data are, first of all, used to determine the Perifocal Frame \mathcal{F}_P associated with the system's orbit. Within this frame, the initial position and velocity of the system's Center of Mass relative Earth are established, and subsequently transformed into the ECI reference frame. Secondly, the orbital parameters serve as essential inputs for defining the characteristics of the surrounding environment, particularly the drag-related parameters C_d and ρ . In this study, however, this aspect is not investigated in detail, and standard values for these parameters are assumed. In particular, C_d is taken as a constant equal to 2, and ρ is considered constant as well, estimated from a reference table of the Harris-Priester model [43].

	Satellite A	Satellite B
Mass(m)	100 [Kg]	100 [Kg]
Surface (S)	$1 [\rm m^2]$	$1 [{ m m}^2]$

Table 5.2: Satellites Parameters

Table 5.2 presents the data for the two main satellites. In addition, the tether data are included in the table 5.3.

	Values	Unit
Length (L_{tot})	1000	m
Diameter (d)	1.7	$_{ m mm}$
Linear density (ρ_T)	10	Kg/Km
Young Modulus (E)	20.844	GPa
Damping (c)	47.312	Ns
Lumped masses number	10	[-]

Table 5.3: Tether Parameters

These values are based on the same parameters employed by Quadrelli and Lorenzini in their analysis of a Kevlar tether [47].

	Values	Unit
Mass (m)	1	Kg
Surface (S)	0.17	m^2

Table 5.4: Lumped masses Parameters

It should be noted that, in this study, the analysis simulates a space-based radar sounding system composed of arrays of small sensors connected by a structural tether. In this context, the lumped masses of the tether are also considered to physically represent the system's sensors. From the perspective of the equations of motion, they are treated as point masses. However, for the definition of certain accelerations - such as drag acceleration, or effects like solar radiation pressure, which is not considered here - it is necessary to assign a physical shape to these masses. Accordingly, the lumped masses are assumed to be cubic, and their characteristic parameters vary with the changes in the system. Specifically the variation is associated with the evolution of the tether's deployed length and thus the tether's deployed mass. The relevant parameters, namely mass and surface area, are expressed as functions of the deployed tether length as follows:

$$m_j = \rho_T \Delta \xi_j l \tag{5.1}$$

$$S_j = \Delta \xi_j ld \tag{5.2}$$

5.2 TSS free dynamics propagation

In this section, in order to provide a concise overview of the intrinsic dynamic behavior of a TSS - when subject exclusively to environmental perturbations, without

the influence of control actions - we present the results of a simulation carried out for the case of a fully deployed tether kept at a fixed length . All the perturbations previously introduced are considered, while the system is left in free evolution. Consequently, no convective terms arise, since no mass flow is present along the tether. The simulations have been performed over two orbital periods for each of the three reference configurations of a tethered system, which will be better illustrated in the following subsections.

5.2.1 Radial Configuration

In the radial configuration, the system deploys the tether along the radial direction, corresponding to the unit vector $\hat{\ell}_1$ of the local reference frame \mathcal{F}_L (2.2.3). A schematic representation is provided below to facilitate visualization of the configuration.

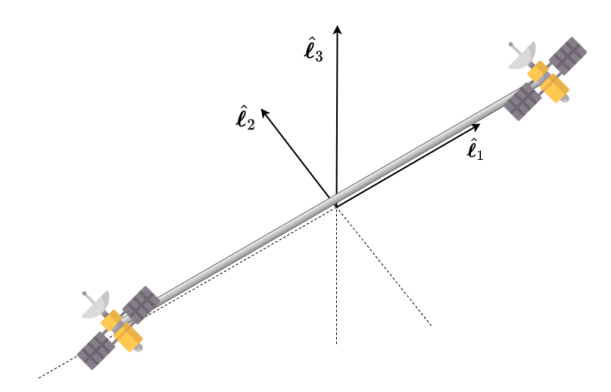


Figure 5.1: Illustrative representation of the radial configuration

In this case, the initial coordinates in the local reference frame that describe the positions of the two satellites are given by:

	$\hat{\boldsymbol{\ell}}_1 (x_L)$	$\hat{m{\ell}}_2 \; (y_L)$	$\hat{\boldsymbol{\ell}}_3 \; (z_L)$
Satellite A	500	0	0
Satellite B	-500	0	0

Table 5.5: Reference coordinates for the radial configuration

All the lumped masses representing the tether are consistently arranged along the line connecting the two end satellites.

Once the system's dynamics have been simulated, post-processing allows for the generation of plots that illustrate the evolution of each mass's position over time. These plots provide a clear visualization of the time history of the three coordinates of each mass, expressed relative to the system's Center of Mass within the local reference frame \mathcal{F}_L .

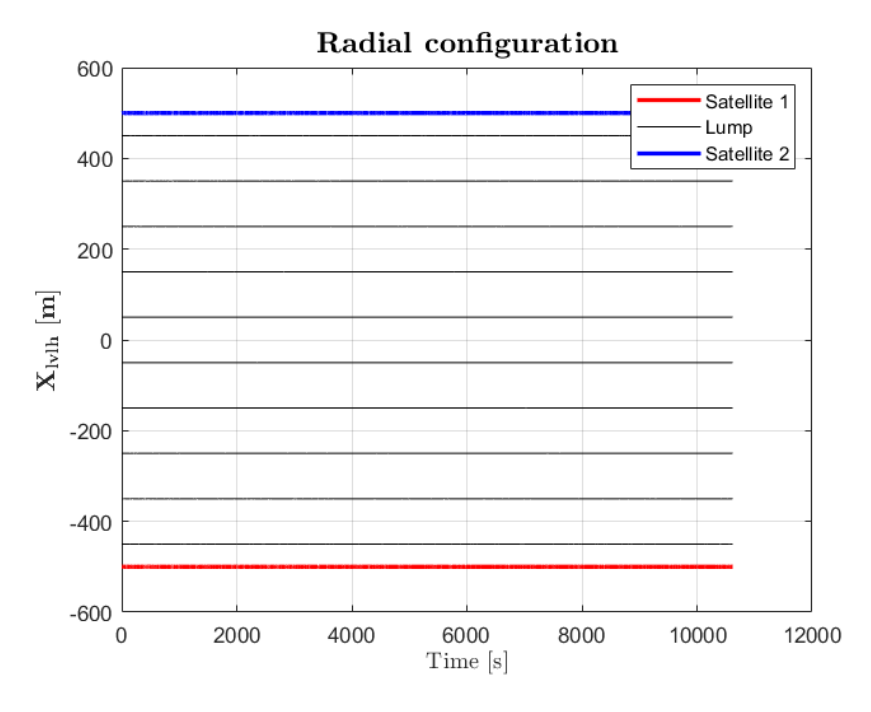


Figure 5.2: Radial configuration: evolution of the x–coordinate $(\hat{\ell}_1)$

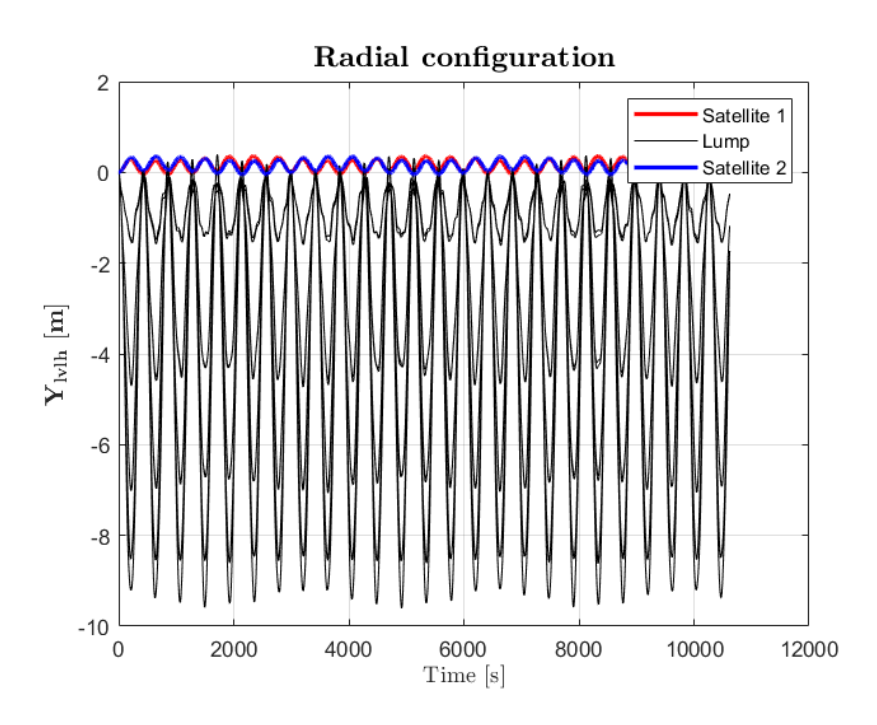


Figure 5.3: Radial configuration: evolution of the y-coordinate $(\hat{\ell}_2)$

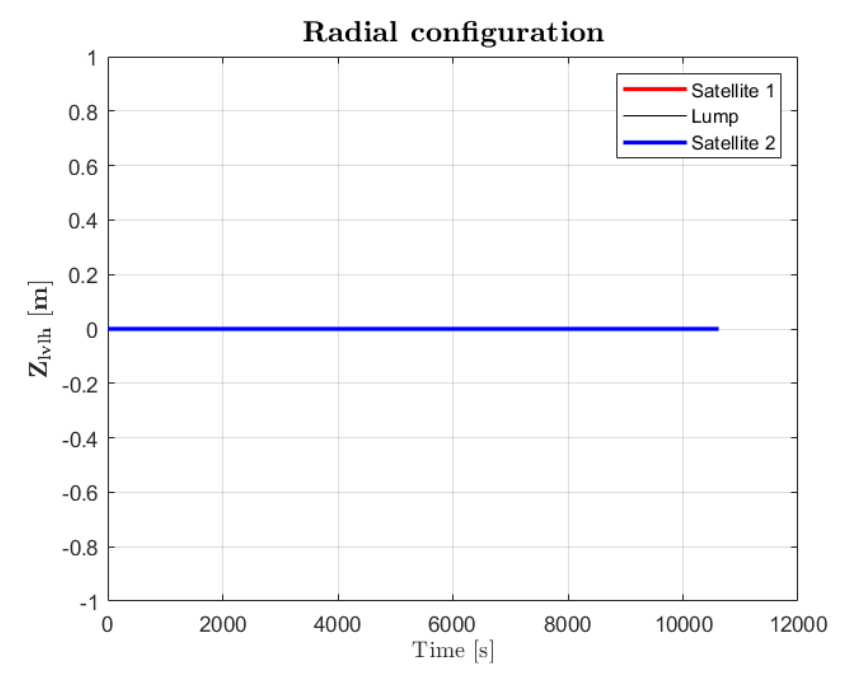


Figure 5.4: Radial configuration: evolution of the z-coordinate $(\hat{\ell}_3)$

As shown by the plots, each mass maintains an almost constant position. This configuration is, in fact, the naturally stable arrangement for tethered satellite systems. This stability originates from the gravity-gradient effect: the satellite closer to the Earth is attracted more strongly than the one farther away. The resulting net force keeps the tether under tension, thereby ensuring that the relative distances between the masses remain constant.

5.2.2 Along-track Configuration

In this configuration, the tether is deployed along the direction of motion of the system's Center of Mass, namely the along-track direction identified by the unit vector $\hat{\ell}_2$ of the local reference frame \mathcal{F}_L (2.2.3).

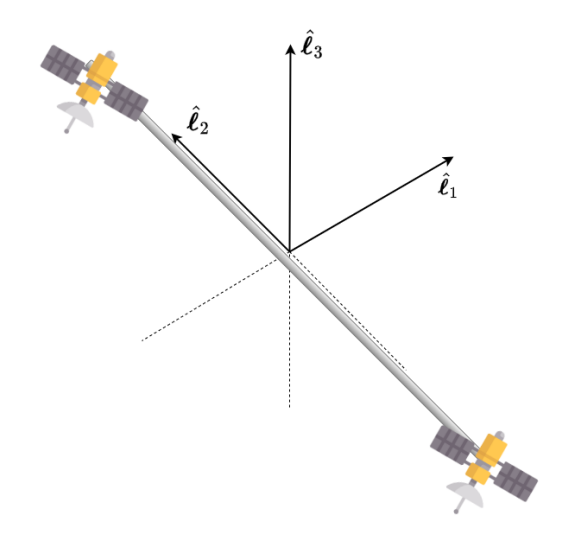


Figure 5.5: Illustrative representation of the along-track configuration

In this case, the coordinates that describe the positions of the two satellites in the local reference frame are the following:

	$\hat{\boldsymbol{\ell}}_1 (x_L)$	$\hat{\boldsymbol{\ell}}_2 \; (y_L)$	$\hat{\boldsymbol{\ell}}_3 \; (z_L)$
Satellite A	0	500	0
Satellite B	0	-500	0

Table 5.6: Reference coordinates for the along-track configuration

Once again, the lumped masses representing the tether are arranged along the line connecting the two end satellites. The system dynamics are illustrated in the following plots:

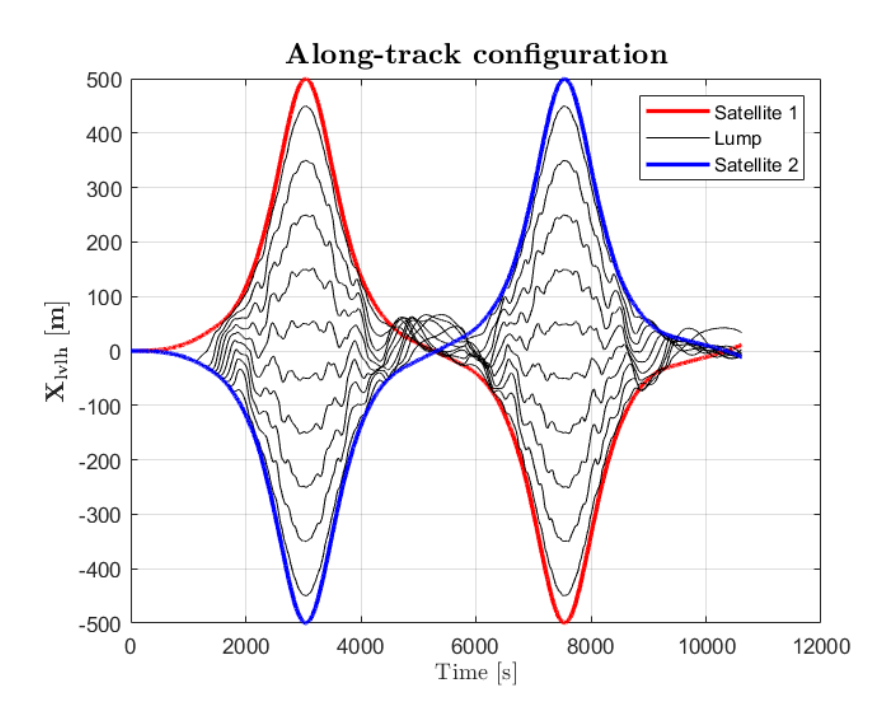


Figure 5.6: Along-track configuration: evolution of the x–coordinate $(\hat{\ell}_1)$

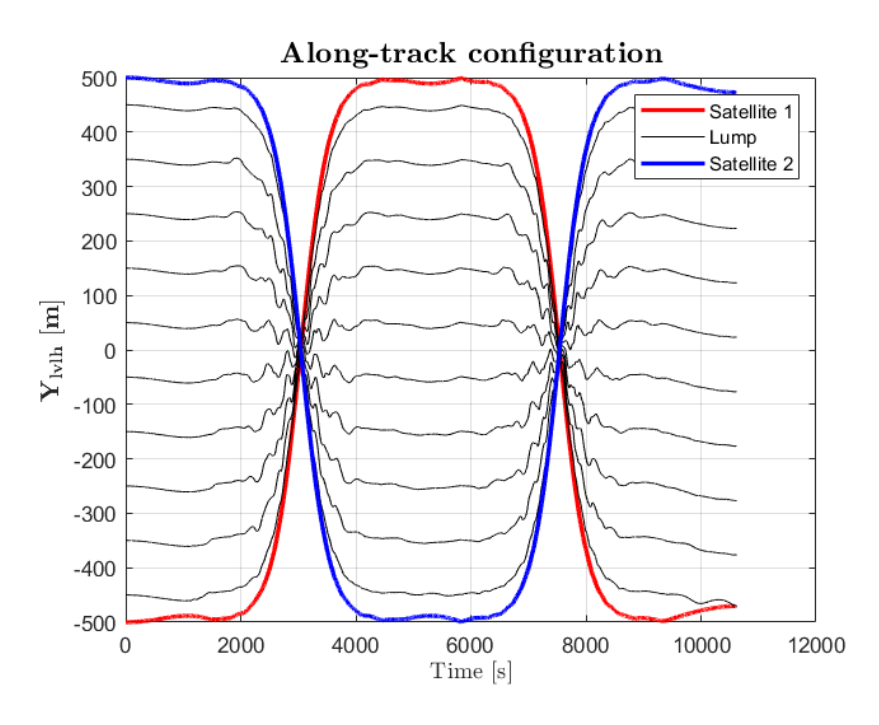


Figure 5.7: Along-track configuration: evolution of the y-coordinate $(\hat{\ell}_2)$

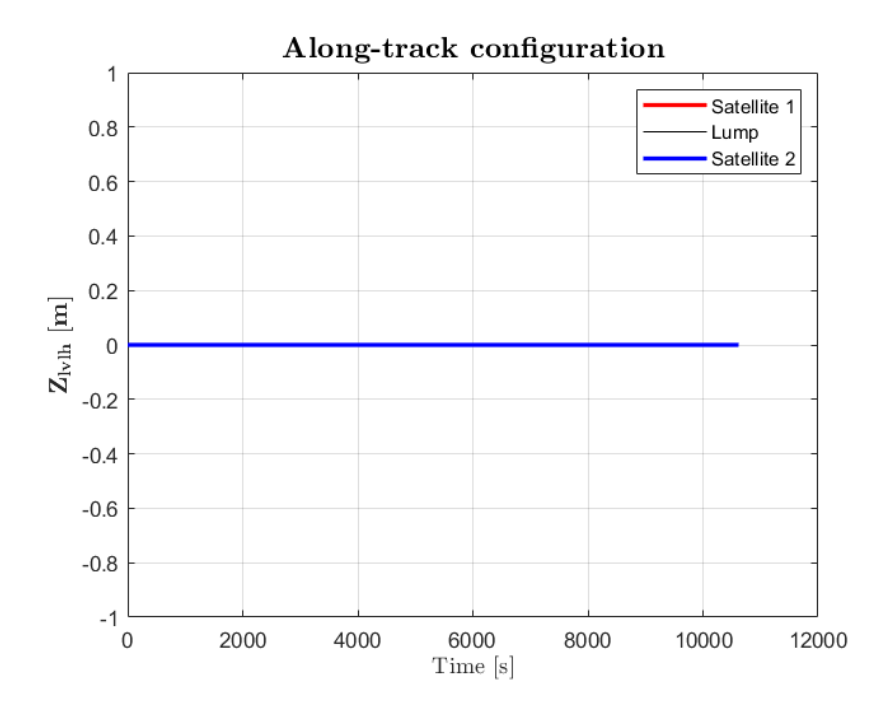


Figure 5.8: Along-track configuration: evolution of the z-coordinate $(\hat{\ell}_2)$

The along-track configuration is inherently unstable. As can be inferred from the plots, the system immediately begins to oscillate with respect to the direction of the angular momentum vector. In principle, the system exhibits a restoring tendency toward its naturally stable equilibrium, namely the radial configuration, although this attempt proves unsuccessful, with the dynamics persisting in oscillations between the two configurations

5.2.3 Cross-track Configuration

Finally, the configuration that will receive the greatest attention is the cross-track configuration. In this case, the tether is deployed in the direction perpendicular to the orbital plane, parallel to the unit vector $\hat{\ell}_3$ of the reference frame \mathcal{F}_L (2.2.3).

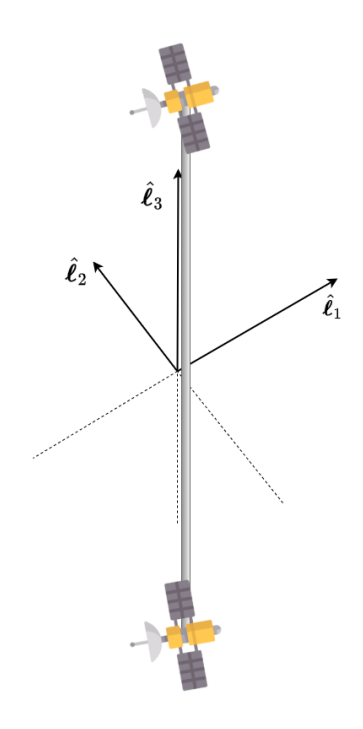


Figure 5.9: Illustrative representation of the cross-track configuration

The initial positions of the satellites are thus described by the following coordinates:

	$\hat{\boldsymbol{\ell}}_1 (x_L)$	$\hat{\boldsymbol{\ell}}_2 \; (y_L)$	$\hat{\boldsymbol{\ell}}_3 \; (z_L)$
Satellite A	0	0	500
Satellite B	0	0	-500

Table 5.7: Reference coordinates for the cross-track configuration

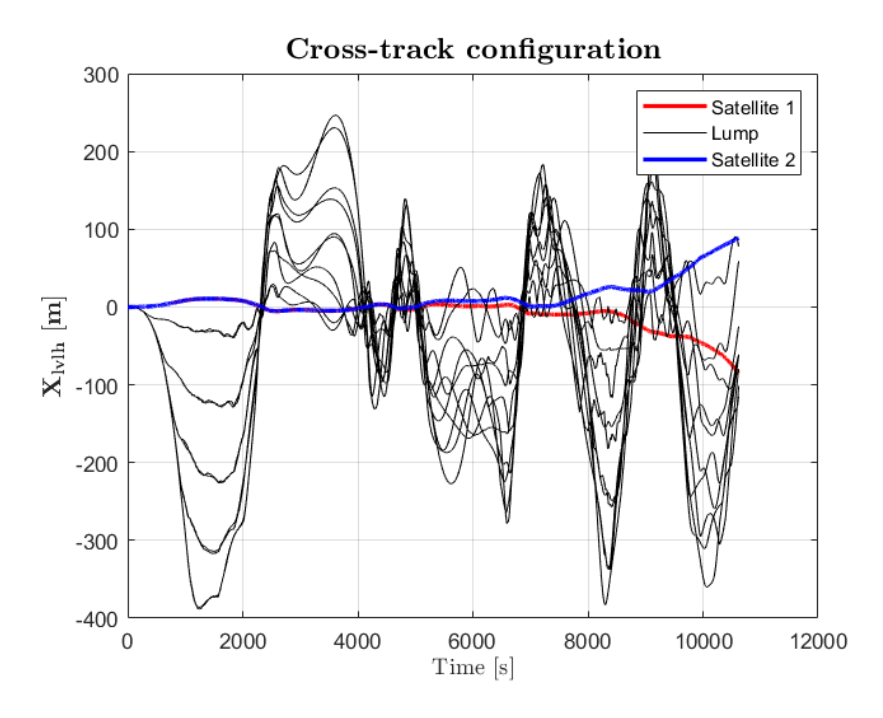


Figure 5.10: Cross-track configuration: evolution of the x–coordinate $(\hat{\boldsymbol{\ell}}_1)$

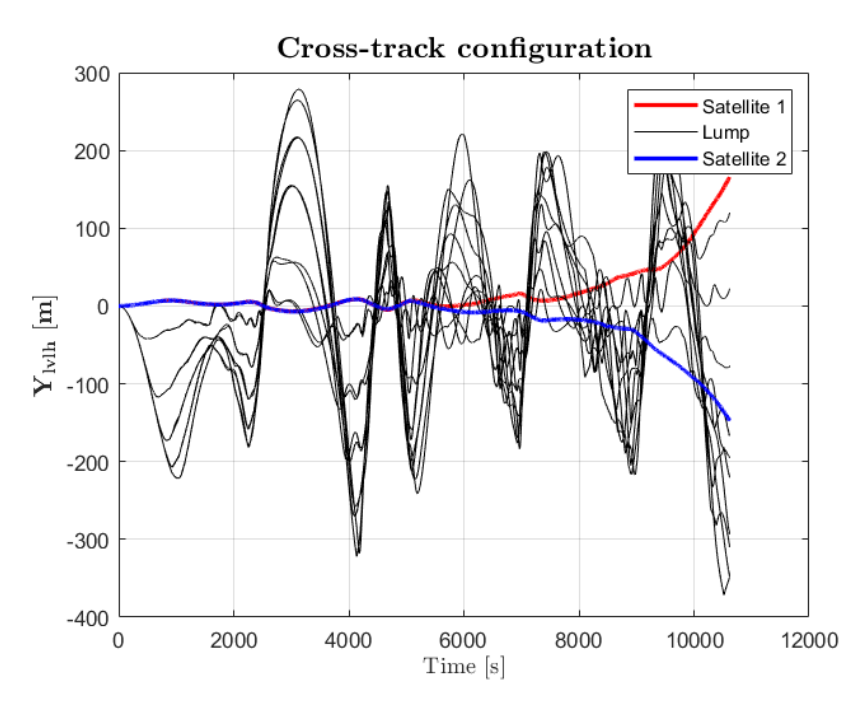


Figure 5.11: Cross-track configuration: evolution of the y-coordinate $(\hat{\ell}_2)$

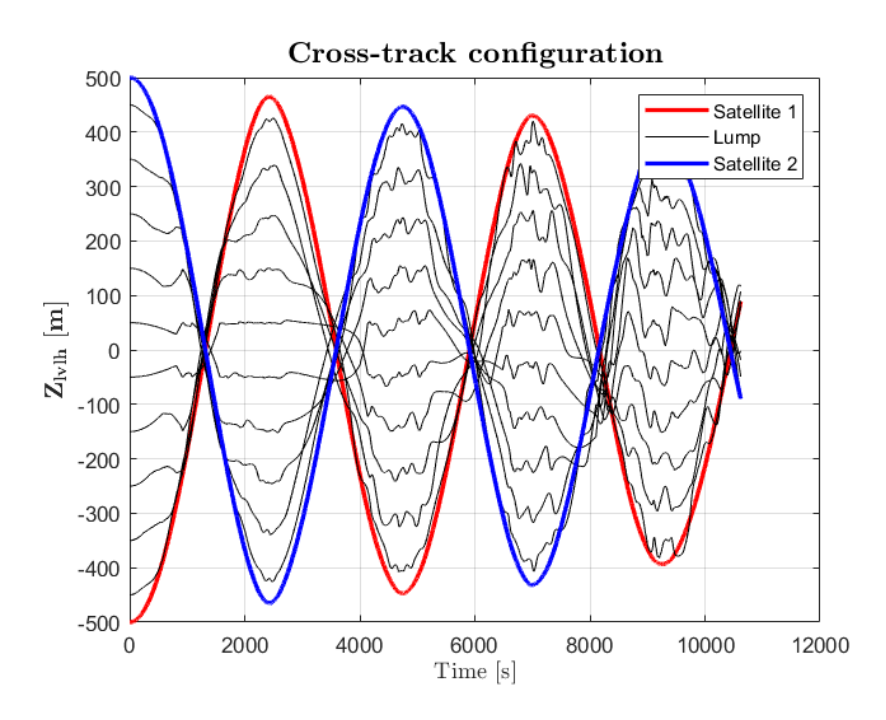


Figure 5.12: Cross-track configuration: evolution of the z-coordinate $(\hat{\ell}_3)$

Even in this case, the instability of the system is readily observable. This behavior can be demonstrated even in the absence of perturbative accelerations. Specifically, the masses in this configuration tend to behave as independent satellites on slightly inclined orbits relative to each other. The inclusion of perturbative accelerations merely amplifies this behavior, further reducing the system's overall stability. From the plots presented in the previous two subsections, it can be observed that the instabilities - primarily affecting the along-track and cross-track configurations - are not limited to small deviations from the ideal positions. For instance, by simulating the cross-track configuration over a longer duration - five orbital periods - it becomes evident, as shown in 5.15, how the system's motion is progressively altered and increasingly dominated by the perturbations.

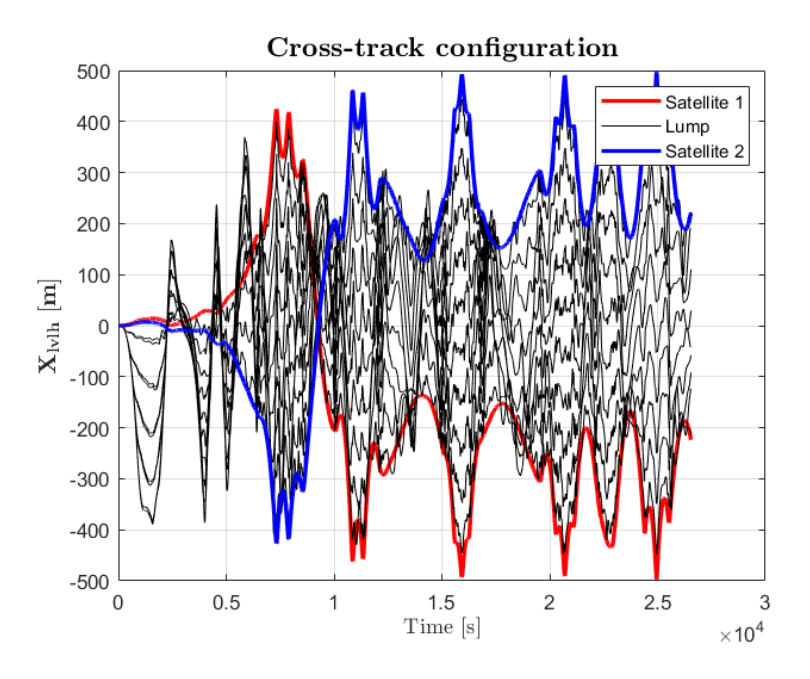


Figure 5.13: Cross-track configuration: evolution of the x-coordinate $(\hat{\ell}_1)$ over 5 periods

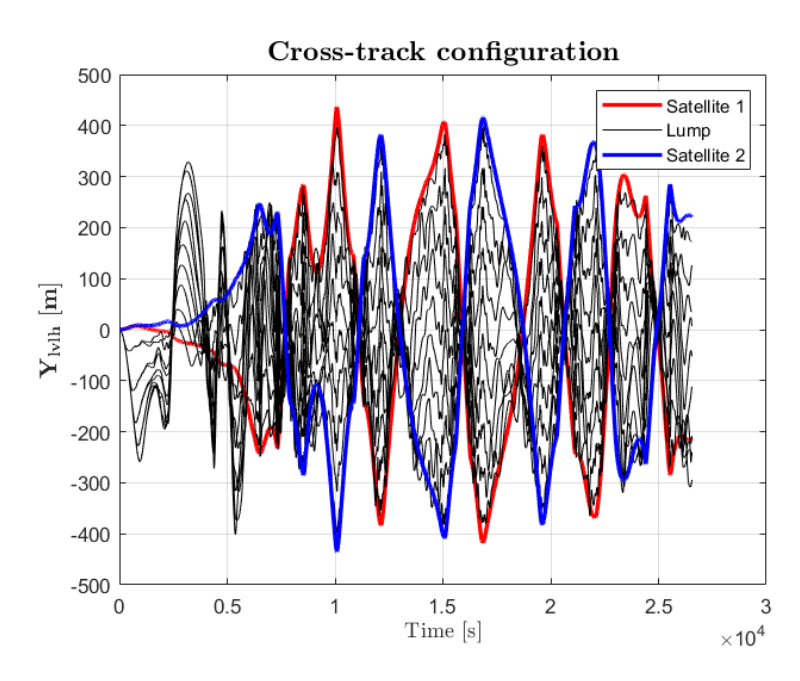


Figure 5.14: Cross-track configuration: evolution of the y–coordinate $(\hat{\ell}_2)$ over 5 periods

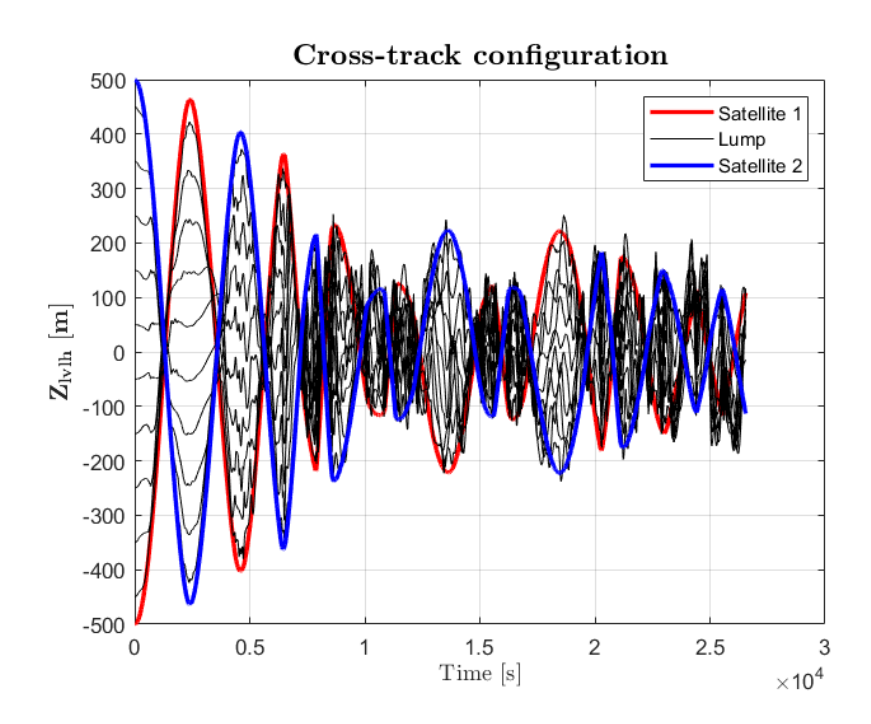


Figure 5.15: Cross-track configuration: evolution of the z–coordinate $(\hat{\ell}_3)$ over 5 periods

The cross-track configuration presents the greatest challenges and, at the same time, plays a central role in the application around which this thesis is developed. Recently, Aliberti [27]. conducted a study demonstrating the possibility of stabilizing the system in the cross-track configuration, primarily proposing two strategies. The first strategy relies on aerodynamic surfaces and takes advantage of residual atmospheric particles to generate lift, thereby maintaining the tether under tension. The second strategy, instead, is based on a Tethered Satellite System spinning around its center of mass, generating the necessary tension through the centrifugal force induced by the rotation.

Up to this point, a preliminary overview of the basic dynamics of the tethered satellite system under analysis has been provided. With the reference to the previously explored stabilization techniques for the desired final configuration also established, we can now turn our attention to the process that brings the system into its operational state: the deployment.

5.3 TSS free deployment analysis

Once the feasibility of maintaining a stable tether in the cross-track configuration has been confirmed, the next step is to identify the optimal strategy for transitioning from the packed configuration to the fully deployed cross-track configuration. In a preliminary analysis, all possible alternatives are considered, ranging from the most intuitive approach—deploying the tether directly along the cross-track direction—to more creative solutions, such as deploying along the radial or along-track directions followed by a specifically designed reconfiguration maneuver to bring the system from one of the aforementioned configurations to the target condition. Thus, in this section the general characteristics of deployment control within our model are presented, along with the first generic results illustrating the system's behavior during free propagation - in the absence of control forces - of the deployment along each of the three reference configurations.

Sections 3.3.1 and 3.4.1 provide information regarding the model used to represent the tether and how it is exploited in the study of deployment. First, it should be noted that this work does not consider the physical mechanism of deployment itself; rather, the focus is placed solely on the rate at which the tether is released. Additionally, as previously specified, it is assumed that in the initial packed configuration the tether is coiled equally between the two leader satellites of the formation. Consequently, the transition to the fully deployed configuration occurs by progressively increasing the portion of tether exposed until the entire available length is released. In this model - based on the approach proposed by Quadrelli [45]- this process is implemented by assigning time-varying profiles to the coordinates s_A and s_B . Let us recall that s_A and s_B are the material coordinates identifying the positions of the leader satellites along the tether, and indirectly represent the portions of tether coiled within these satellites.

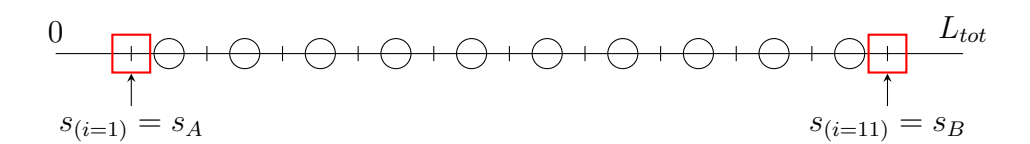


Figure 5.16: TSS modeling at a generic instant

Imposing a time-varying law on these coordinates thus constitutes the actual implementation of a deployment law, which quantifies the rate at which the tether is released and the speed at which the deployed portion of the tether increases.

Specifically, the preliminary deployment law used in the initial simulations of the system's deployment is presented below [16].

$$\dot{s}_A(t) = -0.0643 \quad [\text{m/s}] \tag{5.3}$$

$$\dot{s}_B(t) = +0.0643 \quad [\text{m/s}]$$
 (5.4)

$$\dot{l}(t) = \dot{s}_B(t) - \dot{s}_A(t) \tag{5.5}$$

The deployment rate was set according to a linear deployment law, in which the release speed gradually decreases as the tether is progressively deployed. The following presents the satellites material coordinates profile along with the evolution of the tether's deployed length.

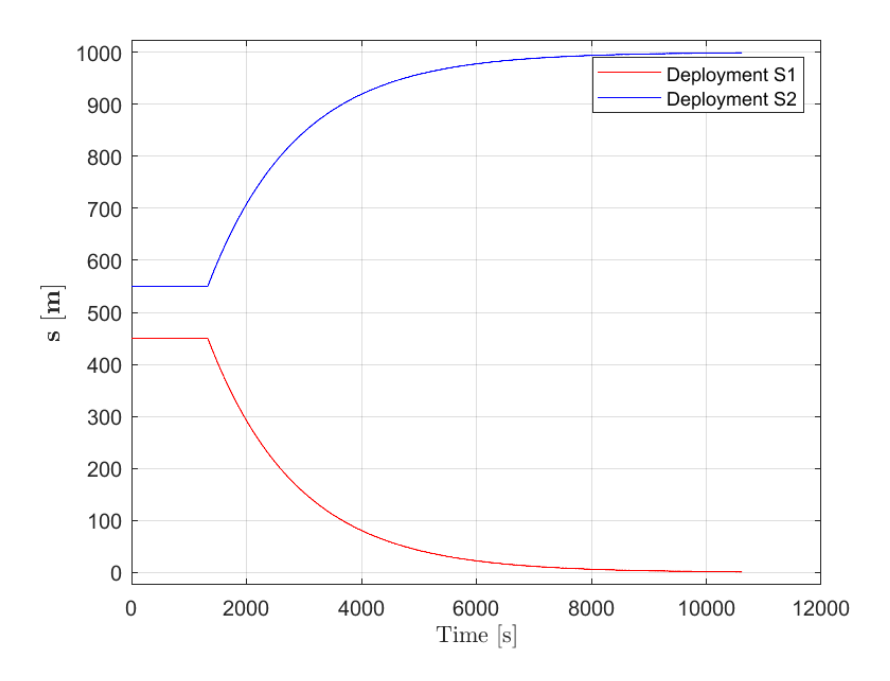


Figure 5.17: Time evolution of the material coordinates describing the position of the satellites along the tether

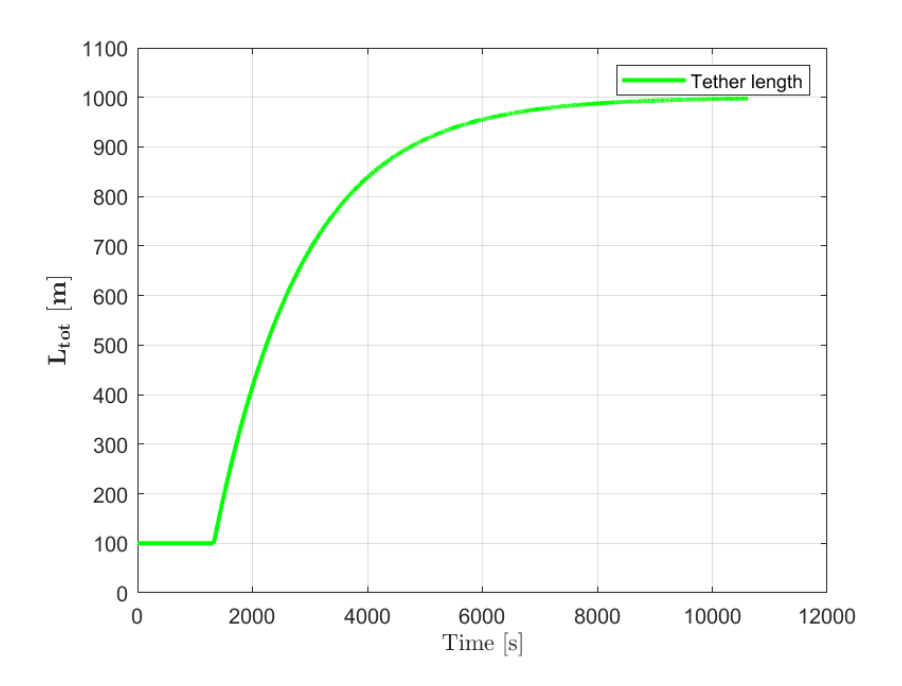


Figure 5.18: Time evolution of the tether length

According to the deployment law just presented, the following subsections aim to provide the reader with an understanding of the TSS behavior during the deployment in the three configurations previously introduced. Before proceeding, it should be noted that the deployment evolution is studied starting from a condition in which the tether is already partially deployed. Specifically, the initial conditions from which the simulations begin are as follows:

	Values
Initial tether length	100 [m]
Final tether length	1000 [m]
Tether deployment rate	0.1286 [m/s]

Table 5.8: Deployment's initial and target conditions

5.3.1 Radial Configuration

Let us begin with the radial configuration. The plots are presented below.

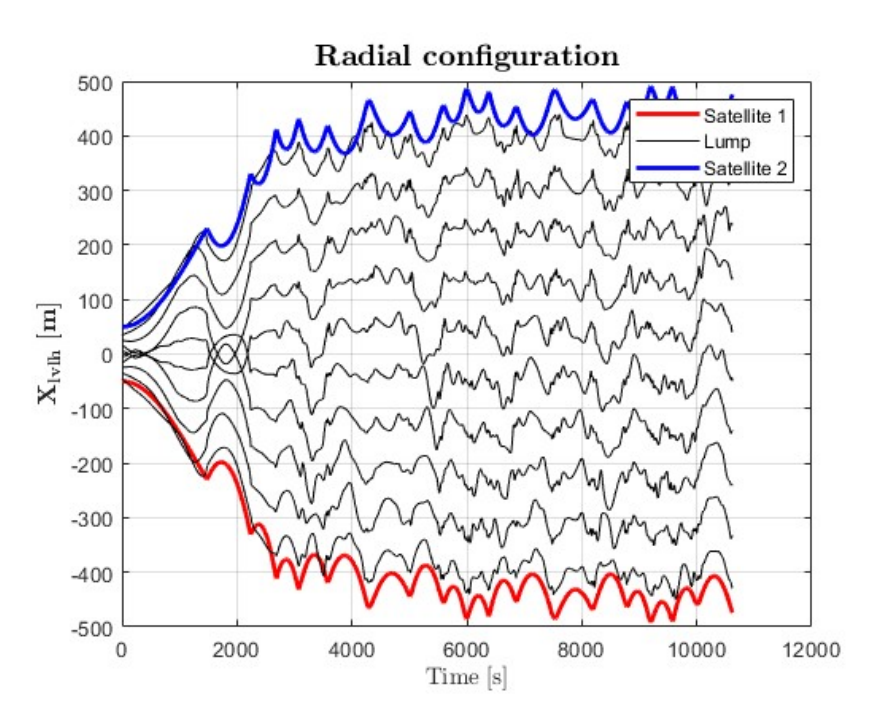


Figure 5.19: Radial configuration: evolution of the x–coordinate $(\hat{\boldsymbol{\ell}}_1)$

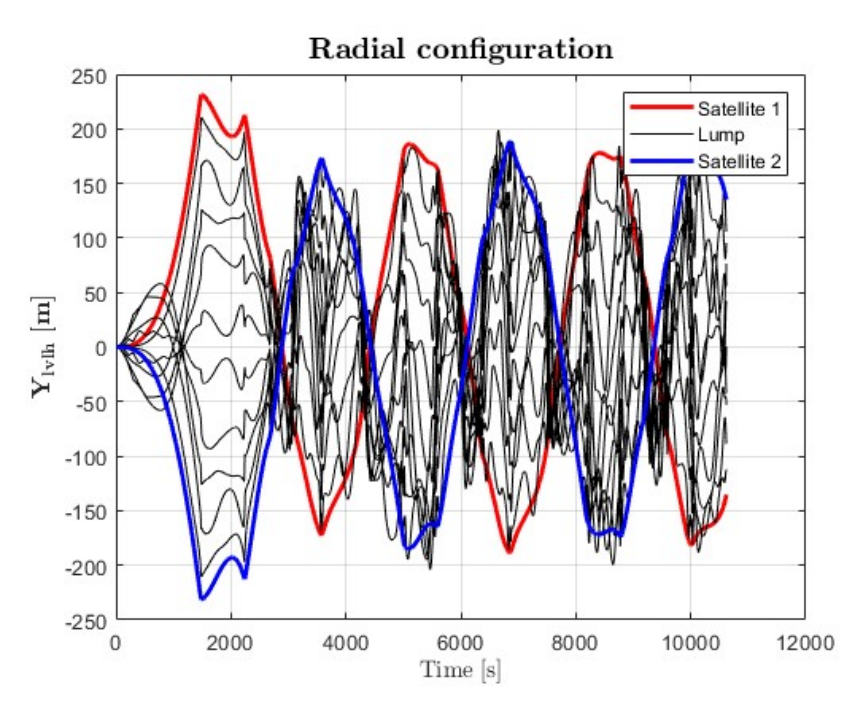


Figure 5.20: Radial configuration: evolution of the y-coordinate $(\hat{\ell}_2)$

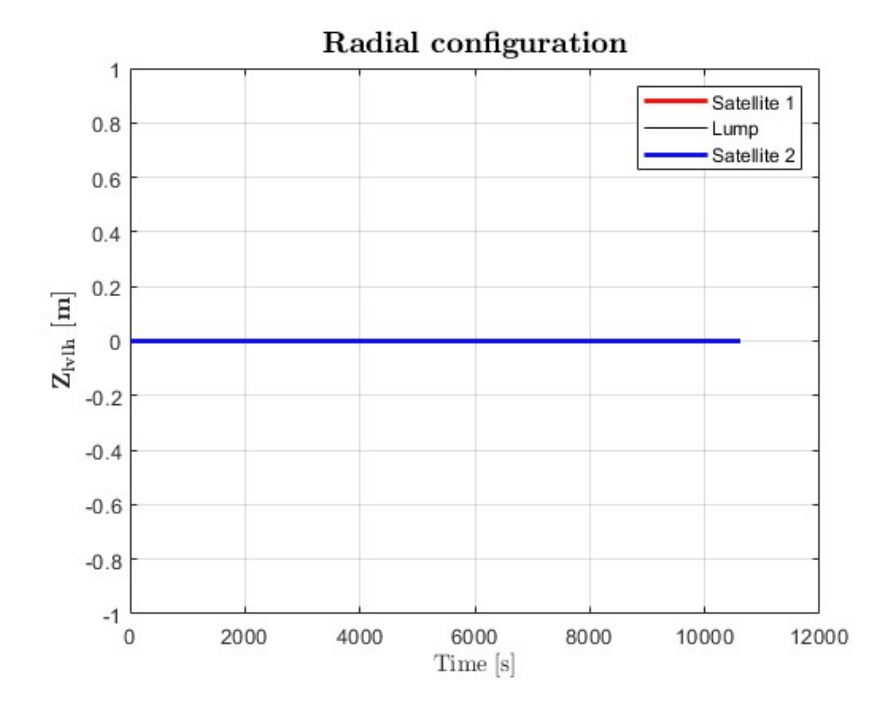


Figure 5.21: Radial configuration: evolution of the z-coordinate $(\hat{\ell}_3)$

The dynamics have been simulated over two orbital periods. In the case of the radial configuration, the results show an interesting tendency of the system to progress toward a complete tether deployment, mainly favored by the gravitational gradient effect. This can be regarded as a positive feature compared to the other configurations. At the same time, however, the system displays a very high level of instability, manifested on one side by strong oscillations along $\hat{\ell}_1$ (x_L) the axis, and on the other by a progressive loss of stability along the $\hat{\ell}_2$ (y_L) direction.

5.3.2 Along-track Configuration

The evolution of the dynamics of the masses during the deployment in the along-track direction is reported in Figures 5.22, 5.23 and 5.24.

As can be observed from these results, the imposition of a control law on the tether release velocity once again ensures that the tether length increases successfully. However, in addition to the slower rate at which full deployment is achieved, the system also falls into the same oscillatory motion around the $\hat{\ell}_3$ (z_L) axis that characterizes the along-track configuration discussed in 5.2.2. This confirms, once more, that such oscillations represent the key effect to be overcome in order to stabilize the system under these conditions

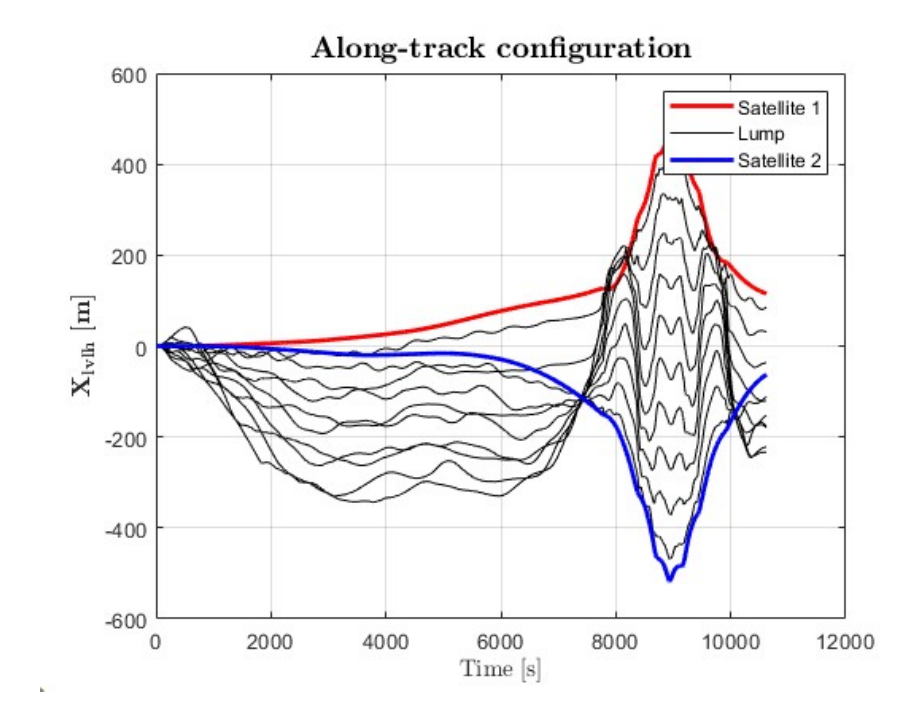


Figure 5.22: Along-track configuration: evolution of the x-coordinate $(\hat{\ell}_1)$

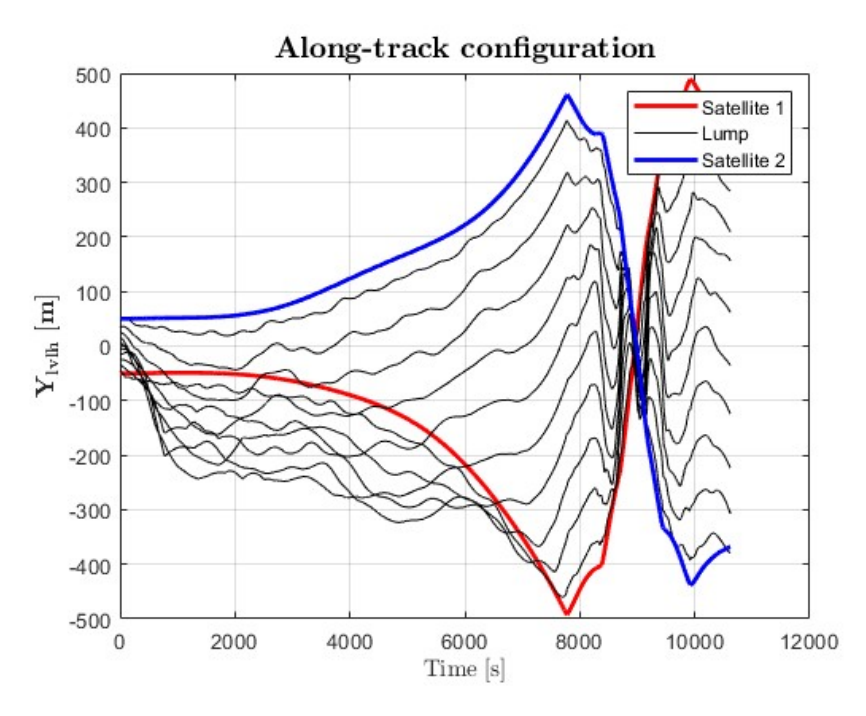


Figure 5.23: Along-track configuration: evolution of the y-coordinate $(\hat{\ell}_2)$

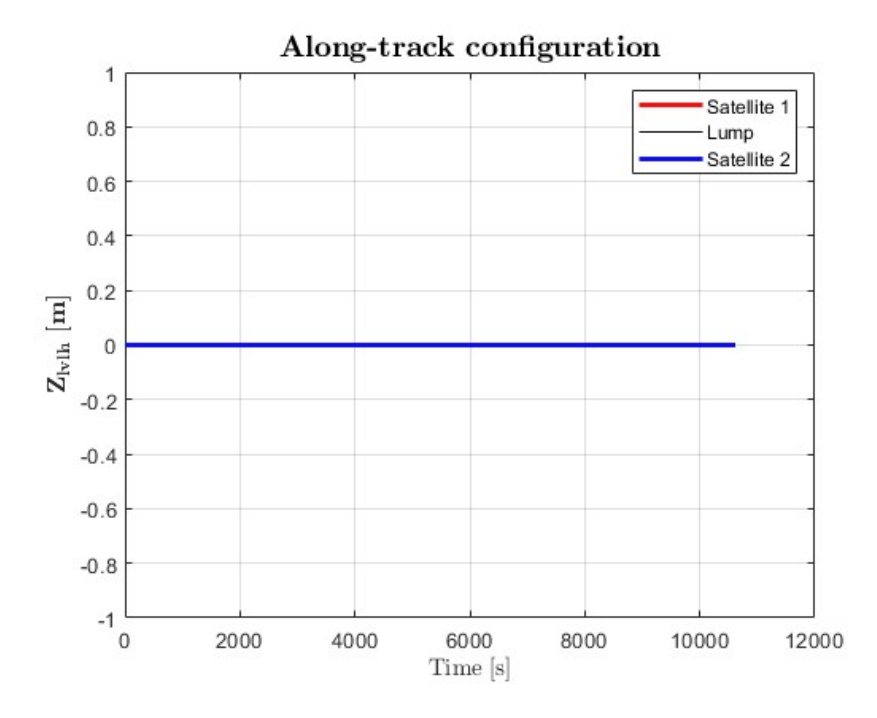


Figure 5.24: Along-track configuration: evolution of the z-coordinate $(\hat{\ell}_3)$

5.3.3 Cross-track Configuration

Finally the post-processing of the simulation data of the cross-track deployment gives the results reported in Figures 5.25, 5.26 and 5.27.

In the case of the cross-track configuration, the behavior of the system proves to be completely unstable. The imposed deployment law does not succeed in driving the tether toward the desired opening; instead, the system continuously collapses onto itself, preventing any effective extension. This outcome highlights how, under such an arrangement, the tethered system cannot sustain deployment and remains trapped in a persistently unstable regime. It is precisely this obstacle that becomes the essential challenge to address, since the initial application that motivated this work relies on the feasibility of reaching and then operating the system in the cross-track configuration. Therefore, the next chapter will focus on this issue, aiming to identify possible strategies to achieve the final state and to determine the control action required.

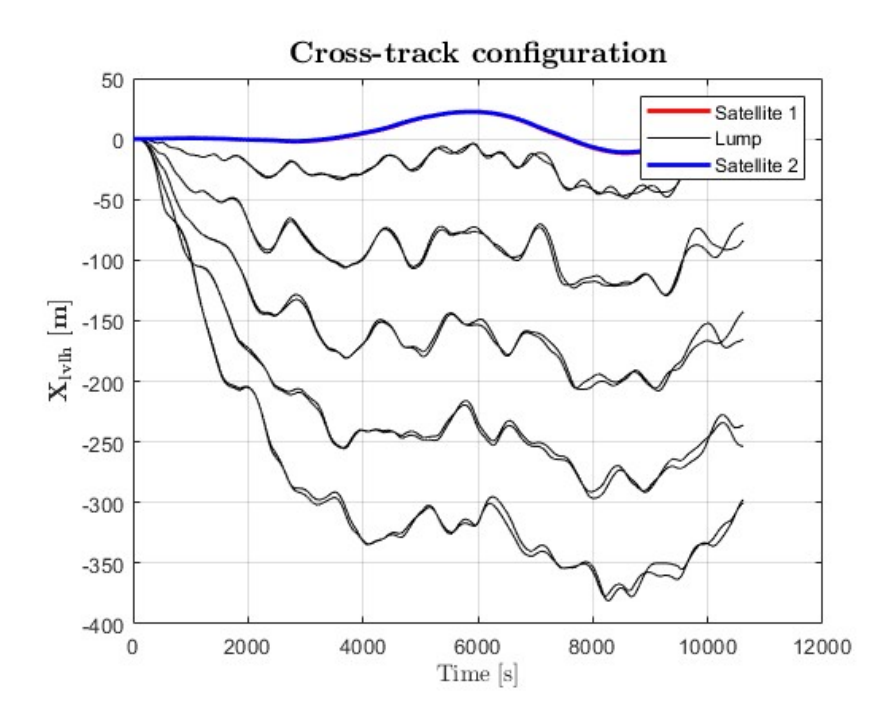


Figure 5.25: Cross-track configuration: evolution of the x-coordinate $(\hat{\ell}_1)$

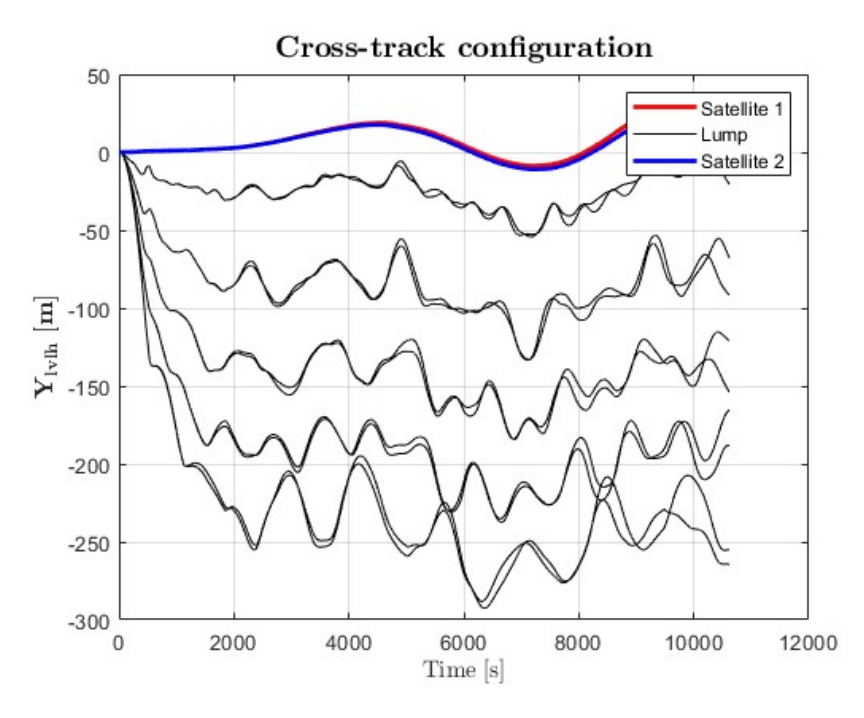


Figure 5.26: Cross-track configuration: evolution of the y-coordinate $(\hat{\ell}_2)$

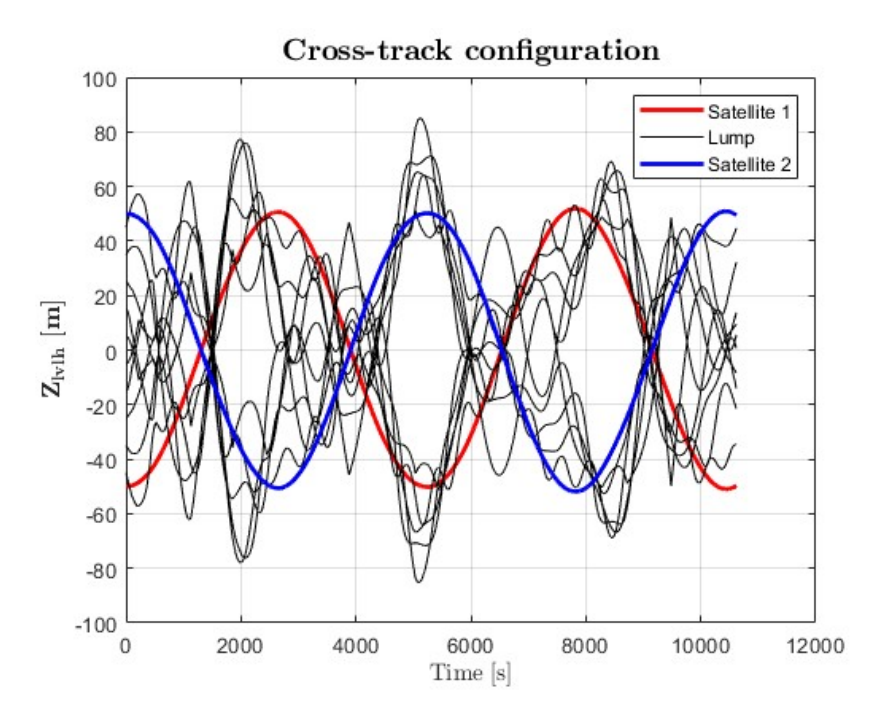


Figure 5.27: Cross-track configuration: evolution of the z–coordinate $(\hat{\ell}_3)$

Chapter 6

Deployment Strategies

The deployment phase - representing both the indispensable initial stage of the mission and the principal focus of the present study - is widely recognized as one of the most critical stages in tether-based missions. As reported in the first chapter, a considerable number of missions have failed due to incomplete or unsuccessful deployment of the tether; among these, NASA's Tethered Satellite System (TSS-1) has been presented as one of the first remarkable cases [32]. Given this central importance, the topic has drawn considerable attention from researchers, prompting numerous investigations aimed at identifying effective strategies to mitigate instabilities and ensure the stabilization of the Tethered Satellite System [48].

The present chapter builds on this research need by focusing on the specific challenge at hand: the attainment of the final desired configuration, namely a fully deployed system that maintains dynamic stability in the cross-track orientation. To this end, a range of deployment strategies is explored, with each approach evaluated in terms of the stability it provides and the resource requirements - the required acceleration and therefore the propellant mass necessary for execution. Given the complexity and computational demand of the lumped-masses model, it has been decided to employ the dumbbell model as a more straightforward tool to implement and test control laws. This choice allows for a faster implementation of the proposed strategies, significantly reducing the effort required to analyze the possible solutions. The loop is closed by extracting the control accelerations obtained from these tests and applying them to the lumped-masses model, which is retained in its role as the high-fidelity representation of the system, allowing for a verification of the consistency with a more realistic description of the TSS.

6.1 Deployment Strategies

The first intuitive approach would be to start the deployment along the cross-track direction, once orbital insertion has been completed. However, this is not the only feasible path. As previously noted, the cross-track configuration is intrinsically unstable, and it may therefore be of interest to exploit the contribution of the gravitational gradient to perform a radial deployment at a reduced cost. Once the desired final length has been reached, a subsequent maneuver can be carried out to shift the tether from the radial to the cross-track orientation. A similar approach may also be adopted using the along-track configuration as an intermediate step: the system is first deployed in the along-track direction and then reoriented to achieve the final cross-track configuration.

These three approaches therefore represent the principal strategies identified for reaching the desired state. For each strategy a PID (Proportional-Integral-Derivative) controller has been employed, chosen for its simplicity and the availability of benchmark results in the literature. This choice is considered sufficient for the purposes of this study, as the main goal is to preliminarily assess the behavior of each deployment strategy within the discrete model.

6.2 Proportional-Integral-Derivative Control

The Proportional-Integral-Derivative (PID) feedback control mechanism is widely used primarily thanks to its ease of implementation and low computational cost; these features make it particularly attractive in contexts where resources are limited and simplicity is preferred. An additional advantage lies in the availability of numerous tuning rules - both analytical and heuristic - that allow the controller parameters to be adjusted without the explicit need for the mathematical model of the system under consideration. Nevertheless, the simplicity that makes the PID controller attractive also comes with drawbacks such as the lack of robustness against variations in system parameters and initial conditions, and the potential difficulty of selecting appropriate control gains. In particular, the tuning process can be non-trivial, especially when the designer has limited prior experience with the dynamics of the controlled system. These limitations underscore the fact that, although the PID controller is a versatile and effective tool, its performance may be significantly affected in scenarios where the system exhibits strong uncertainties or rapid parameter changes.

The standard structure of this controller can be represented as follows:

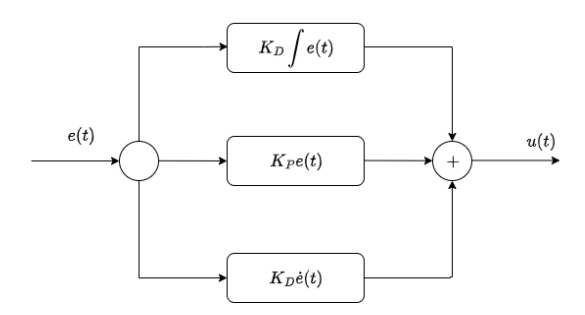


Figure 6.1: Conceptual scheme of the PID controller

The control law is fundamentally based on the computation of the error signal, defined as the difference between the desired and the actual state. The proportional term generates a control action directly proportional to this error, thereby providing an immediate corrective response to deviations from the desired trajectory. To enhance the accuracy and effectiveness of the control, two additional contributions are introduced. The integral term accounts for the cumulative history of the error, enabling the controller to eliminate steady-state offsets and improve long-term accuracy. Conversely, the derivative term anticipates the future trend of the error by responding to its rate of change, thereby contributing to the damping of oscillations and enhancing system stability.

6.2.1 Implementation within the reference model

In this preliminary analysis, where the rod model has been employed, the state of the system is fully captured by three variables: the in-plane angle, the out-of-plane angle, and the tether length. Within this framework, therefore, the study of the evolution of these parameters is sufficient to fully characterize the dynamics of the TSS within this framework. As for the implementation of the deployment, it is enough to prescribe the desired law in terms of \dot{l} , which governs the rate of change of the tether length. Beyond the progressive increase in tether length, the system's behavior is interpreted with respect to the evolution of the in-plane and out-of-plane angles.

As a brief digression, aimed at providing a clearer contextualization and facilitating the understanding of the comparison between the two models, we report here the case of the radial configuration, whose plots were presented in Section 5.3.1. In this scenario, it is possible to confirm that the dynamics are characterized by an in-plane angle that remains essentially constant at zero, together with an out-of-plane angle steadily equal to zero, as illustrated in the figure below. Drawing a parallel with the analysis carried out using the lumped-masses model, this behavior is confirmed, except for small oscillations in the in-plane angle. These

deviations arise from the presence of perturbations, which are not accounted for in the case of the dumbbell model.

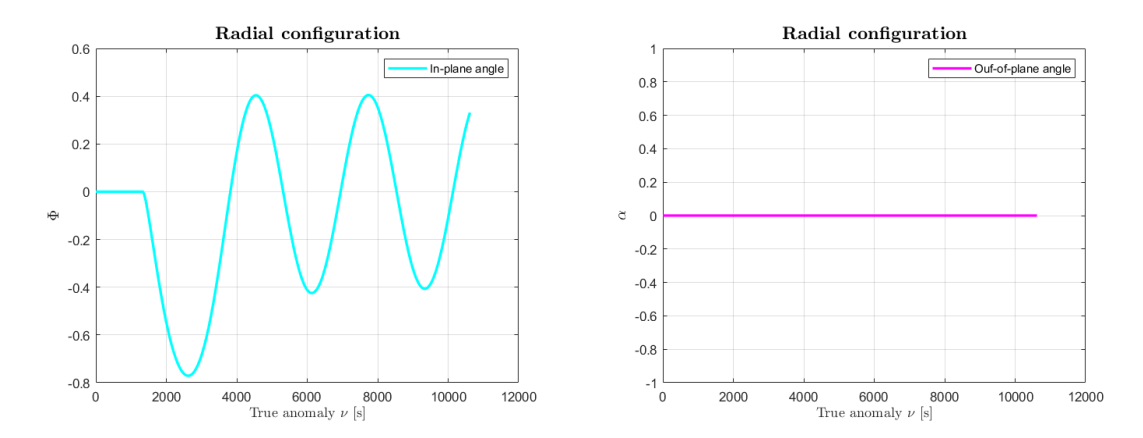


Figure 6.2: Rod model: In-plane and out-of-plane angle

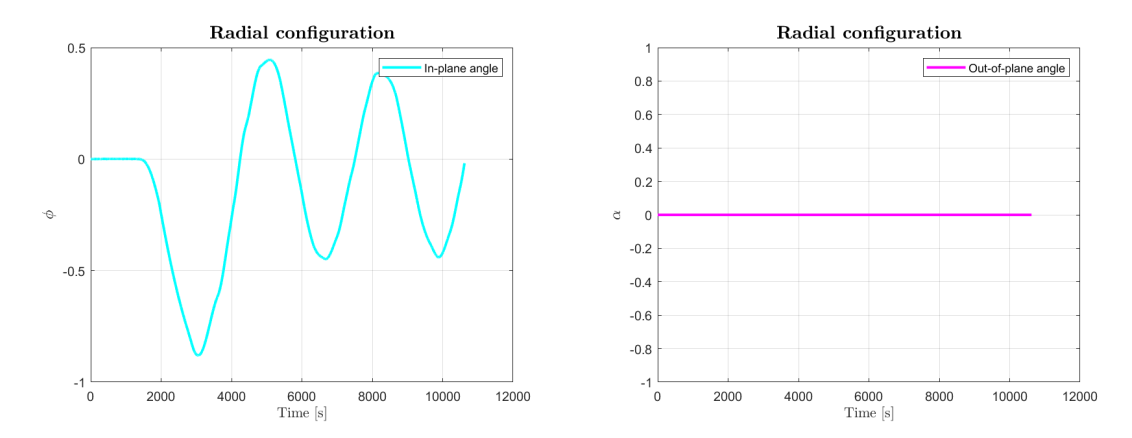


Figure 6.3: Discrete model: In-plane and out-of-plane angle

This behavior is also confirmed in the case of the along-track configuration. In contrast, for the cross-track configuration, in addition to the oscillations of the in-plane angle, significant oscillations of the out-of-plane angle are observed, consistently with the findings discussed in the previous sections regarding the inherent instability of the TSS in this latter configuration.

Building upon the discussion above, the need for an active control on the two characteristic angles - aimed at suppressing oscillations and maintaining each configuration in its nominal orientation - can be addressed by introducing suitable control torques. In this model, two control terms are therefore introduced, acting respectively in the equations of the second and fourth state variables of the ODE system presented at the end of Section 3.5. By employing a PID controller, and

considering that the variables to be controlled are the two angular coordinates, the control action is represented by two torques computed as follows:

$$u_{\phi} = K_P e_{\phi} + K_D \dot{e}_{\phi} + K_I \int e_{\phi} dt \tag{6.1}$$

$$u_{\alpha} = K_P e_{\alpha} + K_D \dot{e}_{\alpha} + K_I \int e_{\alpha} dt \tag{6.2}$$

 u_{ϕ} and u_{α} are torques acting along axes parallel to $\hat{\boldsymbol{\ell}}_1$ and $\hat{\boldsymbol{\ell}}_3$, respectively.

6.3 Radial PID controlled deployment

Let us now consider what appears to be the simplest and most stable deployment configuration, the one in which the system, due to its intrinsic characteristics, naturally exhibits a more stable behavior: the radial configuration. This is also the configuration that has received the greatest attention in the literature to date, making it easier to find comparable results for validation. In our analysis, relying on the simplified rod model, the control gains are defined as follows:

$$K_P = 2.5 K_D = 3 K_I = 0 (6.3)$$

The choice of the initial gain values has been performed according to what has been previously explored in the literature concerning the studies about the dumbbell model of the Tethered Satellite System. Building upon these established references, minor adjustments were introduced to tune the controller's response and achieve the most favorable system behavior within the framework of the present analysis.

The time evolution of the system's characteristic coordinates in this case is shown in the following figures:

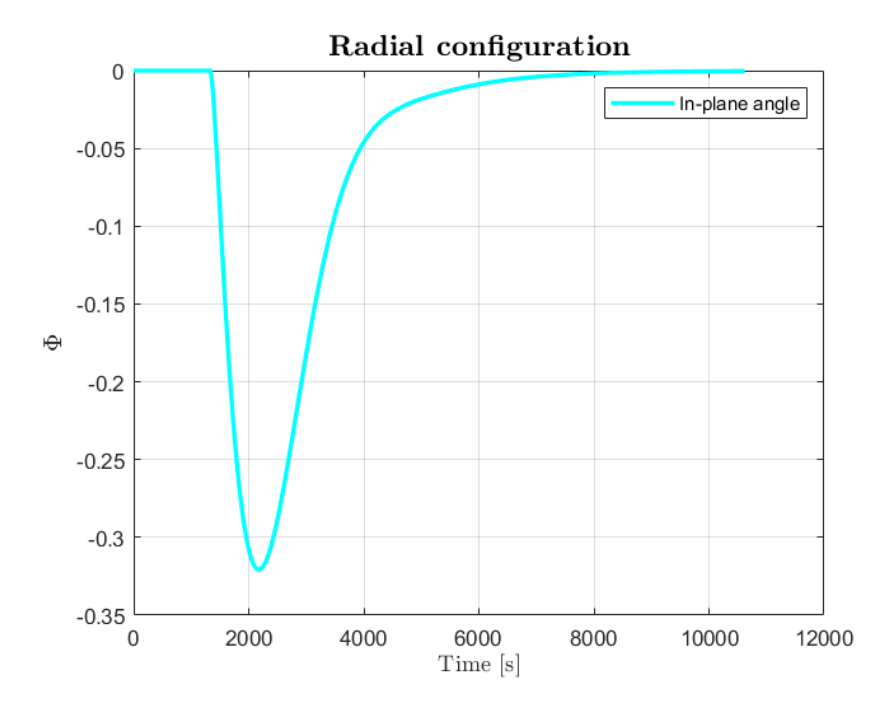


Figure 6.4: Radial configuration: time evolution of the in-plane angle

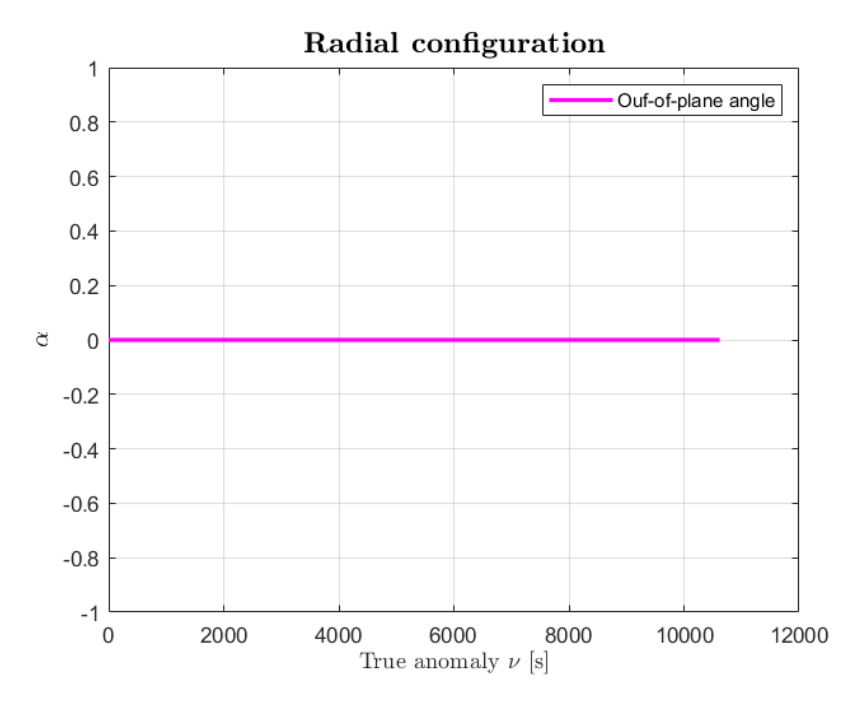


Figure 6.5: Radial configuration: time evolution of the out-of-plane angle

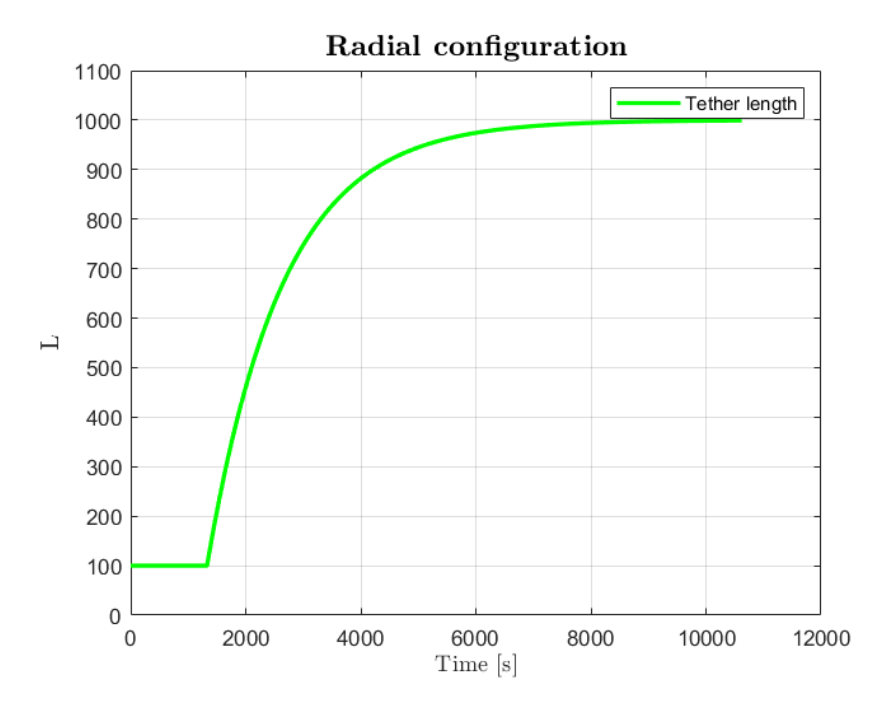


Figure 6.6: Radial configuration: time evolution of the tether length

Below are shown the time evolution of the control torques that ensure the system's stability in the case of the PID controller.

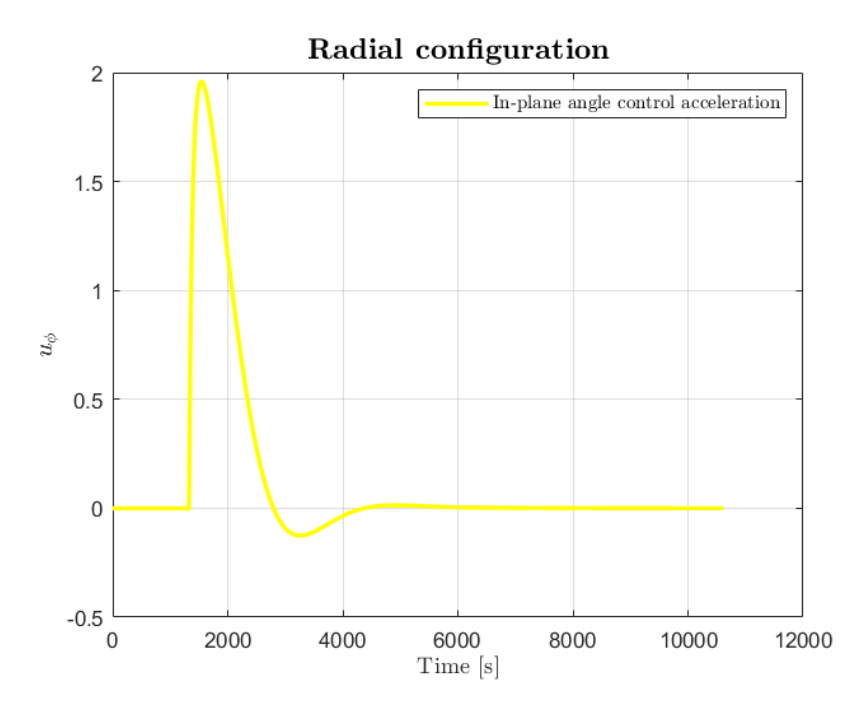


Figure 6.7: Radial configuration: in-plane control torque

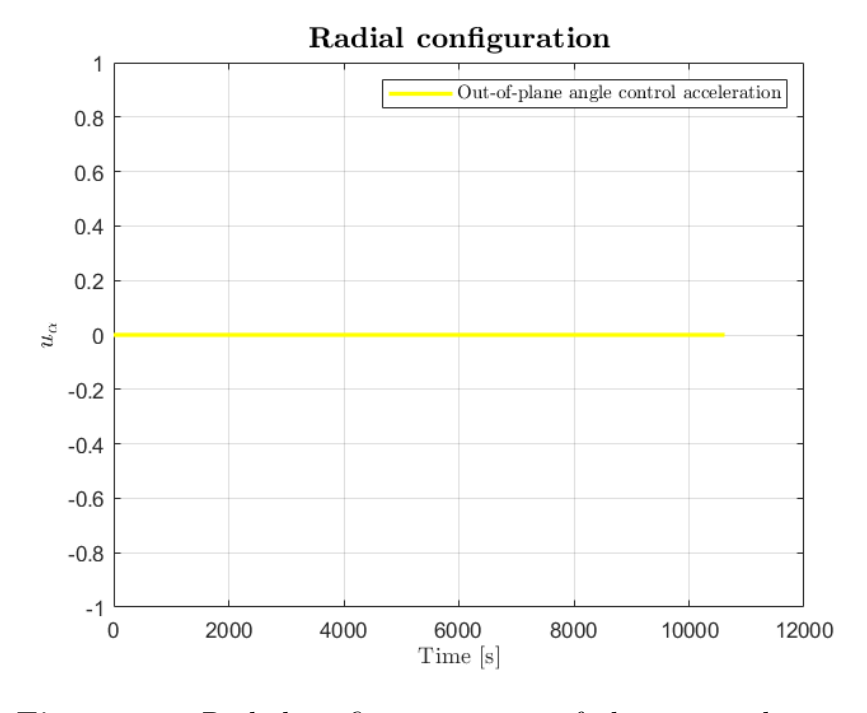


Figure 6.8: Radial configuration: out-of-plane control torque

6.3.1 Validation on the discrete model: Radial Configuration case

In line with what was anticipated in both the introduction of this thesis and the introduction of the present chapter, the final step consists of extracting the control acceleration obtained from this simulation phase to verify its validity by applying it to a more faithful representation of the system, namely the discrete model. Keeping in mind that the motivation for using the dumbbell model as a preliminary analysis tool stems from the difficulty of implementing active control directly within the simulation environment of the discrete model, as well as the associated computational cost, a mean value of the control acceleration is extracted from the results presented above and applied in the discrete model simulations as a constant control input.

First of all, it must be clarified that the control quantity obtained as output from the dumbbell model simulations corresponds to a generalized torque. According to the derivation presented in Section 3.5 and the definition of generalized forces in this context, the following relation holds:

$$Q = \tau \tag{6.4}$$

where Q represents the generalized torque derived from the simulations, and τ denotes the actual torque applied to the system. Starting from this point, by recalling the definition of torque generated by two opposing forces, it is possible to extract from the average control torque values reported in Figures 6.7 and 6.8 the equivalent control forces to be applied to the two leading satellites of the discrete model. These forces, in the present case, are defined as follows:

$$F_{contr,1} = \begin{bmatrix} -0.2\\0\\0 \end{bmatrix} [N] \qquad F_{contr,N_{tot}} = \begin{bmatrix} 0.2\\0\\0 \end{bmatrix} [N]$$
 (6.5)

By introducing these forces - after properly scaling them into accelerations - into the system of ODEs presented in Section 3.4.1, the dynamics obtained are illustrated in the following plots:

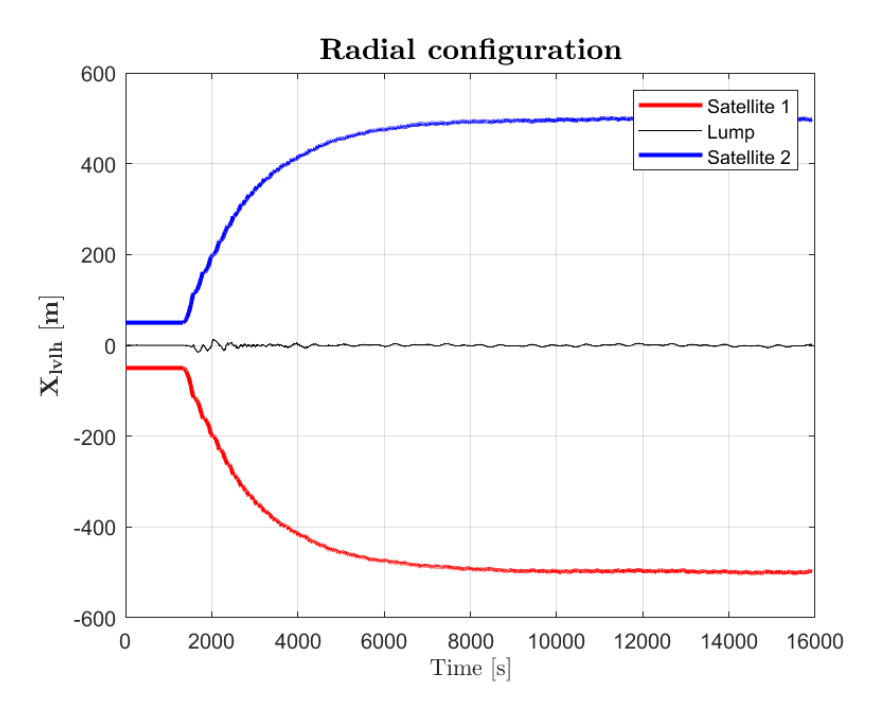


Figure 6.9: Controlled radial configuration: time evolution of the x-coordinate $\hat{\ell}_1$

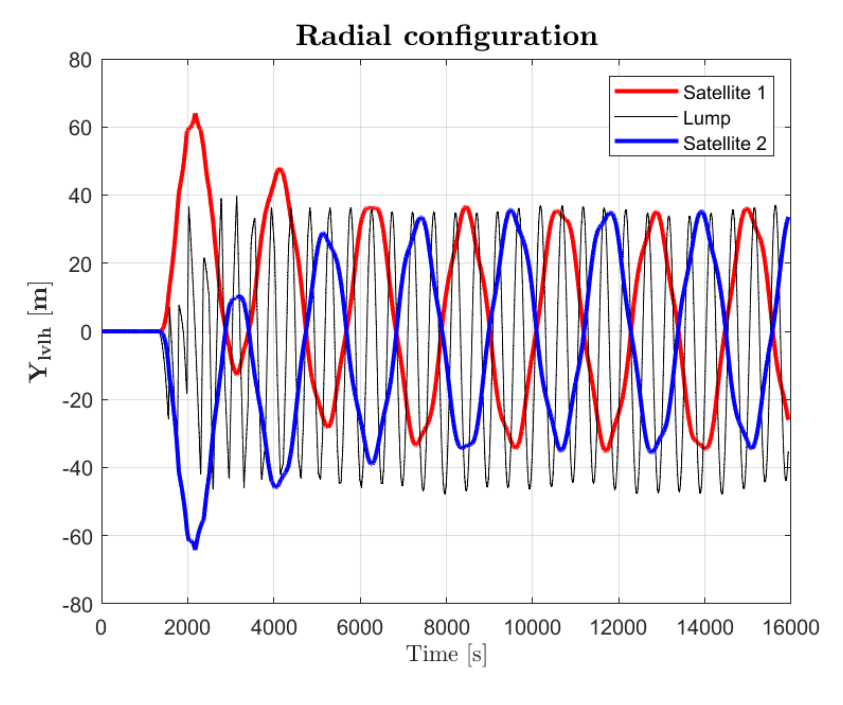


Figure 6.10: Controlled radial configuration: time evolution of the y-coordinate $\hat{\ell}_2$

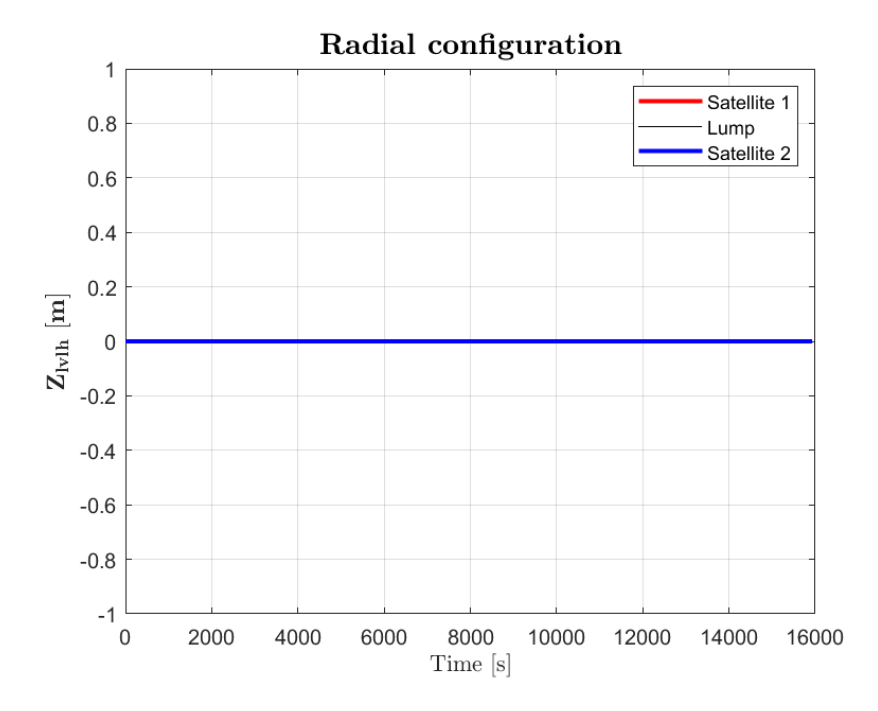


Figure 6.11: Controlled radial configuration: time evolution of the z-coordinate $\hat{\ell}_3$

As shown in the plots, the system assisted by the control forces is able to complete the deployment successfully and reach the desired final extension. However, it is evident that the constant, non-optimized magnitude of the applied control produces noticeable residual instabilities, particularly in the coordinate along the $\hat{\ell}_2$ axis. These oscillations indicate that a time-varying or better-tuned control profile would be required to suppress the remaining oscillations and improve post-deployment stability.

6.4 Along-track PID controlled deployment

In this section, we turn our attention to the alternative deployment on the along-track direction. The same procedure as in the previous section is followed, up to the point of evaluating the system behavior using the lumped-masses model. Relying once again on the simplified rod model, the control gains are defined as follows:

$$K_P = 5 K_D = 2.5 K_I = 0 (6.6)$$

The results obtained for the in-plane and out-of-plane angles are as follows:

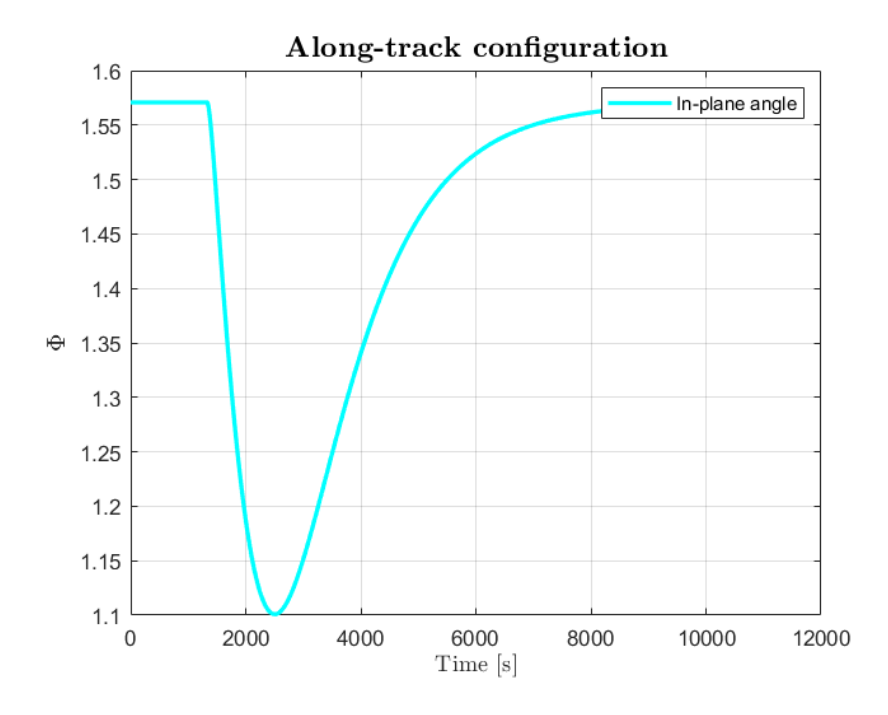


Figure 6.12: Along-track configuration: time evolution of the in-plane angle

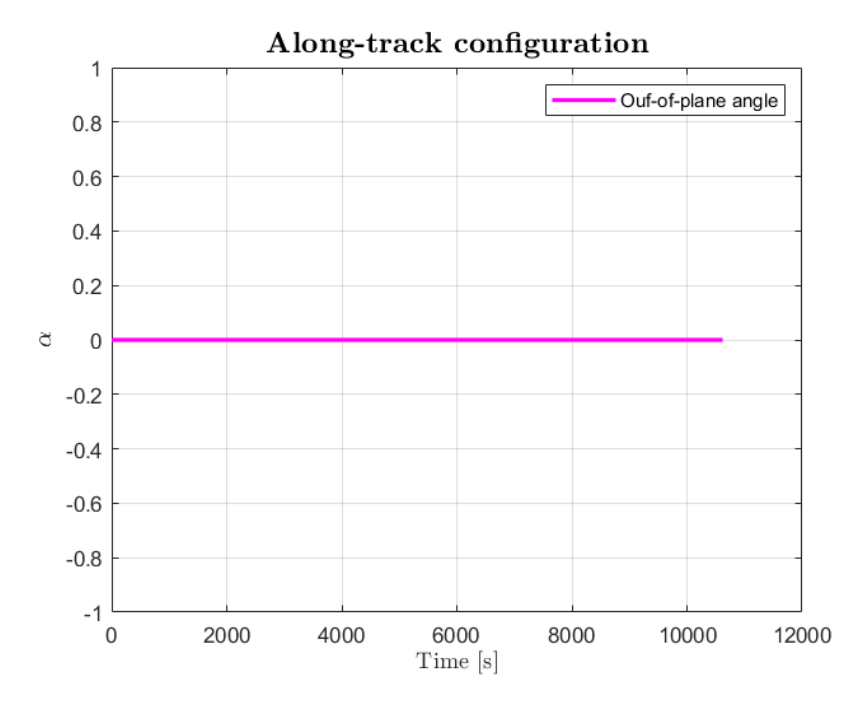


Figure 6.13: Along-track configuration: time evolution of the out-of-plane angle

The following shows the time history of the PID control torques maintaining the system stability.

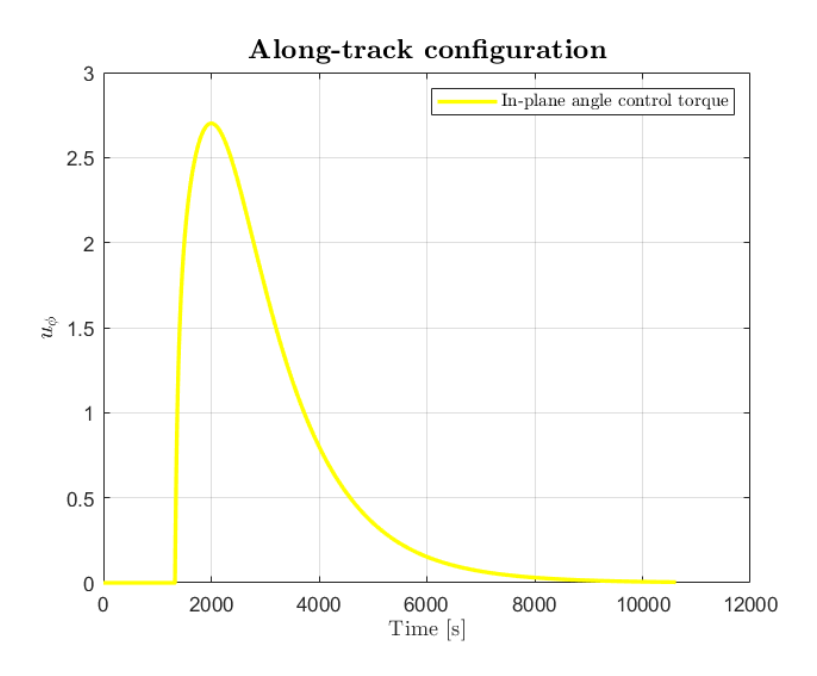


Figure 6.14: Along-track configuration: in-plane control torque

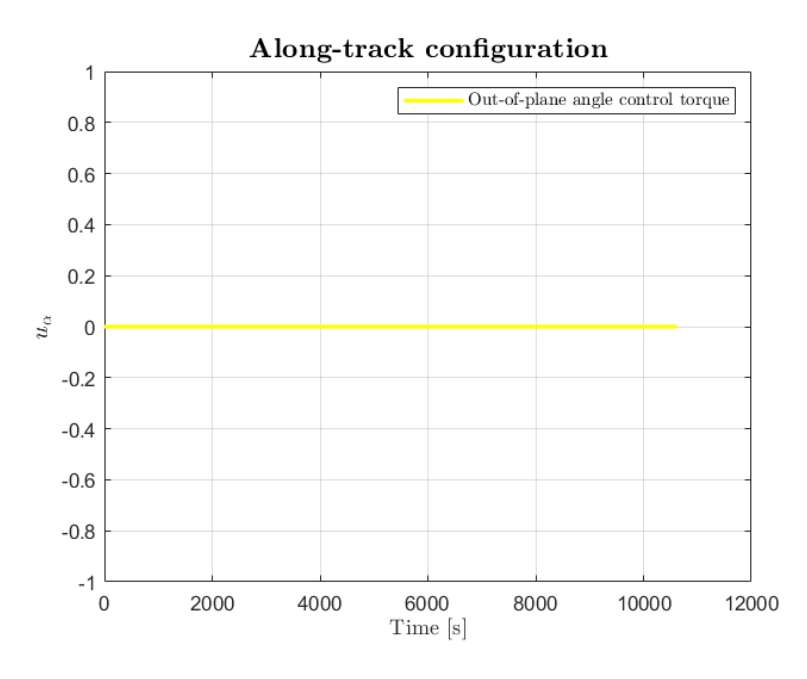


Figure 6.15: Along-track configuration: out-of-plane control torque

6.4.1 Validation on the discrete model: Along-track Configuration case

Following the same approach outlined for the radial configuration, the control accelerations derived from the simplified dumbbell model are applied to the discrete model to evaluate the system's behavior. The procedure remains unchanged: generalized torques obtained from the dumbbell simulations are converted into equivalent forces for the leading satellites and then introduced into the system of ODEs described in Section 3.4.1.

The control forces in this case are, therefore, defined as follows:

$$F_{contr,1} = \begin{bmatrix} 0 \\ -0.25 \\ 0 \end{bmatrix} [N] \qquad F_{contr,N_{tot}} = \begin{bmatrix} 0 \\ 0.25 \\ 0 \end{bmatrix} [N]$$
 (6.7)

The application of these control forces leads to the dynamics described by the following plots.

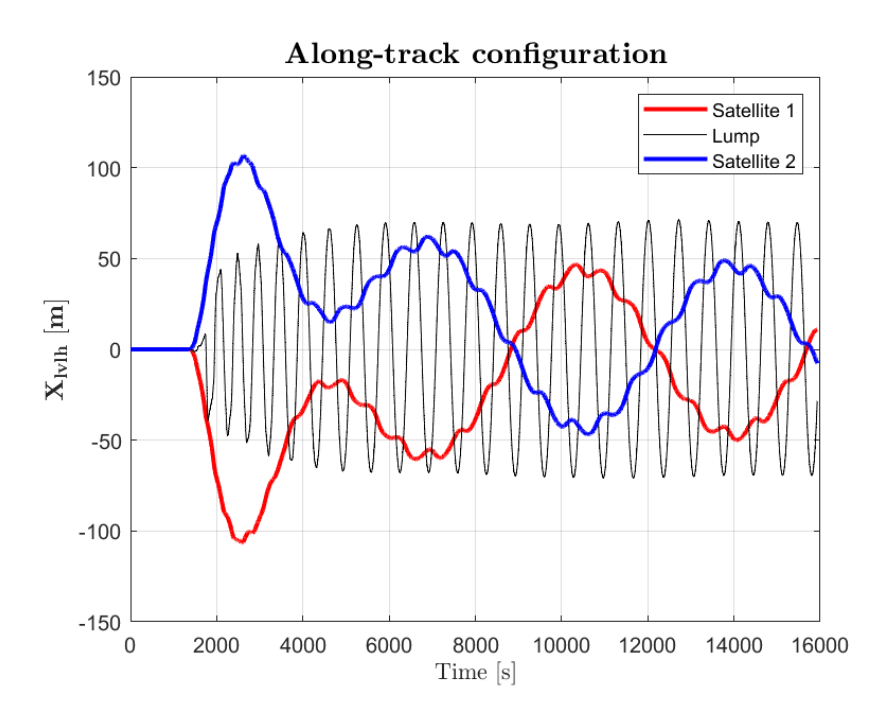


Figure 6.16: Controlled along-track configuration: time evolution of the x-coordinate $\hat{\ell}_1$

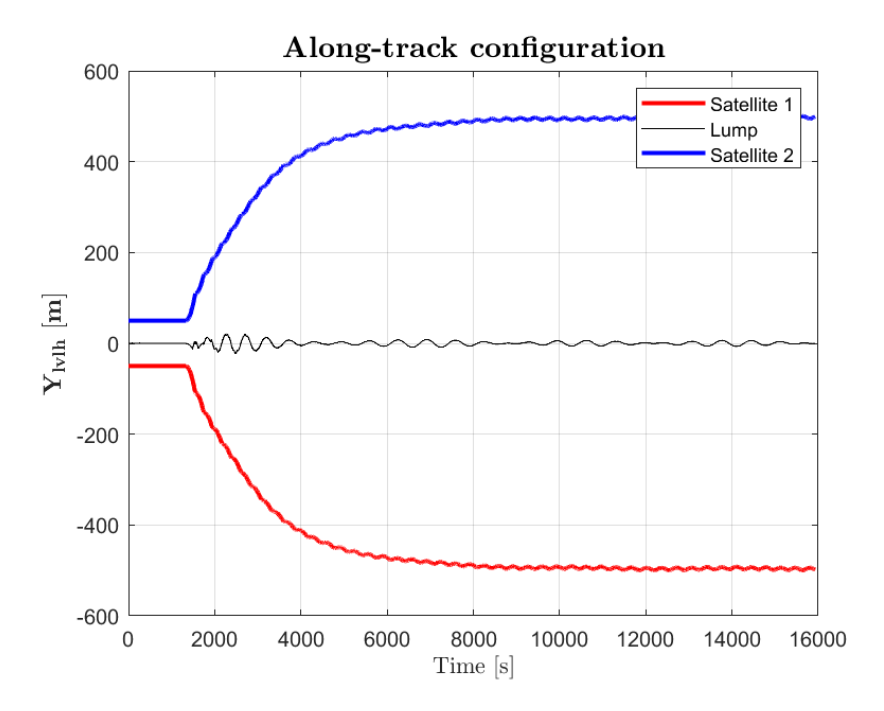


Figure 6.17: Controlled along-track configuration: time evolution of the y-coordinate $\hat{\ell}_2$

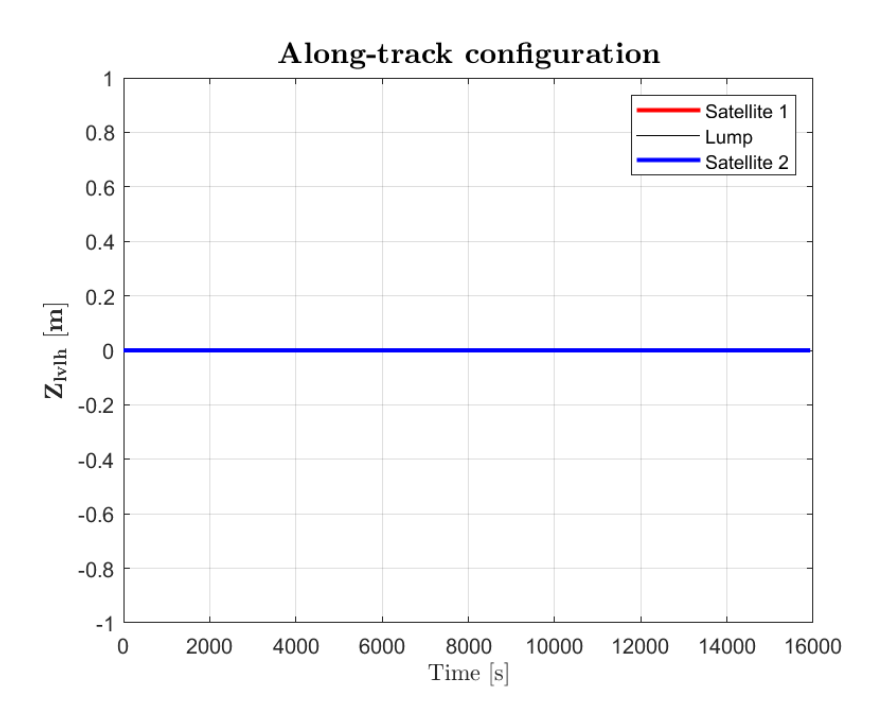


Figure 6.18: Controlled along-track configuration: time evolution of the z-coordinate $\hat{\ell}_3$

As the previous one, also this configuration is characterized by an essentially in-plane motion, which explains why the deployment success can be achieved with a control force very similar in magnitude to that used in the radial case. However, the same considerations discussed earlier still apply: the approximate nature of the control magnitude derived from the simplified model results in still noticeable oscillations - especially in the in-plane direction where no active control is applied. These oscillations represent a non-negligible source of instability, which could be effectively mitigated through the development of a more accurate control strategy.

6.5 Cross-track PID controlled deployment

Finally, we turn our attention to the cross-track configuration to assess the magnitude of control required to ensure system stability in this scenario. Differently, in this case the analysis begins from an initial condition in which the system is not already in the cross-track orientation, but rather lies approximately within the orbital plane. This approach is adopted for two main reasons. First, it allows us to evaluate the system starting from a less favorable state. Second, it provides a useful estimate of the control effort necessary to transition the system from one of the planar configurations - radial or along-track - to the out-of-plane cross-track configuration. This latter consideration is particularly relevant when evaluating the deployment maneuvers explored in Sections 6.3 and 6.4, given that the ultimate objective of this study is tied to an application requiring the system to operate in the cross-track configuration. As such, the analysis must account not only for the in-plane deployment but also for the additional control effort needed to achieve the desired out-of-plane orientation.

Returning now to the implementation of the control within the simulation environment of the dumbbell model, it should be noted that the cross-track configuration is characterized by significant oscillations, which involve also the out-of-plane angle. In this case, the need to stabilize the out-of-plane motion necessitates the introduction of a second control torque acting directly on the angle α . The control torques are once again computed according to Equations 6.1 and 6.2, while the control gains are defined as follows:

$$K_{P,\phi} = 3$$
 $K_{D,\phi} = 2.5$ $K_{I,\phi} = 1$ (6.8)

$$K_{P,\alpha} = 5$$
 $K_{D,\alpha} = 3$ $K_{I,\alpha} = 0$ (6.9)

Based on the control gains defined above, the system demonstrates a satisfactory dynamic response, as illustrated in the following figures, which show the time evolution of the in-plane and out-of-plane angles.

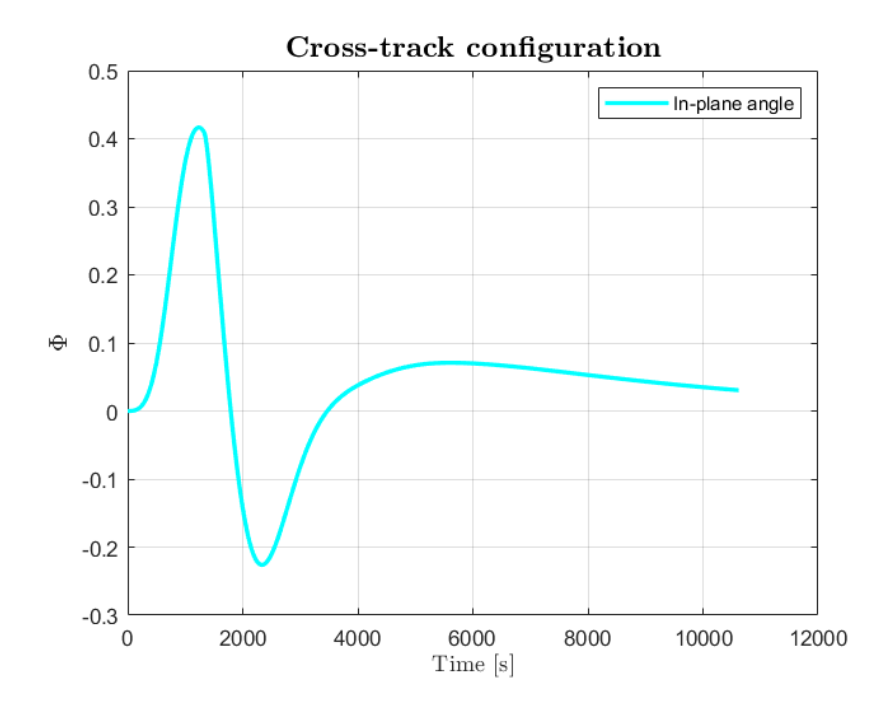


Figure 6.19: Cross-track configuration: time evolution of the in-plane angle

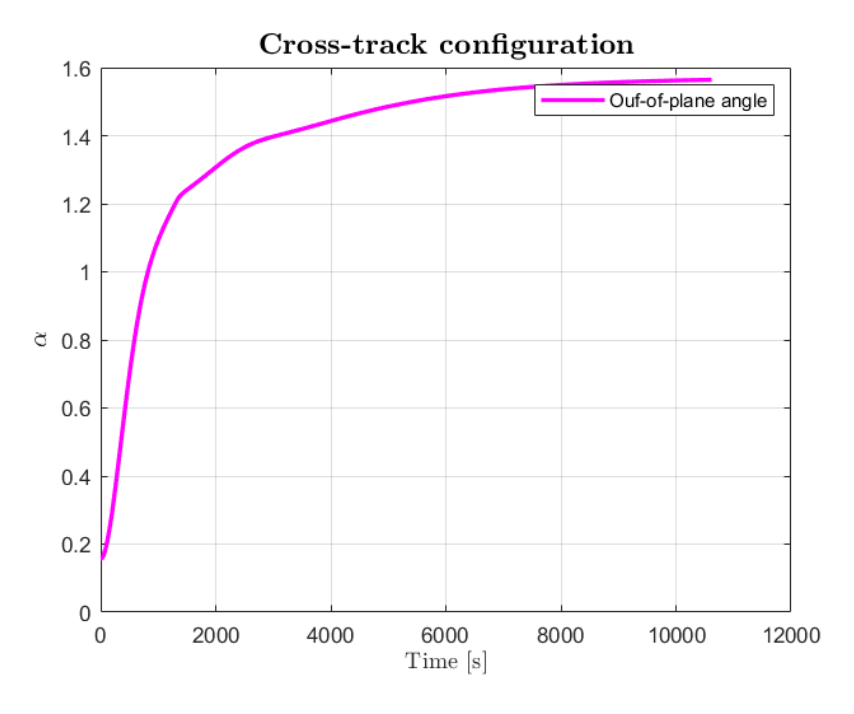


Figure 6.20: Cross-track configuration: time evolution of the out-of-plane angle

The time evolution of the PID control torques stabilizing the system is shown below.

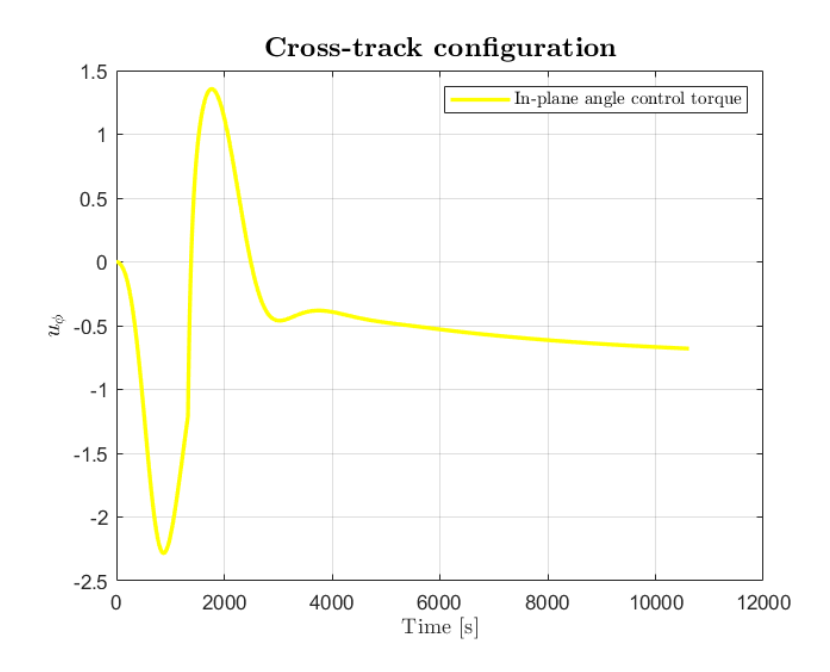


Figure 6.21: Cross-track configuration: in-plane control torque

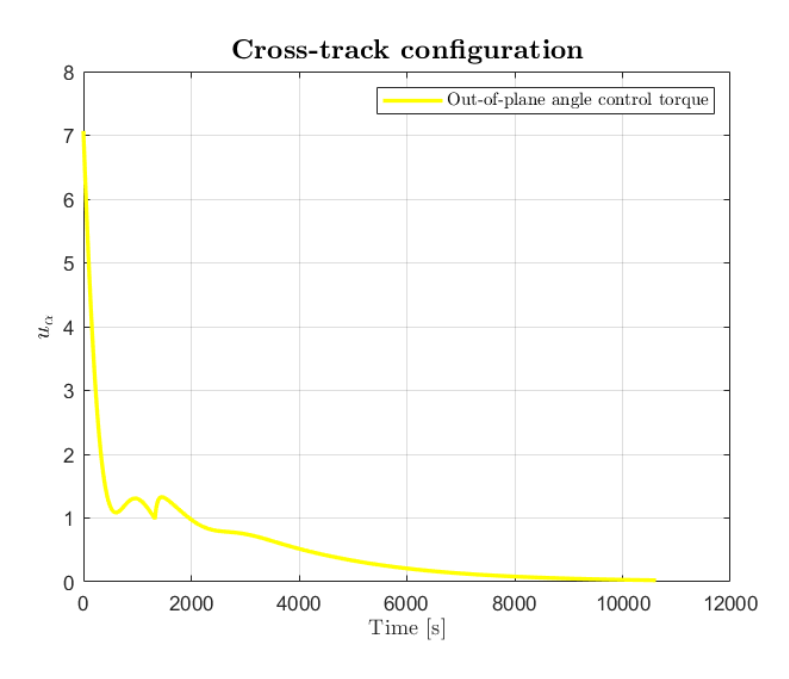


Figure 6.22: Cross-track configuration: out-of-plane control torque

6.5.1 Validation on the discrete model: Cross-track Configuration case

The last step, as done for the previous two configurations, is again verifying the results on the lumped-masses model. In this case the control action comprises two torques, and therefore two corresponding pairs of equal-magnitude and opposite-direction forces are applied to the leader satellites. One pair acts in-plane, while the other acts out-of-plane, parallel to the direction defined by $\hat{\ell}_3$.

$$F_{contr,1} = \begin{bmatrix} 0.05 \\ -0.05 \\ -0.45 \end{bmatrix} [N] \qquad F_{contr,N_{tot}} = \begin{bmatrix} -0.05 \\ 0.05 \\ 0.45 \end{bmatrix} [N]$$
 (6.10)

After scaling these forces to accelerations and inserting them into the lumpedmasses ODE system, the TSS response obtained is shown in the following plots.

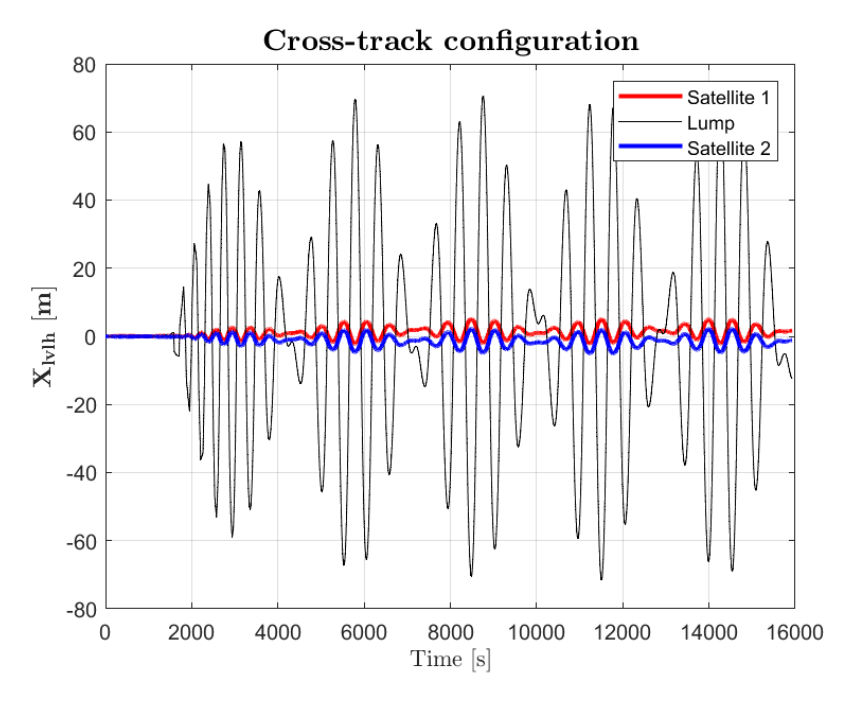


Figure 6.23: Controlled cross-track configuration: time evolution of the x-coordinate $\hat{\ell}_1$

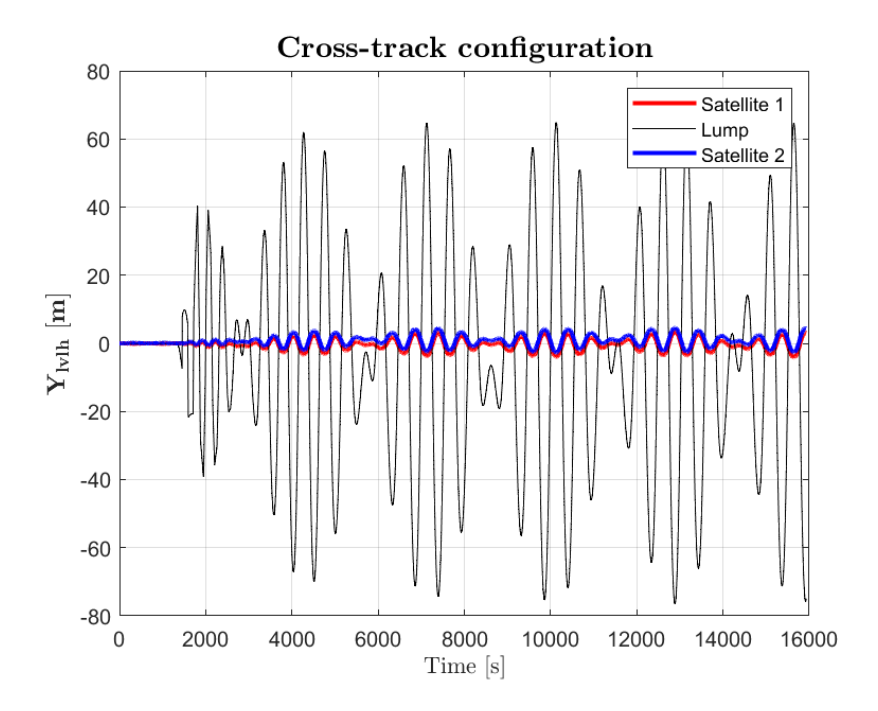


Figure 6.24: Controlled cross-track configuration: time evolution of the y-coordinate $\hat{\ell}_2$

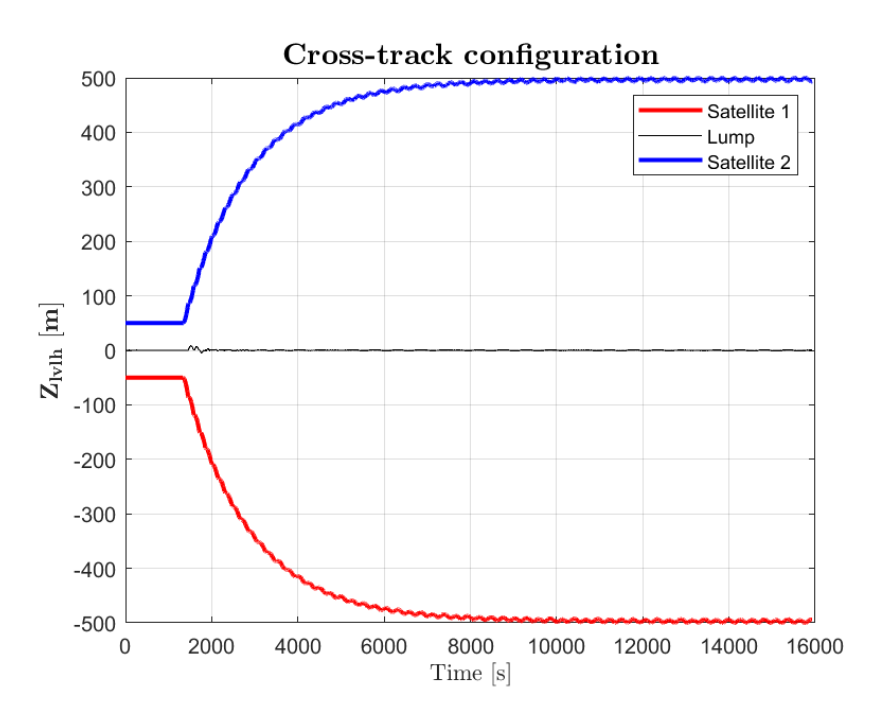


Figure 6.25: Controlled cross-track configuration: time evolution of the z-coordinate $\hat{\ell}_3$

In this set of simulations, as well as in the previous cases, the achievement of the desired final deployed length can be considered satisfactory. However, it should be noted that, similarly to the other two configurations, the system still experiences oscillations. Although their amplitude is two orders of magnitude smaller than the overall final length of the system, they remain non-negligible and, in applications such as space-based radar sounding, could potentially introduce inaccuracies in the measurements.

Furthermore, the overall cost associated with performing the deployment in the cross-track configuration is higher than in the other two cases - approximately twice as large. Nevertheless, considering that this configuration represents the final operational state to be achieved in this analysis, and that transitioning from a planar configuration to this perpendicular one would entail additional complexity and potential risks, this higher expenditure may represent an acceptable trade-off for performing the deployment directly in the cross-track configuration.

Chapter 7

Conclusions and future work

At the conclusion of this work, this brief closing chapter summarizes the main findings achieved throughout the study and outlines potential directions for further research that could build upon the results presented here.

7.1 Conclusion

At the core of the present study lies the MATLAB code, which served as the primary tool for the analysis. The code was developed with a structure that ensures scalability, enabling its application to a wide range of mission scenarios. This flexibility facilitated a systematic investigation of the Tethered Satellite System across different configurations and operational conditions, while also making it possible to modify or extend specific components of the code in a precise and isolated manner whenever required. As the model was progressively developed and validated through the analysis of the system's dynamics and deployment behavior under various conditions, this process also highlighted the inherent challenges associated with the high-fidelity model of the TSS, both in terms of computational cost and in the complexity associated with capturing the full range of factors influencing the system's dynamic response. Indeed, the stiffness and complexity of the governing equations, the high number of degrees of freedom, the sensitivity of the system to external perturbations, the inclusion of tether flexibility, and the intricate handling of deployment-related terms, are all factors that together contribute to the creation of a framework within which developing solutions that are both computationally efficient and practically implementable becomes highly challenging. These challenges motivated the adoption of a reduced-order model - the rod model - which enables simplified preliminary assessments while retaining sufficient fidelity to capture the essential system dynamics.

Building upon the works of Aliberti, Quadrelli, and Romano [27] on space based

radar sounding, this study sets the objective of exploring alternatives for achieving a fully deployed Tethered Satellite System cross-track configuration. Therefore, keeping in mind the challenges discussed above, the simplified rod model was employed to enable a less costly and more straightforward analysis of the three main deployment strategies, deriving an estimation of the corresponding control accelerations required to guarantee the system's stability. Subsequently, these control accelerations were given as input to the high-fidelity lumped masses model to assess their effectiveness in a more realistic representation of the TSS and to analyze the resulting system response under such control action.

The analysis revealed that in-plane maneuvers - namely the radial and the along-track deployment - are less demanding in terms of control effort and overall complexity. However, these approaches require a subsequent maneuver to achieve the desired cross-track configuration, which was not investigated in detail; initial trials indicate that such maneuvers exhibit significant instability. In contrast, direct cross-track deployment, although approximately twice as costly in terms of control effort, allows the system to reach the target configuration directly, exhibiting comparable levels of dynamical instability throughout the transition from the stowed to the fully deployed state. For this reason, the direct cross-track deployment emerges as the most promising and therefore the most deserving of further research efforts. This approach enables the execution of the deployment maneuver by concentrating the control effort into a single phase, maintaining the system directly in the out-of-plane configuration. In contrast, the other two strategies require an equivalent, if not greater, expenditure of effort to perform the subsequent transition from an in-plane arrangement to the cross-track configuration, after already demanding a non-negligible control action to ensure stability during the initial deployment phase.

Overall, based on these findings, it can be stated that, despite the higher initial control cost, direct cross-track deployment represents the most recommendable pathway for achieving the desired operational configuration. By concentrating the stabilization effort into a single, straightforward maneuver, this strategy stands out as the one worth pursuing. Leveraging the provided framework to design more accurate and efficient control laws would represent the final step toward successfully bringing the space-based radar sounding system into its operational configuration, ready to begin data acquisition.

7.2 Possible extension and future research

Over the months during which this research was carried out, several opportunities for further investigation have emerged, building upon the findings presented in this thesis. These include both directions aimed at improving the accuracy and realism of the obtained results, and others that may represent natural subsequent stages in the broader study of the Tethered Satellite System. This section, therefore, briefly outlines the most promising directions for future development.

• Enhancement of the discrete model fidelity:

Although the discretized mass tether model provides a high-fidelity approximation of the system, its realism could be further improved by incorporating torsional and bending stiffness. Such an extension would allow for a more accurate representation of the tether's flexibility and internal dynamics, capturing effects that are currently neglected but could be crucial for the precise pointing and overall performance of the system.

Inclusion of satellite attitude dynamics:

In order to gain a more complete understanding of the system's operational behavior, it is necessary to include the analysis of the attitude of the satellites composing the system. Introducing attitude degrees of freedom for the end satellites, and potentially for intermediate sensor elements along the tether, would substantially increase the complexity of the equations of motion. Nonetheless, to meet the performance requirements, this step would be fundamental for such applications that require precise pointing and alignment.

• More accurate control estimation within the rod model:

While the dumbbell model is primarily intended for preliminary assessments, it would be beneficial to explore more advanced control strategies available in the state of the art. Such an investigation could refine the initial estimation of control efforts, therefore improving the guidance for subsequent high-fidelity simulations.

Active control within the discrete model:

Implementing active control in the high-fidelity framework has proven to be challenging, as partially explored in this work. Although this was omitted from the chapters of this thesis, active controllers were indeed developed for the end satellites' positions using both PID and LQR approaches. During this process, the main obstacles encountered were the difficulty in tuning the controller parameters and the excessive computational time required by the code to complete the dynamic simulations. Nonetheless, further efforts in this direction could be highly valuable, focusing on identifying systematic approaches for control parameter selection and optimizing computation time to ensure both the feasibility and sustainability of on-board implementation. Additionally, considering the inherent nonlinearities of the TSS dynamics, it could be valuable to explore alternative control strategies better suited for handling such nonlinear behavior, such as sliding mode control.

• Detailed study of the deployment mechanism:

A factor that has only been vaguely mentioned during this research is the physical tether release mechanism itself. This component represents a key player within the deployment process and, therefore, it is essential to incorporate a detailed study of the chosen release mechanism into the system modeling. Consequently, a natural next step for future work would be to begin by analyzing existing tether release mechanisms, including known failure cases and lessons learned. Subsequently, in the context of the specific application under consideration - Tethered Satellite System for space based radar sounding - a suitable mechanism could be selected among existing options, or an innovative design may be proposed. Once identified, this choice should then be consistently integrated into the system model, allowing for a thorough evaluation of its effects on the deployment process, benefits, and potential pitfalls, such as impacts on maintaining tether tension during deployment.

• Experimental validation:

Technological advancements have made it possible to simulate orbital dynamics with a high degree of fidelity, and it would be a missed opportunity not to take advantage of such capabilities. For instance, facilities such as granite-based testbeds allow for a realistic reproduction of space system dynamics, enabling the inclusion of both environmental perturbations and control inputs. Ultimately, experimental testing would constitute the final step in validating the simulation results, providing a bridge between theoretical analysis and practical mission readiness.

Collision avoidance analysis:

Given the extended length of the tether, it would be interesting to investigate potential collision scenarios, assessing the associated risks and, if necessary, identifying the need for a dedicated Collision Avoidance System (CAS) specifically tailored for this Tethered Satellite System.

Bibliography

- [1] S. Zhang, C. Zhu, J. K. O. Sin, and P. K. T. Mok. "A Novel Ultrathin Elevated Channel Low-temperature Poly-Si TFT." In: 20 (Nov. 1999), pp. 569–571 (cit. on p. 3).
- [2] T. S. Kelso. "Analysis of the Iridium 33-Cosmos 2251 Collision." In: Proceedings of the Advanced Maui Optical and Space Surveillance Technologies Conference (AMOS). Maui Economic Development Board, 2009, pp. 361-370. URL: https://celestrak.org/publications/AMOS/2009/AMOS-2009.pdf (cit. on p. 3).
- [3] European Space Agency (ESA). About Space Debris. https://www.esa.int/ Space_Safety/Space_Debris/About_space_debris. Accessed: 2025-07-29 (cit. on p. 3).
- [4] J. C. Liou and N. L. Johnson. "A sensitivity study of the effectiveness of active debris removal in LEO." In: *Acta Astronautica* 64.2-3 (2008), pp. 236–243. DOI: 10.1016/j.actaastro.2008.06.021 (cit. on p. 4).
- [5] D. J. Kessler and B. G. Cour-Palais. "Collision Frequency of Artificial Satellites: The Creation of a Debris Belt." In: *Journal of Geophysical Research* 83.A6 (1978), pp. 2637–2646. DOI: 10.1029/JA083iA06p02637 (cit. on p. 4).
- [6] J. C. Liou. "Risks in Space from Orbiting Debris." In: Science 311.5759 (Jan. 2006), pp. 340–341. DOI: 10.1126/science.1121050 (cit. on p. 4).
- [7] D. L. Gallagher, L. Johnson, J. B. Moore, and F. Bagenal. *Electrodynamic Tether Propulsion and Power Generation at Jupiter*. Technical Publication NASA/TP-1998-208475. NASA, 1998. URL: https://ntrs.nasa.gov/api/citations/19980020847/downloads/19980020847.pdf (cit. on p. 5).
- [8] Spencer Wilson Ziegler. "The Rigid-Body Dynamics of Tethers in Space." PhD Thesis. PhD Thesis. PhD Thesis, [Nome Università, se noto], 2003 (cit. on p. 6).
- [9] Douglas Hoyt and Richard Uphoff. "Cislunar Tether Transport System." In: Journal of Spacecraft and Rockets 37.2 (2000), pp. 177–186 (cit. on p. 6).

- [10] Robert L. Forward and Peter Nordley. "Mars-Earth Rapid Interplanetary Tether Transport (MERITT) System. I Initial Feasibility Analysis." In: 35th Joint Propulsion Conference, AIAA Paper 1999-2151. American Institute of Aeronautics and Astronautics (AIAA), 1999. URL: https://arc.aiaa.org/doi/abs/10.2514/6.1999-2151 (cit. on p. 6).
- [11] Vladimir S. Aslanov and Alexander S. Ledkov. "Survey of Tether System Technology for Space Debris Removal Missions." In: *Journal of Space Engineering and Technology* (2020). Samara National Research University, Samara Russia (cit. on p. 7).
- [12] Aliberti Stefano. "Modeling, Dynamics and Control of Space Tethered System as Distributed Radar Array." Politecnico di Torino (cit. on p. 7).
- [13] NASA. HelioSwarm: A Multipoint, Multiscale Mission to Characterize Turbulence. NASA Science Mission Website. 2023. URL: https://ntrs.nasa.gov/api/citations/20230007800/downloads/SSC23%20HelioSwarm%20Overview.pdf (cit. on p. 8).
- [14] M. L. Cosmo and E. C. Lorenzini. *Tethers in Space Handbook*. Tech. rep. NASA/CR-97-206807. NASA Marshall Space Flight Center, 1997. URL: htt ps://ntrs.nasa.gov/archive/nasa/casi.ntrs.nasa.gov/19920010006.pdf (cit. on p. 11).
- [15] Paul Williams. "Deployment/retrieval optimization for flexible tethered satellite systems." In: *Nonlinear Dynamics* 52 (2008), pp. 159–179. DOI: 10.1007/s11071-007-9269-3. URL: https://link.springer.com/article/10.1007/s11071-007-9269-3 (cit. on p. 11).
- [16] B. S. Yu, H. Wen, and D. P. Jin. "Review of deployment technology for tethered satellite systems." In: Acta Mechanica Sinica 34.4 (2018), pp. 754-768. DOI: 10.1007/s10409-018-0752-5. URL: https://doi.org/10.1007/s10409-018-0752-5 (cit. on pp. 11, 73).
- [17] R. D. Estes. Theoretical investigation of EM wave generation and radiation in the ULF, ELF, and VLF bands by the electrodynamic orbiting tether. Tech. rep. NASA/CR-1988-11145. NASA Marshall Space Flight Center, 1988. URL: https://ntrs.nasa.gov/citations/19880011145 (cit. on p. 13).
- [18] M. L. Cosmo and E. C. Lorenzini. Tethers in Space Handbook, COMET / Asteroid Sample Return, PA.11.00. Tech. rep. NASA/TP-1986-PA.11.00. NASA Marshall Space Flight Center, Aug. 1986. URL: https://ntrs.nasa.gov/api/citations/19860004517/downloads/19860004517.pdf (cit. on p. 13).

- [19] Matteo Duzzi, Lorenzo Olivieri, and Alessandro Francesconi. "Tether-Aided Spacecraft Docking Procedure." In: *Acta Astronautica* 126 (2016), pp. 1–11. URL: https://doi.org/10.1016/j.actaastro.2016.03.013 (cit. on p. 13).
- [20] Martin Birkelund Larsen and Mogens Blanke. "Passivity-Based Control of a Rigid Electrodynamic Tether." In: Journal of Guidance, Control, and Dynamics 34.1 (2011). Technical University of Denmark, pp. 118–127. DOI: 10.2514/1.50446. URL: https://doi.org/10.2514/1.50446 (cit. on p. 13).
- [21] Konstantin E. Tsiolkovsky. Moscow, 1959 (cit. on p. 13).
- [22] Yuri Artsutanov. To the Cosmos by Electric Train. Traduzione inglese di Joan Barth Urban e Roger G. Gilbertson, 2004. 1960 (cit. on p. 13).
- [23] Jerome Pearson. "The Orbital Tower: A Spacecraft Launcher Using the Earth's Rotational Energy." In: *Acta Astronautica* 2.9–10 (1975), pp. 785–799. DOI: 10.1016/0094-5765(75)90021-1. URL: https://doi.org/10.1016/0094-5765(75)90021-1 (cit. on p. 13).
- [24] Bradley C. Edwards. "Design and Development of a Space Elevator." In: *Acta Astronautica* 47.10 (2000), pp. 735–744 (cit. on p. 13).
- [25] John M. Knapman. Exploiting a Space Elevator at Geosynchronous Altitude. International Space Elevator Consortium. 2024 (cit. on p. 14).
- [26] George Z.H. Zhu and Li Gangqiang. "A Novel Concept of a Parallel Partial Space Elevator with Multiple Carts." In: *Proceedings of the AIAA SciTech Forum.* 2020. DOI: 10.2514/6.2020-4250. URL: https://arc.aiaa.org/doi/10.2514/6.2020-4250 (cit. on p. 14).
- [27] Stefano Aliberti, Marco B. Quadrelli, and Marcello Romano. "A distributed space radar sounder using a cross-track flying tethered satellite system." In: Acta Astronautica 221 (2024), pp. 266–282. DOI: 10.1016/j.actaastro. 2024.05.018. URL: https://doi.org/10.1016/j.actaastro.2024.05.018 (cit. on pp. 14, 16, 72, 103).
- [28] Leonardo Carrer, Christopher Gerekos, Francesca Bovolo, and Lorenzo Bruzzone. "Distributed Radar Sounder: A Novel Concept for Subsurface Investigations Using Sensors in Formation Flight." In: IEEE Transactions on Geoscience and Remote Sensing 57.12 (2019), pp. 9791–9809. DOI: 10.1109/TGRS. 2019.2929422. URL: https://ieeexplore.ieee.org/document/8765321 (cit. on pp. 14, 15).

- [29] NASA / Apollo Lunar Sounder Experiment Team. Apollo Lunar Sounder Experiment (ALSE). NASA Technical Reports / Lunar Orbiter Program. 1972–1977. URL: https://ntrs.nasa.gov/citations/19720010325 (cit. on p. 14).
- [30] European Space Agency / Mars Express MARSIS Team. Mars Advanced Radar for Subsurface and Ionosphere Sounding (MARSIS). ESA Mission Instrument Description. 2005. URL: https://www.esa.int/Science_Exploration/Space_Science/Mars_Express/MARSIS (cit. on p. 14).
- [31] Japan Aerospace Exploration Agency (JAXA). SELENE (Kaguya) Lunar Orbiter Mission. JAXA Mission Overview. 2007–2009. URL: https://global.jaxa.jp/projects/sat/selene/ (cit. on p. 14).
- [32] NASA. Tethered Satellite System Contingency Investigation Board Report. Tech. rep. NASA, 1992. URL: https://ntrs.nasa.gov/api/citations/19930016042/downloads/19930016042.pdf (cit. on pp. 18, 82).
- [33] NASA. Tethered Satellite System (TSS-1R) Post-Flight Report. Tech. rep. NASA, 1996. URL: https://ntrs.nasa.gov/api/citations/19970011947/downloads/19970011947.pdf (cit. on p. 18).
- [34] ESA / DLR. The Second Young Engineers' Satellite (YES2). 2007. URL: https://www.academia.edu/1220395/The_Second_Young_Engineers_Satellite (cit. on p. 18).
- [35] JAXA. KITE (Kounotori Integrated Tether Experiment). 2017 (cit. on p. 18).
- [36] C. Rupp. "Tether dynamics and control: A survey." In: *Acta Astronautica* () (cit. on p. 19).
- [37] V. S. Aslanov. "Deployment dynamics of the tethered system YES2 based on the swing principle." In: *Proceedings of the 66th International Astronautical Congress (IAC-15)*. 2015, pp. C1, 7, 9. URL: https://aslanov.ssau.ru/papers/IAC-15%2CC1%2C7%2C9%2Cx28257.pdf (cit. on p. 19).
- [38] S. Pradeep. "A New Tension Control Law for Deployment of Tethered Satellites." In: Mechanics Research Communications 24.3 (1997), pp. 247–254. DOI: 10.1016/S0093-6413(97)00021-9 (cit. on p. 19).
- [39] Z. H. Zhu and L. Murugathasan. "Optimal linear control of tethered satellite deployment." In: *Acta Astronautica* 111 (2015), pp. 245–255 (cit. on p. 19).
- [40] H. Kojima and T. Taruoka. "Deployment Control of a Tethered Satellite System for Rendezvous with a Target." In: *The Japan Society for Aeronautical and Space Sciences* 59 (2016), pp. 313–322 (cit. on p. 19).
- [41] J. Kang, S. Xu, and Y. Xie. "Fractional-order sliding mode control for tether deployment in space." In: *Nonlinear Dynamics* 90.2 (2017), pp. 1169–1183 (cit. on p. 19).

- [42] David A. Vallado. Fundamentals of Astrodynamics and Applications. 4th. Microcosm Press, 2013 (cit. on p. 32).
- [43] W. A. Heiskanen and H. Moritz. *Physical Geodesy*. W.H. Freeman and Company, 1967 (cit. on pp. 32, 34, 59).
- [44] Mark A. Wieczorek and Matthias Meschede. "Ultra-high-degree surface spherical harmonic analysis using the Gauss-Legendre and the Driscoll/Healy quadrature theorem and application to planetary topography models of Earth, Mars and Moon." In: Journal of Geophysical Research: Planets (2005) (cit. on p. 32).
- [45] Marco B. Quadrelli, Masaki Ono, and Ankur Jain. "Modeling of Active Tether System Concepts for Planetary Exploration." In: *Acta Astronautica* 138 (2017), pp. 512–529. DOI: 10.1016/j.actaastro.2017.04.017 (cit. on pp. 36, 73).
- [46] Mattia Pastori, Francesco Braghin, and Marco Bruno Quadrelli. "Modeling, Dynamics and Control of a Variable Topology Tethered Space System." In: Proceedings of the 2022 IEEE Aerospace Conference (AERO). IEEE, 2022. DOI: 10.1109/AER053065.2022.9843490 (cit. on p. 36).
- [47] Marco B. Quadrelli and Enrico C. Lorenzini. "Dynamics and Stability of a Tethered Centrifuge in Low-Earth Orbit." In: () (cit. on p. 60).
- [48] Aaron Teik Hong Aw, Renuganth Varatharajoo, and Yew-Chung Chak. "Review of deployment technology for tethered satellite systems." In: Review of deployment controllers for space tethered system (2020) (cit. on p. 82).